ISSN 1000-9620

海洋通报

Marine Science Bulletin

NATIONAL MARINE DATD AND
INFORMATION SERVICE OF CHINA

2013
Volume 15
Number 2

NOAA
U.S. DEPARTMENT OF COMMERCE
NATIONAL OCEANIC AND ATMOSPHERIC ADMINISTRATION

NOAA CENTRAL LIBRARY
WITHDRAWN
AUG 22 2017
National Oceanic &
Atmospheric Administration
US Dept of Commerce

MARINE SCIENCE BULLETIN

Vol. 15 No. 2 Oct. 2013

CONTENTS

Application of the two different salinity parameterization schemes in the sea ice model ..... WANG Qing-yuan et al. (03)

Seasonal evolution of the Northern Yellow Sea cold water mass ..... LI Xi-bin et al. (15)

Effect of sea surface wind on the seasonal variation of sea level in the east of China seas ..... MU Lin et al. (26)

Study on the calculation of the position and scope of tropical cyclone ..... LIU Yong-lu et al. (37)

Ocean surface current retrieval based on the satellite remote sensing data ..... AN Yu-zhu et al. (46)

Research of the wave measurement using GPS absolute velocity estimation technology ..... SHAN Rui et al. (59)

A review of numerical modeling research on the marine oil spill ..... CAI Yang et al. (71)

Distribution and ecological evaluation of heavy metals in multi-medium of the Dongzhai Harbor ..... TIAN Hai-tao et al. (87)

LIBRARY
Pacific Islands Fisheries Science Center
NOAA Fisheries
Honolulu, Hawai'i

海 洋 通 报（英文版）

HAIYANG TONGBAO

2013 年 10 月 第 15 卷 第 2 期

目 次

两种盐度参数化方案在海冰模式中的应用比较 …… 王庆元 等 (14)

北黄海冷水团季节变化特征分析 …… 李希彬 等 (25)

风对中国东部海域海平面季节变化的影响 …… 牟 林 等 (36)

基于卫星云图的轮廓法自动识别热带气旋研究 …… 刘永禄 等 (45)

基于卫星遥感数据的全球表层流场反演重构 …… 安玉柱 等 (58)

基于 GPS 单点测速的海浪测量方法初探 …… 单 瑞 等 (70)

海上溢油数值模型研究进展 …… 蔡 扬 等 (86)

海南东寨港重金属在多种环境介质中污染状况及评价 …… 田海涛 等 (96)

NOAA CENTRAL LIBRARY

AUG 22 2017

National Oceanic &
Atmospheric Administration
US Dept of Commerce

Vol. 15 No. 2 Marine Science Bulletin Oct. 2013

Application of the two different salinity parameterization schemes in the sea ice model

WANG Qing-yuan[1], LI Yan[2], LI Qing-quan[3], WANG Lan-ning[4], MU Lin[2], YI Xiao-yuan[1]

1. *Tianjin Meteorological Observatory, Tianjin* 300074, *China;*
2. *National Marine Data and Information Service, Tianjin* 300171, *China;*
3. *National Meteorological Centre, Beijing* 100081, *China;*
4. *Beijing Normal University College of Global Change and Earth System Science, Beijing* 100875, *China*

Abstract: In this study, we mainly introduce two salinity parameterization schemes used in Sea Ice Simulator (SIS), that is, isosaline scheme and salinity profile scheme. Comparing the equation of isosaline scheme with that of salinity profile scheme, we found that there was one different term between the two schemes named the salinity different term. The thermodynamic effect of the salinity difference term on sea ice thickness and sea ice concentration showed that: in the freezing processes from November to next May, the sea ice temperature could rise on the influence of the salinity difference term and restrain sea ice freezing; at the first melting phase from June to August, the upper ice melting rate was faster than the lower ice melting rate. Then sea ice temperature could rise and accelerate the sea ice melting; at the second melting phase from September to October, the upper ice melting rate was slower than the lower ice melting rate, then sea ice temperature could decrease and restrain sea ice melting. However, the effect of the salinity difference term on the sea ice thickness and sea ice concentration was weak. To analyze the impacts of the salinity different term on Arctic sea ice thickness and sea ice concentration, we also designed several experiments by introducing the two salinity parameterizations to the ice-ocean coupled model, Modular Ocean Model (MOM4), respectively. The simulated results confirmed the previous results of formula derivation.

Keywords: Arctic, sea ice model, salinity parameterization scheme

1 Introduction

Since 1960s, the scientists continuously developed the sea ice models, in order to improve the ability of simulation. Maykut et al.[1] constructed a thermal sea ice model which

Received on Jul. 23, 2013

Corresponding author: wqyjx@sohu.com

is a one-dimensional model(hereafter referred to as MU71), governed ice growth rate using the surface heat balance, and governed ice transfer using diffusion equation in 1971. This model also included the effect of snow cover, ice salinity, ice bubble, bubble, shortwave radiation heat transmission, vertical change of ice density, conductivity as well as the heat capacity. Semtner [2] simplified the MU71 in sea ice model in 1976. This simplified model with only one snow layer, two ice layers, constant heat conduction and simple salt content parameters could simulate the seasonal variations of sea ice thicknesses and areas. Bitz et al.[3] suggested that sea ice heat capacity could not only include the energy which was needed to increase sea ice temperature, but also include the energy which was needed to raise salt water bubble temperature and melt sea ice around the salt water bubble. Thus a sea ice model with a clear physical process should be able to accurately describe the heat capacity and fusion heat of sea ice. After that, Bitz et al. [3] developed a multi-layer sea ice thermal model with a conservational energy and solved the problem above well. In 2000, Winton designed a sea ice model named SIS which was based on the model developed by Semtner. This model kept three layers of vertical structure and also considered the conservation of the heat capacity as well as fusion heat of sea ice. A completely iterative implicit time step scheme was made to calculate the sea ice temperature in Winton model. Therefore, Winton model could adopt much longer time step than the time step used in Semtner model. Besides, the Winton model could well couple with atmospheric model named GFDL (Geophysical Fluid Dynamics Laboratory).

Usually, there are two salinity parameterization schemes in sea ice models, that is, isosaline scheme, in which the salinity of the sea ice was the same in each layer, and salinity profile scheme. Both of the simplified sea ice model developed by Semtner and the SIS model developed by Winton adopt isosaline parameterization scheme rather than salinity profile scheme in the vertical direction. However, the two models could simulate seasonal variations of sea ice thicknesses and areas which differ slightly from the observational data. So if we introduce the salinity profile scheme in the SIS, can the model simulate much more similar seasonal changes in sea ice thickness and area? This article discussed the differences between the simulations using salinity profile scheme in SIS and the simulations using isosaline scheme in SIS model. In addition, the physical reasons of the differences will be discussed in this research.

This paper includes the following four sections: the first section includes the introduction of the salinity profile scheme. The SIS model and the calculation processes of the derivation equations to replace original isosaline scheme with salinity profile scheme are described in section 2. Besides, in this section, we compare the differences between the effect of the salinity profile scheme and the influence of isosaline scheme on sea ice

physical process. In section 3, we simulate the seasonal variations of sea ice thicknesses and areas using the two salinity schemes by MOM4 respectively. Then, comparative analysis is made to illustrate the sea ice physical processes that influence ice thicknesses and areas. Finally, we discuss these results and give conclusions.

2 The two salinity parameterization schemes on vertical direction in sea ice model

For isosaline scheme, salinity in the vertical direction of sea ice is constant and for salinity profile scheme, salinity in the vertical direction of sea ice satisfies salinity profile line. In this paper, the salinity profile scheme, which was also used in the MU7I model and energy conservation model designed by Bitz et al. [3] in 1999, is an empirical formula deduced from observational data. In the formula, salinity profile is time independent. Suppose that no salinity is at snow layer and the salinity named S_i at halfway point of individual ice layer represents the salinity of the layer whose value is determined by relative position. The empirical formula given by Schwarzacher [5] shows as follows:

$$S_i = 1.6[1 - \cos(\pi z^{(a/(b+z))})] \tag{1}$$

where z=(k-0.5)/N_i, and k represents the layer of sea ice, and a, b are the empirical constants, a=0.407, b=0.573. Ni represents the total layers of sea ice. From equating (1), we can note that the range of salinity S_i is 0 - 3.2 ppt. In this article, we use three-layer SIS sea ice model (Fig. 1). Fig. 1 illustrates the salinity in this model: the snow salinity is zero, the upper layer S_1=1.62 ppt; the lower layer sea ice salinity S_2=3.14 ppt; the bottom sea ice salinity S_3=3.20 ppt.

3 Three-layer SIS thermal model and its formula derivation

Fig. 1 depicts the vertical structure schematic diagram of the 3-layer SIS model which includes a layer of choice partisan, upper and lower sea ice layers with the same thickness. There are several assumptions in the model, as follows: no heat capacity effect in the snow layer; sensible heat flux and latent heat flux existing in the upper layer, but only considering sensible heat flux in the lower layer; sun radiation just absorbed by sea ice without snow or through the sea ice into the ocean; the lower layer sea ice don't absorb solar radiation; thermal process only changing in the vertical direction and not considering the variation of

the lateral boundary. The calculation processes of vertical thermal of the three-layer SIS sea ice model are made by the following three main steps: firstly, calculate three temperature variables T_S, T_1, T_2. Among them, T_S is the snow layer surface temperature which is obtained by diagnosis and the value should be less than or equal to the melting temperature. T_1 and T_2 represent the halfway point temperature of upper and lower layer, respectively. The sea ice temperature T_b on the bottom is a constant, that is, -1.8 °C. Secondly, using the value calculated from the first step, we solve out the surface energy flux of the sea ice and the energy flux on the bottom of the sea ice. Then values of energy flux are used to obtain the quality variations of sea ice and snow and then to adjust the thickness of ice and snow layer. Finally, heat enthalpies of upper and lower layer ice are changed due to the adjustment of the sea ice thickness. As a result, T_1, T_2 and T_S are adjusted and get a group of new values of T_1, T_2 and TS which are used as integral initial values for the next time step. The three steps above are a cycle of the sea ice thermal process of SIS model. Next, we show the calculation processes of SIS model which adopt the salinity profile scheme. The calculation processes refer to the calculation process of isosaline scheme given by Winton et al. [4] in 2000.

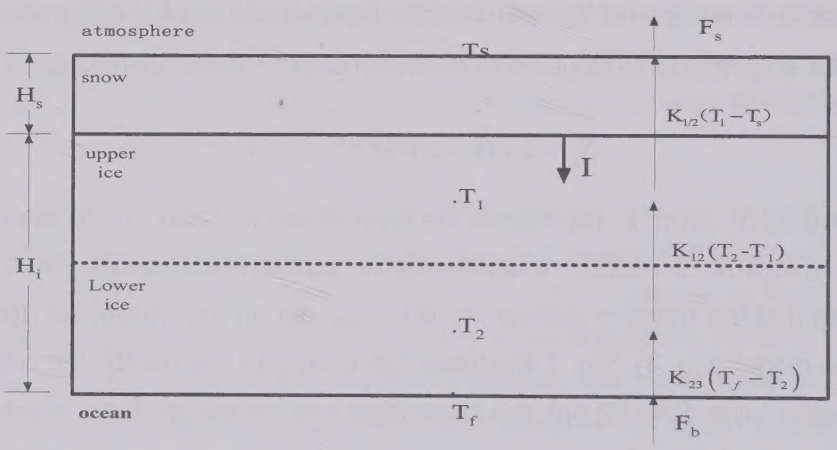

Fig. 1 Schematic diagram of the 3-layer mode

(H_s is the snow of thickness. H_i is the ice of thickness. T_s is the surface temperature. T_f is a bottom temperature. F_s is heat flux at the surface of the ice entering to the atmosphere. F_b is the heat flux input from the ocean. i is short radiation entering to ocean or absorbed by the upper lay ice.)

3.1 The calculation of sea ice physical quantities before the sea ice heat enthalpy adjustment for the upper and lower layers

Using the three-layer structures of SIS and the four assumptions above, the sea ice heat enthalpy conservation equations for per unit mass of upper and lower layers are constructed as following:

$$E_1(T_1, S_1) = C_0(T_1 + \mu S_1) - L(1 + \mu S_1 / T_1) \tag{2}$$

$$E_2(T_2, S_2) = C_0(T_2 + \mu S_2) - L \tag{3}$$

where E_1 was the heat enthalpy of upper layer, and E_2 was heat enthalpy of lower layer. C_0 is the heat capacity constant, and μ is the experience constant, referring to coefficient between sea ice melt temperature and salinity. L is the icy latent heat release constant. Equation (2) and (3) derivate to the time and then both sides of the equations are multiplied by the unit area of sea ice thickness mass m to get equations (4) and (5):

$$m \frac{dE_1}{dt} = m\left(C_0 + \frac{L\mu S_1}{T_1^2}\right)\frac{dT_1}{dt} \tag{4}$$

$$m \frac{dE_2}{dt} = mC_0 \frac{dT_2}{dt} \tag{5}$$

Combined with Fig. 1 and equation (4) and (5), we get heat unit area flux balance equation for the upper and lower layers.

$$\frac{\rho_i h_i}{2}\left(C_0 + \frac{L\mu S_1}{T_1^2}\right)\frac{dT_1}{dt} = K_{1/2}(T_s - T_1) + K_{12}(T_2 - T_1) + I \tag{6}$$

$$\frac{\rho_i h_i}{2} C_0 \frac{dT_2}{dt} = K_{12}(T_1 - T_2) + K_{23}(T_f - T_2) \tag{7}$$

Equations (6) and (7) are discredited, to get equations (8) and (9):

$$\frac{\rho_i h_i}{2\Delta t}\left(C_0 + \frac{L\mu S_1}{T_1\overline{T_1}}\right)(T_1 - \overline{T_1}) = K_{1/2}(T_s - T_1) + K_{12}(T_2 - T_1) + I \tag{8}$$

$$\frac{\rho_i h_i}{2\Delta t} C_0 (T_2 - \overline{T_2}) = K_{12}(T_1 - T_2) + K_{23}(T_f - T_2) \tag{9}$$

where $\overline{T_1}$, $\overline{T_2}$ respect the time step temperatures of the upper and lower layers, and T_2 is given by equation (9):

$$T_2 = \frac{2\Delta t K_{12}(T_1 + 2T_f) + \rho_i h_i C_0 \overline{T_2}}{6\Delta t K_{12} + \rho_i h_i C_0} \tag{10}$$

The diagnosis equation of T_s is derived from Eq T_1, given by:

$$T_s = \frac{K_{1/2} T_1 - A}{K_{1/2} + B} \tag{11}$$

where A and B are functions of last time step surface temperature, which are known items.

Integrate equations (8), (10) and (11) to obtain a quadric equation of T_1. Solve this equation to get T_1 and then equations (10) and (11) to get T_2 and T_s. Above mentioned items are individual sea ice temperatures calculated by salinity profile before sea ice thickness adjustment. The net heat M_s of sea ice surface could be obtained by T_1, T_2 and

T_3, and the equation is as follow,

$$M_s = K_{1/2}(T_1 - T_s) - F_s \tag{12}$$

The net heat Mb on the bottom of sea ice is given by:

$$M_b = F_b - K_{23}(T_f - T_2) \tag{13}$$

In equation (12) F_s is the heat flux conducted from snow or ice layer to air. F_b in equation (13) is the oceanic heat flux into the bottom of sea ice. Equations (12) and (13) are the criterion equation for sea ice melts and freezing respectively, that is, M_s>0 means sea ice beginning to melt from surface; M_b>0 mean sea ice beginning to freeze from the bottom. These are the three external physical processes of sea ice and snow. In addition to these three processes, sea ice model also include two internal adjustment processes, that is, snow layer, which is lower than water line, would partisan into ice layer. Thus, sea ice thicknesses of upper and lower layers readjust and satisfy the structure shown in Fig. 1.

If S_1 is the salinity of the isosaline scheme, calculations of the sea ice physical quantities in the schemes before enthalpy adjustment agree closely with that in the salinity profile scheme. However, after enthalpy adjustment, the calculation equations of individual ice layer in the two schemes are different. To study the effect of the differences, we set the salinity of each sea ice layer in the isosaline scheme as the value of S_1 which is the salinity of the upper layer ice of the salinity profile scheme.

3.2 The calculations of sea ice physical quantities after the enthalpy of upper and lower sea ice adjustment

The heat enthalpy of upper and lower ice layer changes after the sea ice thicknesses adjustment and needs to adjust the sea ice temperature of the two layers. Suppose that in the SIS model, the temperature of the supplying sea ice layer is the constant and the temperature of the receiving sea ice layer adjusts. It suggests that when lower sea ice enters into the upper ice, the upper ice temperature adjusts and the adjusted enthalpy conservation equation is as follow:

$$E_1(T_{1new}, S_1) = f_1 E_1(T_1, S_1) + (1 - f_1) E_2(T_2, S_2) \tag{14}$$

The left term of equation (14) means the re-adjustment heat enthalpy of upper layer ice. The first term in the right side is the original heat enthalpy of upper layer sea ice. The second term in the right side is the heat enthalpy entering into the upper layer sea ice, where $f_1 = h_1 / (h_1 + \triangle h)$, and h_1 is the sea ice thickness of upper layer before the adjustment, and $h_1 + \triangle h$ is the sea ice thickness of upper layer after the adjustment. After taking equations (2) and (3) into (14), we get equation (15):

$$T_{1new} = \frac{\overline{T} - \left(\overline{T}^2 + 4\mu S_1 L / C\right)^{1/2}}{2} \tag{15}$$

where:

$$\overline{T} = f_1(T_1 - \frac{L}{C}\frac{\mu S_1}{T_1}) + (1 - f_1)T_2 + \mu(S_2 - S_1)(1 - f_1) \tag{16}$$

If the upper sea ice enters into lower layer sea ice, the lower layer sea ice temperature could be obtained using a similar method:

$$T_{2new} = \frac{(\Delta h T_1 + h_2 T_2 - \Delta h L \mu S_1 / (T_1 C))}{(\Delta h + h_2)} + \frac{\Delta h \mu (S_1 - S_2)}{(\Delta h + h_2)} \tag{17}$$

If the sea ice on the bottom freezes, the lower layer sea ice temperature would come to change. Supposing the ice thickness is $\triangle h_2$, the adjusted temperature of the lower layer sea ice could be got using a similar method:

$$T_{2new} = \frac{(\Delta h_2 T_f + h_2 T_2)}{(\Delta h_2 + h_2)} + \frac{\Delta h_2 \mu (S_3 - S_2)}{(\Delta h_2 + h_2)} \tag{18}$$

The adjustment sea ice temperature calculated by the above formulae would be served as the initial temperature of the next time.

While adopting isosaline scheme, the last terms of equations (16), (17), (18) are zero due to the same value of sea ice salinity at each ice layer. Comparing the model equations in the isosaline scheme with that in the salinity profile scheme, there is one different term between the three equations of the two schemes named salinity different term. From equations (16), (17), (18), the thermodynamic effects of the salinity difference term on sea ice thickness and area show that: when the lower layer sea ice enters into upper layer sea ice, the ice temperature of the upper layer will rise. When the upper layer sea ice enters into lower layer sea ice, the ice temperature of the lower layer will decrease. Scale analysis shows that the salinity different term is smaller than the largest term of the equation about an order of 1 - 2. Thus, the salinity different term could be omitted if adopting an approximation. It suggests that in the SIS model, the simulations of sea ice thicknesses and areas using the two salinity schemes differ slightly.

4 Simulations of the two salinity parameterization schemes used in sea ice model

4.1 Model description and experiment design

Due to the flux exchange between sea ice and ocean, we adopt the low resolution

global ice-ocean coupled model named Modular Ocean Model V4.0 (MOM4) and simulate the sea ice with GFDL. SIS model is the part of the MOM4 model. Two sensitivity experiments are performed to investigate the impacts of different salinity schemes. Sensitivity experiment 1: this experiment uses original isosaline scheme (the salinity value is 1.62 ppt) in model, referred as Exp1; Sensitivity experiment 2: this experiment uses salinity profile scheme in SIS model to replace the original isosaline scheme, referred as Exp2. In each experiment, the model is integrated for 50 years. The average of the last ten years is regarded as the model simulation. The effects of the salinity difference term on sea ice thicknesses and areas et al. are obtained by subtracting results of the experiment 1 from Exp 2.

4.2 Experimental results

The seasonal variation of sea ice thicknesses of Exp1 and Exp2 and the differences between Exp1 and Exp2 are shown in Fig. 2. The maximum sea ice thickness is in May and the minimum sea ice thickness is in October. The sea ice melting phase is from June to October and the sea ice freezing phase is from November to May of the next year. The gray line in Fig. 2 denotes the differences of sea ice thickness between Exp1 and Exp2, that is, the variations of sea ice thickness caused by salinity different term. It suggests that under the effect of salinity different term, the sea ice thickness decreases. However, the maximum value is only 0.55 cm in August. That is to say, the simulations of sea ice thickness and area using two salinity schemes are similarly. And, the simulations of sea ice concentration are also similar.

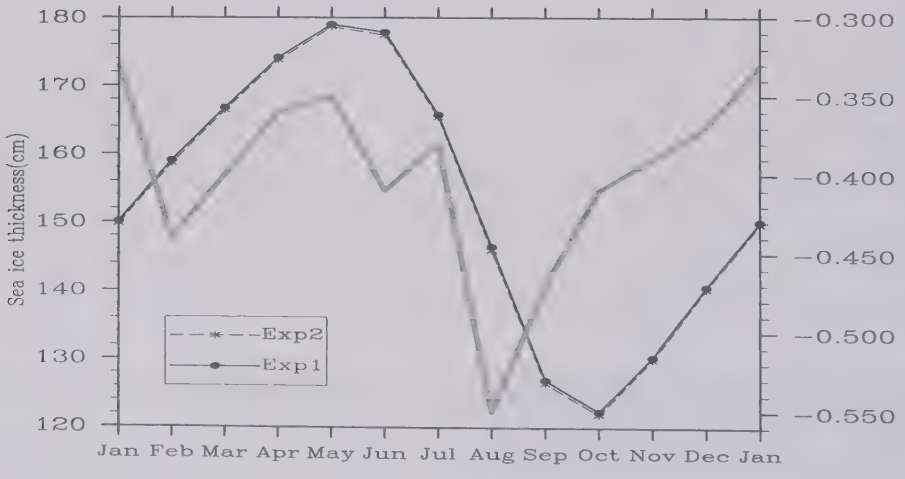

Fig. 2 Sea ice thickness of Exp1 (black solid line) and Exp2 (black dashed line) and the difference of the sea ice thickness between Exp1 and Exp2 (gray line)

Fig. 3 shows the changes of sea ice temperature caused by salinity different term. Fig. 3 implies that sea ice temperature differences are positive in the Arctic sea ice growth period (November to May of the next year) and means that the lower layer sea ice enters into the upper layer sea ice. That is to say, the growth of sea ice thickness of Arctic is caused by sea ice freezing at the bottom of ice. At the first melting phase from June to August, the upper ice melting rate is faster than the lower ice melting rate. The lower layer sea ice enters into the upper layer sea ice. At the second melting phase from September to October, the upper ice melting rate is slower than the lower ice melting rate. In this way, the lower layer sea ice enters into upper layer sea ice.

The results made by Maykut [1] showed that the simulated annual average melting ice at the sea surface of Arctic was 40.1 cm and the simulated melting period was from June 29 to August 19. The simulated annual average sea ice melting at the bottom was 5.1 cm and the simulated melting period was from July 17 to November 11. The simulated sea ice melting period in our article is from June to August. The melting period of sea ice at the bottom is from September to October. The upper layer sea ice enters into the lower layer sea ice and causes the negative sea ice temperature difference from September to October. The simulations of numerical experiments confirmed the conclusions of the above formulae.

The simulated sea ice thicknesses of Arctic in August using isosaline scheme and salinity profile scheme in the SIS model are shown in Fig. 4, respectively. Results indicate that simulations of sea ice thicknesses by two salinity schemes are similar.

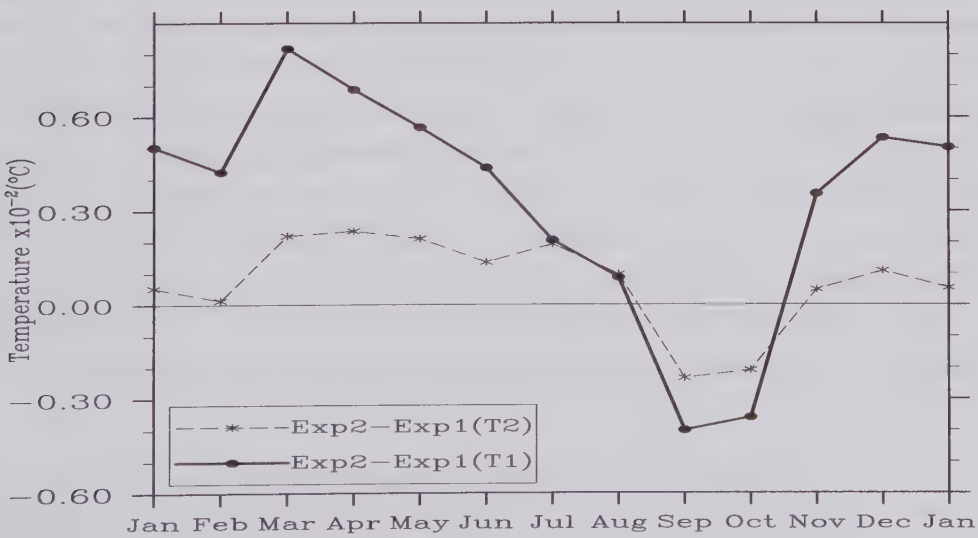

Fig. 3 Upper ice and lower ice temperature differences between Exp2 and Exp1

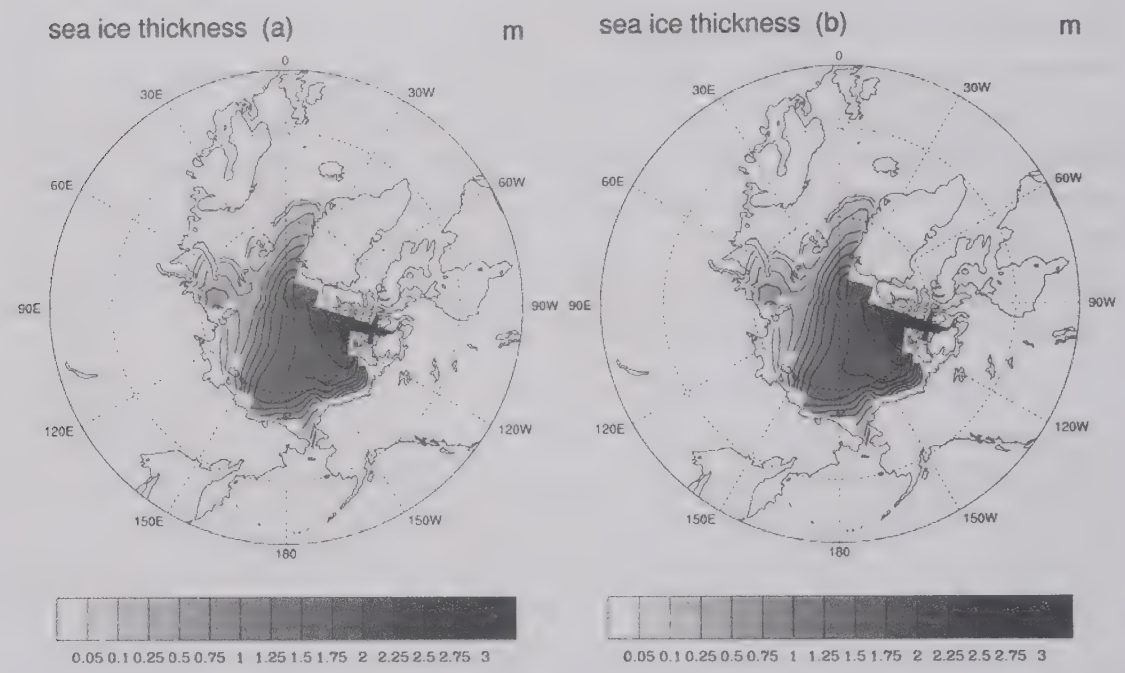

Fig. 4 Sea ice thicknesses and concentration distributions in August of the isosaline scheme (left panel) and salinity profile scheme (right panel)(a and b are the sea ice thickness, unit: cm)

5 Summary and discussion

(1) There are two salinity parameterization schemes used in SIS sea ice model, that is, isosaline scheme and salinity profile scheme. Comparing the equations of isosaline scheme with that of salinity profile scheme, there is one different term, named salinity different term between the two schemes. Scale analysis shows that the salinity different term is smaller than the largest term of the equation about an order of 1 - 2. Thus, the salinity different term could be omitted if adopting an approximation. Salinity parameterization scheme affects the sea ice temperature through the sea ice salinity and then impacts the sea ice thicknesses. Therefore, the simulations of the SIS model usidng any salinity parameterization scheme to simulate the Arctic sea ice thicknesses are basically the same. The subsequent simulations of numerical experiments confirm the conclusions of the above formulae.

(2) Thermal effects of the salinity different term are as follows: in the Arctic sea ice growth period (November to May of the next year), sea ice temperature could rise under the influence of the salinity difference term and restrain sea ice freezing. At the first melting phase from June to August, the upper ice melting rate is faster than the lower ice melting

rate. Then sea ice temperature could rise and accelerate the sea ice melting. At the second melting phase from September to October, the upper ice melting rate is slower than the lower ice melting rate, then sea ice temperature could decrease and restrain sea ice melting. However, the effect of the salinity difference term on the sea ice thickness is slight.

In this paper, we mainly discuss the differences between the two salinity parameterization schemes used in SIS model. Also, we investigate the thermal effect of the salinity difference term. In the SIS model, the simulations of sea ice thicknesses and sea ice concentration using two salinity schemes are similar. Thus, to improve the speed of calculation of SIS model and reduce the errors from calculation, we could adopt the isosaline scheme rather than salinity profile scheme. However, adjustment of the salinity scheme in SIS model can't reduce the deviation between simulations of sea ice thickness and concentration and observations. Thus, we need to improve the model from the perspective of others.

Acknowledgements

This paper is supported by the National Natural Science Foundation of China (No. 41075030, 41106004, 41106159 and 41206013) and the Ocean Public Welfare Science Research Project, State Oceanic Administration, People's Republic of China (No. 201005019).

References

[1] Maykut G A, Untersteiner N. Some results from a time-dependent thermodynamic model of sea ice [J]. J. Geophys. Res., 1971, 76, 1 550 - 1 575.

[2] Semtner A J. A model for the thermodynamic growth of sea ice in numerical investigations of climate [J]. J. Phys. Oceanogr., 1976, 6, 379 - 389.

[3] Bitz C M, Lipscomb W H. A new energy-conserving sea ice model for climate study [J]. J. Geophys. Res., 1999,104, 15 669 - 15 677.

[4] Winton M. A reformulated three-layer sea ice model [J]. J. Atmos. Ocean Tech., 2000, 17, 525 - 531.

[5] Schwarzacher W. Pack ice studies in the Arctic Ocean [J]. J. Geophys. Res., 1959, 64, 2 357 - 2 367.

两种盐度参数化方案在海冰模式中的应用比较

王庆元[1]，李 琰[2]，李清泉[3]，王兰宁[4]，牟 林[2]，易笑园[1]

（1. 天津市气象台，天津 300074；2. 国家海洋信息中心，天津 300171；3. 国家气候中心，北京 100081；
4. 北京师范大学，北京 100875）

摘 要：本文详细介绍了 SIS 海冰模式中引进两种盐度参数化方案即等盐度方案和盐度廓线方案对海冰模拟所存在的差异。利用盐度廓线方案导出的表征盐度与海冰温度间关系的方程比等盐度方案多出一项，将定义为盐度差异项。盐度差异项对海冰厚度的热力作用表现为：在海冰厚度增长季节（11 月到次年 5 月），盐度差异项通过升高海冰内部温度，抑制海冰增长；在消融的第一阶段（6-8 月），盐度差异项通过升高海冰内部温度加快海冰消融；在消融的第二阶段（9-10 月），盐度差异项通过降低海冰内部的温度抑制海冰消融。但尺度分析表明，盐度差异项要比方程中队海冰温度作用最大项小 1-2 个量级，如果采用一级近似，可以略去盐度差异项，因此盐度差异项对海冰增长和消融影响很小。同时利用冰洋耦合模式（Modular Ocean Model，MOM4），分别采用两种盐度参数化方案模拟北极海冰厚度和海冰密集度的季节性变化，模拟结果也表明两种方案模拟得到的海冰厚度和海冰密集度的季节性变化相差甚小。

关键词：北极；海冰模式；盐度参数化方案

Seasonal evolution of the Northern Yellow Sea cold water mass

LI Xi-bin[1, 2], SUN Xiao-yan[3*], ZHANG Qiu-feng [1, 2], NIU Fu-xin[1, 2], YAO Zhi-gang[4, 5]

1. *Tianjin Marine Environmental Monitoring Central Station, State Oceanic Administration (SOA), Tianjin* 300451, *China;*

2. *Tianjin Marine Environmental Monitoring and Forecasting Center, Tianjin* 300451, *China;*

3. *National Marine Data and Information Service, Tianjin* 300171, *China;*

4. *College of Physical and Environmental Oceanography, Ocean University of China, Qingdao* 266100, *Shandong province, China;*

5. *Physical Oceanography Laboratory, Ocean University of China, Qingdao* 266100, *Shandong province, China;*

Abstract: With the in-situ temperature and salinity observations taken seasonally in the Northern Yellow Sea area during the National 908 Water Investigation and Research Project from 2006 to 2007, the characteristics of the Northern Yellow Sea cold water mass (NYSCWM) were studied, including both its spatial pattern over the whole bottom and historically typical section from Dalian to Chengshantou. Seasonal evolution as well as its spatial distribution was analyzed to further understand the NYSCWM, as a result, some new features about the NYSCWM had been found. Compared to the previous studies, the center of colder water mass in summer moved eastward, but sharing the similar peak values for both temperature and salinity with historical data. In spring, the axis of 32.8 psu saltier moves westward approximately 75 km and the high salinity areas beyond 123.5° E were largely impaired comparing to that in winter. In winter, the NYSCWM almost disappeared due to the reinforced wind-induced mixing and the Yellow Sea Warm Currents (YSWC) moved northward and controlled most of the Northern Yellow Sea region. In autumn, two cold centers with the peak value of 9℃ were found inside the attenuated NYSCWM.

Keywords: the Northern Yellow Sea cold water mass; seasonal evolution; temperature and salinity distribution; Yellow Sea warm current

Received on Jun. 6, 2013

*Corresponding author: luckysunxy@126.com

1 Introduction

The Yellow Sea is a semi-enclosed shallow sea, and the most significant feature of its seabed topography is that a northwest-southeast direction trough presents in the central South Yellow Sea with water depth approximately 50 m - 80 m. The trough becomes shallower and turns to the east-west direction in the Northern Yellow Sea.

In addition, topographies of both sides of the trough are asymmetrical obviously. To the west, the former sea topography of Yellow River Delta at the Subei Coast is relatively flat, while sea topography of the east side of the trough which is close to the Korean peninsula is significantly more precipitous than that of the west side. Generally, the Yellow Sea is divided into northern and southern parts bounded by the Shandong Chengshantou and the Korean long mountain string (with the widthof 193 km) [1]. The north region of the boundary is the Northern Yellow Sea which is our study area. Average water depth of the Northern Yellow Sea is only 38 m which is relatively shallower than that of the Southern Yellow Sea. In the Northern Yellow Sea, the most striking feature of hydrology is the existence of the Northern Yellow Sea cold water mass (NYSCWM). Researches of NYSCWM distribution and evolution are pretty valuable to the understanding of issues, such as the hydrodynamic environment in North Yellow Sea area, air-sea interaction, ecological element distribution and water exchange of the Bohai Sea with the open sea et al.

2 Data used

Data used in this paper is from seasonal observations of the Bohai Strait and Northern Yellow Sea area obtained by cruises of *Dongfanghong* No. 2 of Ocean University of China during the National 908 Water Investigation and Research Project from 2006 to 2007. 20 observation sections and 120 observation stations were set up, and the specific locations of stations are shown in Fig. 1a. Observation area covered most North Yellow sea region from the Bohai Strait to 124°E, and the minimum water depth of survey stations was 13 m and the maximum depth is 74 m. Topography of study area is shown in Fig. 1b. Sea Bird 911 Plus CTD was applied to obtain temperature and salinity data in our observation, and the instrument was calibrated prior to the use and the observation data were under the quality control prior to the analysis.

3 Seasonal variation of NYSCWM horizontal distribution

3.1 Horizontal distribution of bottom cold water in summer

Horizontal distribution of bottom cold water in summer can be seen in Fig. 2, from which we can see:

(1) NYSCWM has already formed fully with the minimum temperature about 6 °C. And 6 °C temperature contours were basically zonal, entrenched in the 50 m isobath to the deep trough, and the central location was roughly at 122.4°E and 38.2°N.

(2) Taking the 8 °C temperature contours as the boundary of NYSCWM in summer, we can see NYSCWM was basically in the northwest - southeast direction, which distributed in the range of 121.3°E to 24.0°E, 37.0°N to 38.9°N and covered more than half of the whole study area. Isotherm of landward side of 8 °C contour outer distributed more densely, and temperature difference of cold water core and shore hot water was above 10 °C.

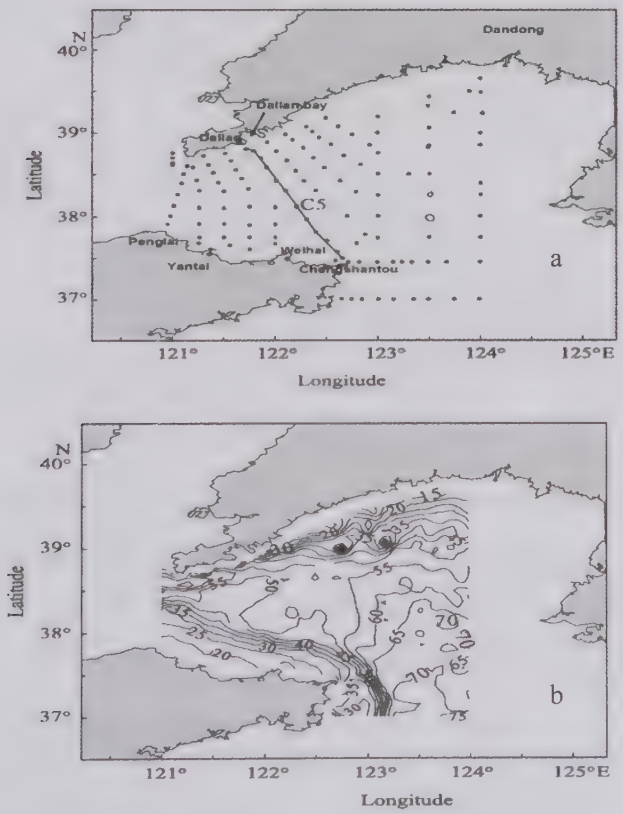

Fig. 1 Stations of the CTD observation (a) and its topography features (b)

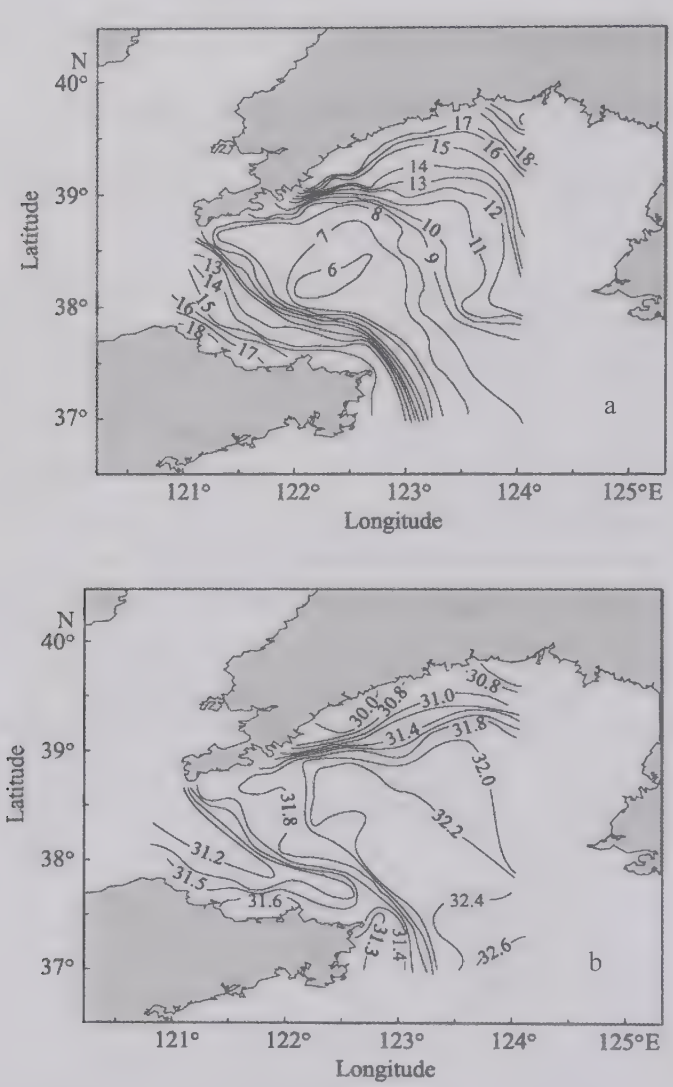

Fig. 2 Distributions of bottom temperature (a) and salinity (b) in summer

(3) Entrenched position of the cold water mass corresponded to high values of salinity, and its salinity was higher than 32 psu. High salt area surrounded by 32 psu salt line covered more than half of our study area. Obvious salinity front formed between high salt and low salt water.

Based on observation data of eight years(1965-1966,1972-1973,1975,1979-1979), Weng [2] pointed out that, during summer maturity period, average location of NYSCWM in most years was located in the north of Weihai city around 122°12′E,38°14′N, and low temperature centers of layers were relatively consistent. Compared with the previous

research, our study shows that low temperature center of NYSCWM was slightly eastward.

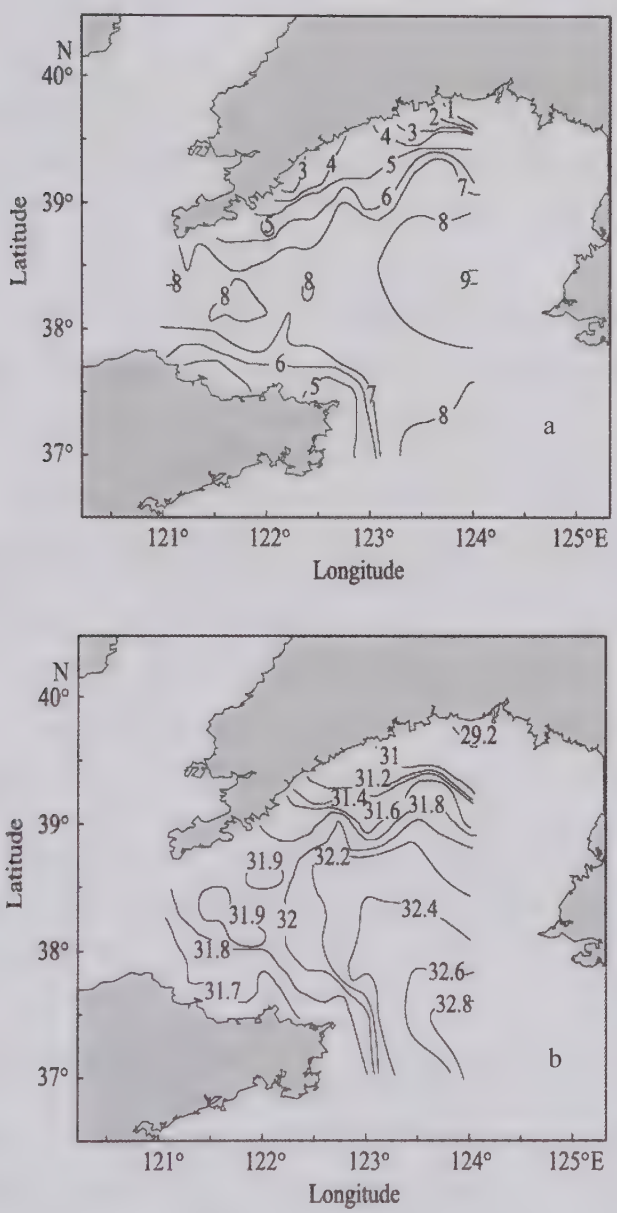

Fig. 3 Distributions of bottom temperature (a) and salinity (b) in winter

3.2 Horizontal distribution of bottom cold water in winter

From the temperature distribution map (Fig. 3a) we can see, NYSCWM has disappeared in winter, and Yellow Sea Warm Currents (YSWC) dominated most area of the Northern Yellow Sea controlled by NYSCWM in summer. The previous cold water

center with temperature below 6 °C now has been replaced by 8 °C - 9 °C water body basically. The temperature distribution throughout the sea basically showed far shore high and near shore low, which was just opposite to summer.

From the salinity distribution map (Fig. 3b) we can obviously see that YSWC invaded northward to the North Yellow Sea in winter, accordingly high salinity water tongue extended to the North Yellow Sea from southeast to northwest. The maximum salinity of the water tongue could reach 32.8 psu, and spindle position of 32.8 Isohaline located near 124°E, 37°N.

3.3 Horizontal distribution of bottom cold water in spring

Spring is a transitional period from winter to summer, water temperature distribution of bottom cold water mass in spring can be seen in Fig. 4. From Fig. 4a, we can see the control of YSWC more weakened in summer than that in winter, and cold water in the middle of the Northern Yellow Sea became to form, and 6 °C cold water covered the area range of 121 - 123°E, 38° - 38.8°N, which accounted for about 1/3 of our total investigation area. Water temperature of shallow shore area increased from 3 °C - 4 °C in winter to 7 °C - 8 °C in spring. Water temperature of the Northern Yellow Sea bottom cold water center was difference between the shore water, that was about 2 °C - 3 °C.

From the salinity distribution map (Fig. 4b), salinity of cold water area of the Northern Yellow Sea was still high, and its value was greater than 32 psu. Compared with that in winter, distribution patterns of high saline tongue changed a lot. Spindle position of 32.8 psu in spring shifted from 124°E in winter to 123.3°E, which moved westward more than 75 ke. And high salinity (salinity higher than 32.8 psu) water area in winter which located to the east of 123.5°E reduced its northward extension greatly, and it degenerated into a weaker little high saline tongue.

In our investigation, winter voyage was during the time period from Dec. 30 to Jan. 17 of the next year, spring voyage was during the time period from Apr. 22 to May 5. Bottom cold water temperature of the Northern Yellow Sea was lower in spring than in winter, which indicated that bottom cold water temperature of the Northern Yellow Sea continued to decrease during the time period from the end of winter voyage investigation to the beginning of summer voyage investigation, at least in February of the winter. Comparing the two investigation results of spring with winter voyages showed that the cooling rate of bottom cold water of the Northern Yellow Sea reached 2 °C. By comparison, 6 °C cold water of the Northern Yellow Sea low layer occupied much larger area in spring than in summer, difference between the two had reached more than 10 times, which also reflected that in the transition period from spring to summer, vertical turbulent mixing and advection

transport and other factors played an important role in the Yellow Sea cold water mass formation [3].

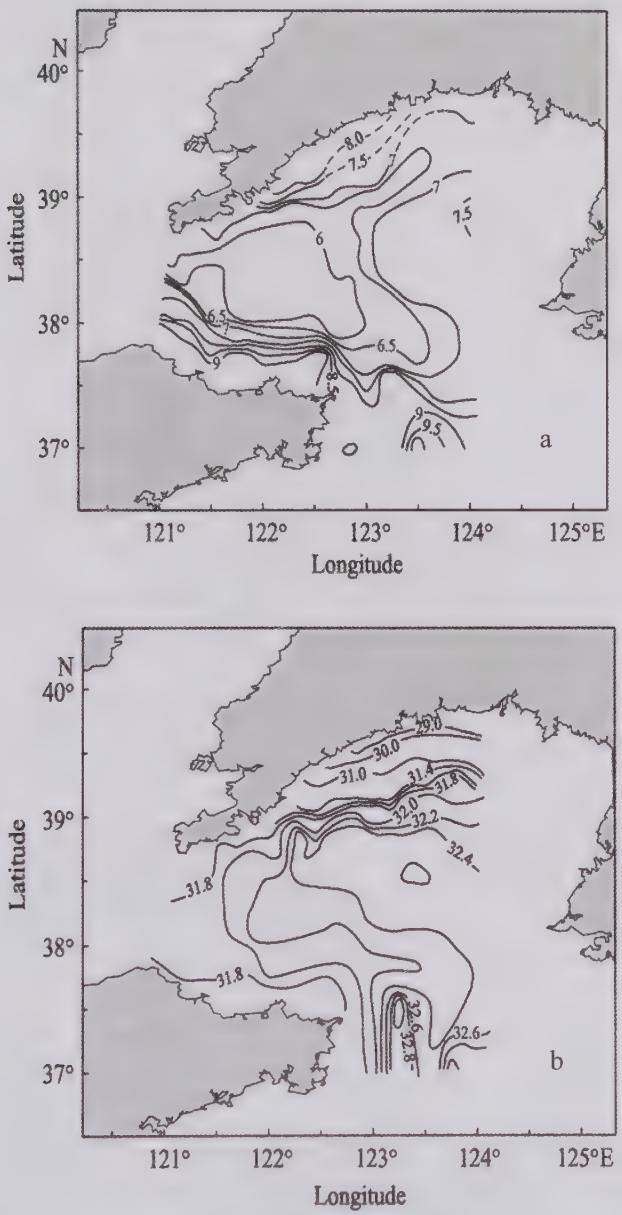

Fig. 4 Distributions of bottom temperature (a) and salinity (b) in spring

3.4 Horizontal distribution of bottom cold water in autumn

Autumn is the transitional period from summer to winter. From Fig. 5a we can see that vertical turbulent mixing intensity is caused by winter stress enhances, and mixing of

the upper water makes the strength and scope of NYSCWM weakened. Weakened NYSCWM presents two low temperature centers in autumn, which are located at 122°E, 38.3°N and 122.4°E, 38.7°N, and both cold center temperatures are 9 °C. Despite in autumn, cold water temperature in central of the Northern Yellow Sea has increased, comparing with that in summer, and the middle cold water and coastal water still maintain a large temperature gradient, Central cold water and coastal water temperature difference reaches about 9 °C - 10 °C.

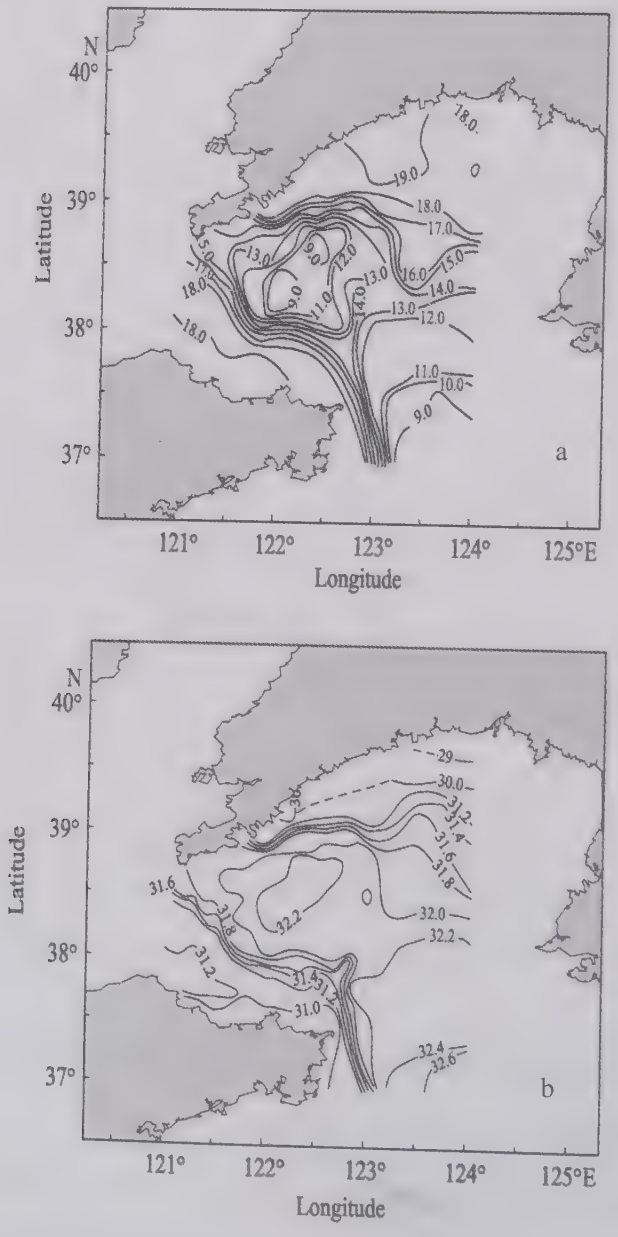

Fig. 5 Distributions of bottom temperature (a) and salinity (b) in autumn

From the salinity distribution map (Fig. 5b) we can see that high salinity center is still located nearby 38.5°N, 122.5 °E. Similar to the temperature distribution, taking the connection 122.5°E, 38°N with 123.3°E,38.3°N as the boundary, the entire of the Northern Yellow Sea can be divided into two parts, and the northwest of the connection shows gradual disappearance of NYSCWM and southeast of the connection shows Yellow Sea Warm Current northward invasion. In autumn, NYSCWM displays two 9 °C low temperature centers, which has not yet been mentioned or discovered in previous studies. On the one hand, this finding was largely attributable to the survey stations laid much more intensive than before, making it possible for further and more sophisticated understanding on thermohaline structure of the Northern Yellow Sea region. On the other hand, whether this discovered dual-nuclear structure of the Northern Yellow Sea cold water in autumn had climatological characteristics or single instantaneous observations still need further research.

3.5 Seasonal variation analysis of NYSCWM distribution

Based on the analysis of NYSCWM thermohaline distribution in four seasons, we can see that NYSCWM begins to form in spring and becomes fully mature in summer, and in autumn, NYSCWM begins to weaken and disappears completely until winter.

Based on the observation data of 42 years (1928 - 1931, 1933 - 1940, 1943, 1957 - 1967, 1972 - 1973 and 1975 - 1990) Zhang [4] pointed out that variation range of low temperature core of NYSCWM was 4.03 °C - 8 °C, with average value about 5.9 °C. And salinity variation range of low temperature core was 30.79 psu, and annual average was approximately 32.01 psu. In our study, temperature of low temperature core was about 6 °C and salinity was about 32 psu, which showed that our survey results coincided with previous observations.Compared with historical data, temperature and salinity of low temperature center of NYSCWM changed little.

4 Conclusions

(a) In winter, NYSCWM has already disappeared basically, and its temperature range is about 8 °C - 9 °C. The temperature gradually decreases to shore in the middle of the Northern Yellow Sea. High salinity water of Yellow Sea Warm Current displays tongue pattern and extends to northwest. The maximum salinity of the water tongue could reach 32.8 psu.

(b) In spring, cold water feature in the middle of the Northern Yellow Sea shows up, and 6 °C cold water covers 1/3 of our total investigation area. Salinity of cold water center

area of North is greater than 32 psu. Spindle position of high salinity water tongue which locates to the east of Chengshantou shifts from 124°E in winter to 123.3°E in spring, and the previous 32.8 psu high salinity water tongue degenerates into a weaker little high saline tongue.

(c) In summer, NYSCWM has already formed fully with minimum temperature about 6 °C and salinity larger than 32 psu, which entrenches in the 50 m isobath to deep trough, and temperature difference of cold water core and shore hot water could reach 12 °C. Obvious salinity front forms between high salt and low salt water. Compared with previous researches, our study shows that low temperature center of NYSCWM is slightly easterly. But temperature and salinity of cold water center change little.

(d) In autumn, NYSCWM weakens, which is caused by the upper water mixing, and weakened NYSCWM presents two low temperature centers. High salinity center is still located nearby 38.5°N, 122.5 °E, which is similar to the temperature distribution.

References

[1] Sun X P. China offshore seas [M]. Beijing: Ocean Press of China, 2006: 376.

[2] Weng X C, Zhang Y K, Wang C M, et al. The variational characteristics of the Yellow Sea cold water mass [J]. Oceanologia Et Limnologia Sinica, 1988, 19(4): 368 - 379.

[3] Xia C, Qiao F, Yang Y. Three-dimensional structure of the summertime circulation in the Yellow Sea from a wave-tide-circulation coupled model [J]. Journal of Geophysical Research-Oceans, 2006, 111(C11): C11S - C13S.

[4] Zhang Y K, Yang Y L. Analyses of the variational characteristics of the north Huanghai sea cold water mass [J]. Marine forecasts, 1996, 13(004): 15 - 21.

北黄海冷水团季节变化特征分析

李希彬[1,2]，孙晓燕[3]，张秋丰[1,2]，牛福新[1,2]，姚志刚[4,5]

（1. 国家海洋局天津海洋环境监测中心站，天津 300451；2. 天津市海洋环境监测预报中心，天津 300451；
3. 国家海洋信息中心，天津 300171；4. 中国海洋大学海洋环境学院，山东 青岛 266100；
5. 中国海洋大学物理海洋教育部重点实验室，山东 青岛 266100）

摘 要：基于 2006 至 2007 年“908”项目执行期间春夏秋冬共四个航次的 CTD 温盐数据，针对四个季节底层大面及大连-成山头断面温度和盐度的分布特征，分析了北黄海冷水团的季节变化，初步探讨了其消长过程，并与历史资料相比较，发现了关于北黄海冷水团的新问题。研究表明：夏季，北黄海冷水团温度和盐度与历史资料相比，低温中心位置存在东偏，但低温中心温度和盐度变化不大。春季，32.8 psu 高盐水舌主轴位置较冬季偏西约 75 km，123.5°E 以东的原冬季盐度高值区的范围向北延伸的势力大减，退化为较弱的小高盐水舌冬。冬季，北黄海冷水团已经消失，黄海暖流呈舌状向北延伸。秋季，减弱的北黄海冷水团存在两个中心温度约 9 °C 的低温中心。

关键词：北黄海冷水团；季节变化；温盐分布；黄海暖流

Effect of sea surface wind on the seasonal variation of sea level in the east of China seas

MU Lin[1], CHI Yong-xiang[2, 3], LIU Shou-hua[1, 4, 6], SONG Jun[1, 5], LIN Xiao-pei[5], LI Yan[1], ZHANG Jian-li[1]

1. *National Marine Data and Information Service, Tianjin* 300171, *China*;

2. *College of Physical and Environmental Oceanography, Ocean University of China, Qingdao* 266100, *Shandong province, China*;

3. *Yantai Environment Monitoring center of SOA, Yantai* 264006, *Shandong province, China;*

4. *The Second Institute of Oceanography, SOA, State Key Laboratory of Satellite Ocean Environment Dynamics, Hangzhou* 310012, *Zhejiang province, China;*

5. *Physical Oceanography Laboratory, Ocean University of China, Qingdao* 266100, *Shandong province, China;*

6. *Key Laboratory of Ocean Circulation and Waves, Chinese Academy of Sciences, Qingdao* 266071, *Shandong province, China*

Abstract: Sea level seasonal variations in the east of China seas from 2004 to 2006 are simulated by the advanced ROMS model. The results show similar sea level spatial features with TOPEX/Poseidon observations, with annual ranges decreasing gradually from the sea coast to the Kuroshio region. By getting rid of wind stress in ROMS model, the simulated sea level results still show obvious seasonal variations. However, the phenomenon of sea level anomaly disappears in Min Zhe Current Coastwise (MZCF) and Su Bei current coastwise (SBCF), and the change of it from coastal area to ocean recedes. The seal level difference between Bohai, Yellow Sea (BYS) and East China Sea (ECS) becomes weaker in spring and autumn. The annual differences decrease obviously, and the gradual change of annual ranges from seacoast to the Kuroshio almost disappears. The annual ranges in BYS are nearly identical. The annual range ratio without the wind stress to with the wind stress increases gradually from the sea coast to Kuroshio region.

Keywords: sea level; seasonal variation; numerical simulation; sea surface wind

Introduction

Global warming is a serious reality that has received much attention since last

Received on Oct. 29, 2012

Corresponding author: moulin1977@hotmail.com

decades. In recent years, human activities play an important role in the global climate changes by emissions of greenhouse gases such as carbon dioxide. It is believed that an abrupt climate change in the global climate system around 1976 causes many impacts such as the increase of sea surface temperature, sea level rise and weakening of the East-Asian summer and winter monsoons.

Researches show that the TOPEX/Poseidon (T/P) sea level and steric sea level all have significant seasonal variations. And, there are obvious sea level seasonal variations in China seas (Zhang, 2006; State Ocean Administration, 2008). Sea level seasonal variations in the ECS are caused by monsoon, coastal current system, and atmospheric static pressure effect. Whereas, the sea level seasonal variations in South China Sea are almost caused by monsoon currents (Li et al., 1982). Zhan et al., (2003) presented the sea level time-frequency characteristics of the Yellow Sea, ECS and South China Sea, which showed similar sea level change features such as dominant anniversary signal and the weaker half of the periodic signal in the Yellow sea and ECS. However, the periodicity and intensity of sea level seasonal variations show significant differences in the Yellow sea and ECS. Yan (2008) found that the T/P sea level seasonal variability was mainly caused by the steric effect, accounting for about 92%. There are obvious T/P sea level variations in ECS, which are closely related to the steric sea level changes, but the amplitudes of T/P sea level seasonal variations are smaller than that of steric sea level (Yan, 2008).

At present, our knowledge on how the sea level seasonal changes in the east of China Seas is still limited. Thus, in the paper we simulate the seasonal variations of sea level from 2004 to 2006 in the east of China Seas by ROMS (Song, 2010) and analyze the difference between the simulation and T/P observation. Further, some sensitivity experiments are conducted to explore the influence of sea wind on the sea level seasonal changes and annual range characteristics.

1 Experimental design

First, some basic assumptions are set in ROMS, which include free surface, hydrostatic and Boussinesq approximation, and primitive equations.

Two experiments are conducted, which are basic experiment and comparative experiment. Considering the impact of Kuroshio on ECS and the simulation accuracy, the model is set in the domain of 99°E - 145°E, 9°S - 52°N, with 6'×6' horizontal grid resolution and 33 layers in vertical direction. The previous simulation results (Song, et al, 2011) are used as initial and open boundary conditions to drive the model, which is conditioned at the top interface including shortwave radiation, long-wave radiation,

sensible heat and latent heat flux, evaporation and precipitation, and wind stress. The blended sea wind from the National Center for Environmental Prediction (NCEP) with a spatial resolution of 1/4°×1/4° and a temporal resolution of one day are used to compute the wind stress. Sea surface height, horizontal current velocity, temperature and salinity are considered in the open boundary conditions. In order to find out the role of wind in sea level seasonal variations, the comparative experiment with getting rid of wind stress is constructed.

2 Results and discussion

In our study, the data are seasonally averaged in spring (December to February), summer (March to May), autumn (June to August) and winter (September to November). The area we focused on is 116°E - 132°E，20°N - 41°N. T/P data from January 2004 to December 2006 are used for the comparison with simulations. Multi-year mean sea level height in this paper is calculated for the periods of 1993 - 2010.

2.1 Sea level height anomaly from simulations and the T/P data

The seasonal variability of SSHA from T/P observation and the simulation results are analyzed. The spatial distribution characteristics of simulation agree well with the T/P data results. In the Northwest of Taiwan and Ryukyu Islands, the spatial distributions are similar except some small difference. However, there are big deviations in Japan Seas.

Sea level height anomaly is negative in winter over the east of China Seas and the minimum area is in Bohai Sea. Comparing with the whole east China Seas, SSHA in the northwest of Taiwan and MZCF are higher (Fig.1d, Fig. 2d). In spring, SSHA in YBS and Ryukyu Islands is higher than that in the ECS. As a result of the monsoon transition in spring, the positive SSHA spreads from the two ends of China Seas to the middle and leads to the high negative SSHA over MZCF and the north of Jiangsu. (Fig. 1a and Fig. 2a).

It shows that there is positive SSHA in the east of China Seas in summer, which has the maximum SSHA value of the four seasons. However, the east areas of Taiwan and the MZCF have the negative SSHA (Fig. 1b and Fig. 2b). As we known, Asian monsoon transit occurs in autumn. Thus, SSHA in BYS becomes lower than that in ECS. It also has generated a positive SSHA region in MZCF and the north of Jiangsu (Fig. 1c and Fig. 2c). The spatial distribution is similar in spring and autumn, and also in summer and winter, but it has the contrast in phase mode.

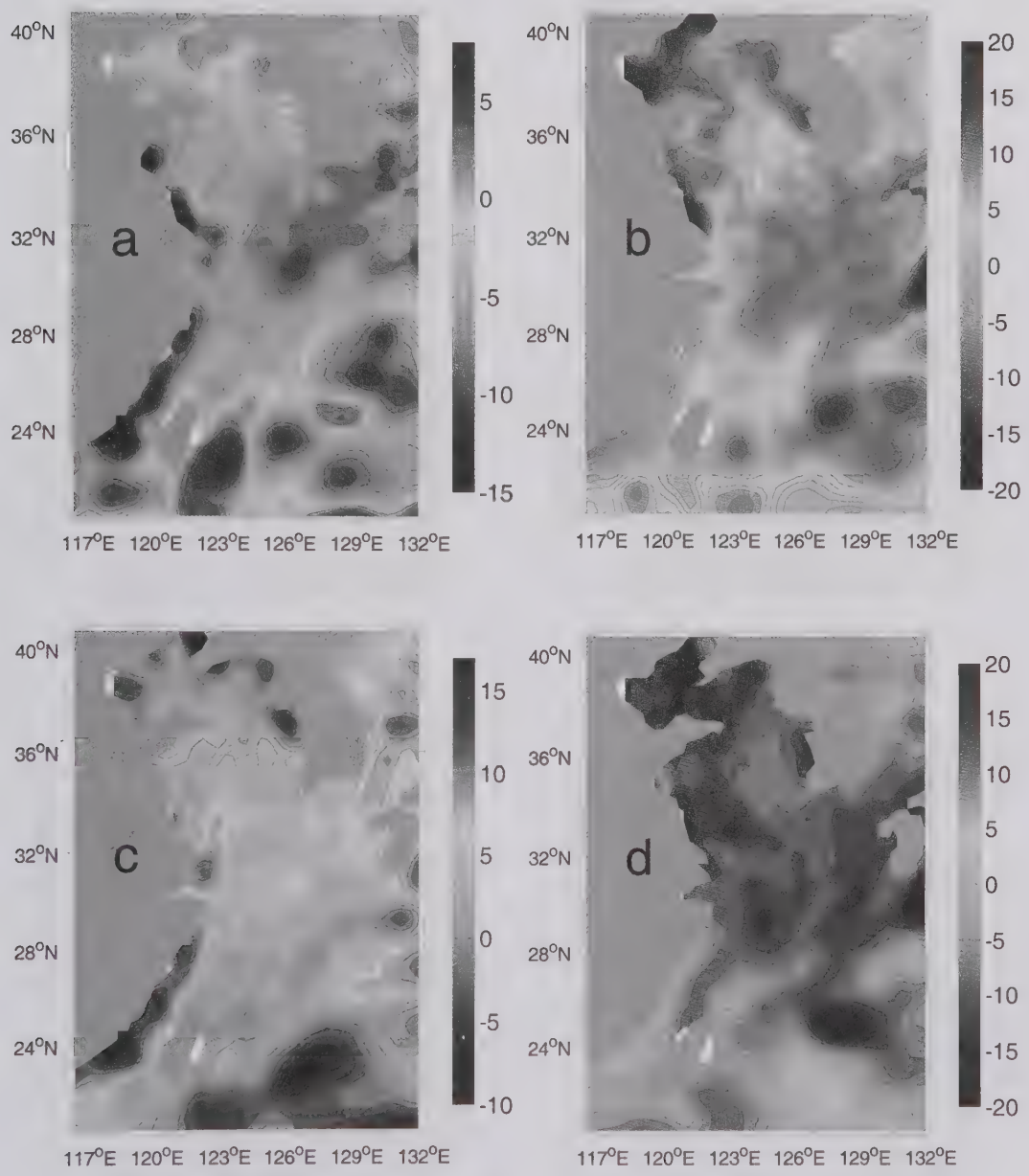

Fig. 1 Variability of SSHA in the east of China Seas from T/P data (unit: cm)

(a) the SSHA in spring; (b) the SSHA in summer; (c) the SSHA in autumn; (d) the SSHA in winter

SSHA in the east of China Seas is lowest in winter with the minimum less than -20 cm, and highest in summer with the maximum value higher than 25 cm. In the west of Taiwan, there is a lower SSHA region in spring with the minimum value less than -15 cm, and a higher SSHA region in the northeast, with the maximum one higher than 8 cm. In autumn, there is a high SSHA region in the east of Taiwan and a low SSHA region in the east.

Comparing the simulation results with the T/P observation data, the SSHA is lower in spring and winter, but higher in summer and autumn.

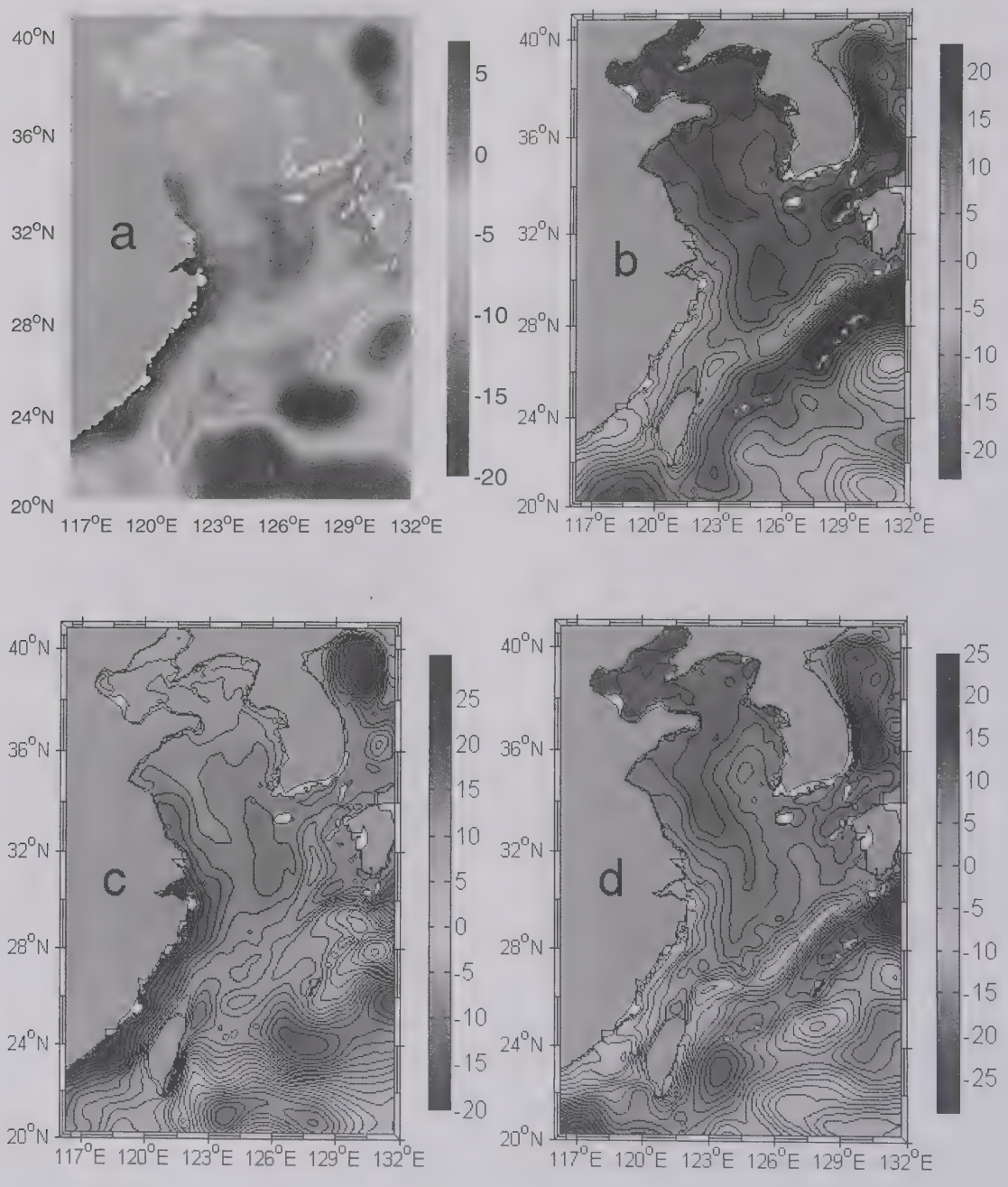

Fig. 2 Variability of SSHA in the east of China Seas from basic experiment simulation (unit: cm)

(a) the SSHA in spring; (b) the SSHA in summer; (c) the SSHA in autumn; (d) the SSHA in winter

The spatial distribution characteristics are similar between the simulations and the

T/P data except some small differences. In spring, eddies are less in number and larger in area in the southeast of Ryukyu Islands, compared with the T/P results. In summer and winter, the simulation results show good Kuroshio path, which is not obvious in T/P data. In autumn, the simulated results of basic experiment present positive SSHA characteristics in the east of China Seas.

2.2 Annual range comparisons between simulations and T/P results

The annual range of sea level is defined as the difference between the maximum monthly average sea level and the minimum monthly average sea level, which is an important factor of sea level seasonal variability.

From the annual range figure of simulation and T/P data from 2004 to 2006 (Fig. 3a and Fig. 3b), they show similar features in the spatial distribution. The annual range becomes smaller from nearshore to the deep ocean, which is attributed to the monsoon in this region. In winter, the northwest wind drives out sea water to the deep ocean and in summer, the southeast wind forces sea water stacking in the nearshore (Fig. 3a and Fig. 3b). There is a high region of annual range in the southeast of Ryukyu Islands of Taiwan. The simulation results are higher than the T/P data in annual range as a whole. In the north of the coastal area of Jiangsu, there is a region with false extreme annual range because of the terrible accuracy of T/P data in the shallow water.

2.3 Analysis of sea wind influence on the sea level seasonal variability in the east of China seas

We analyze the results of comparative experiment from 2004 to 2006 in the east of China Seas. In spring, it has positive SSHA modes around Taiwan and negative SSHA modes in BYS and in the north of ECS, and SSHA value reaches highest in the northeast and south of Taiwan (Fig. 4a). In summer, most regions have positive SSHA modes except the regions along the latitude directions from 20° to 22° (Fig. 4b). In winter, Taiwan and the Ryukyu Islands act as a role of boundary line of zero SSHA, the south of which is negative region and the north of which is positive region (Fig. 4c). While in winter, the boundary line of Taiwan and Ryukyu Islands changes its direction, the northwest of which is negative and the southeast of which is positive (Fig. 4d). Just like the basic experiment, the spatial distribution is similar in spring and autumn, and also in summer and winter, but contrast in the phase mode. Compared with the basic experiment, the comparative experiment also shows obvious seasonal variability although the wind influence is removed. It indicates that the sea level variations are controlled by lots of other factors, such as steric effect, air temperature, air pressure and so on. In the comparative experiment, the phenomenon of negative SSHA in spring, summer and positive SSHA in autumn and winter disappears.

The SSHA changes from coast to the deep sea become weaker. In spring and autumn, the difference of SSHA between the ECS and BYS, the Ryukyu Islands is smaller than that in the basic experiment. Also, in the southeast of the Ryukyu Islands, extreme phenomenon zone of alternating positive and negative SSHA weakens. The results are caused by the sea winds, which drive the water level spread in another way. In the east of China Seas, the wind direction changes from northwest to southeast accompanying by different seasons. The amplitudes of SSHA become smaller without wind effects.

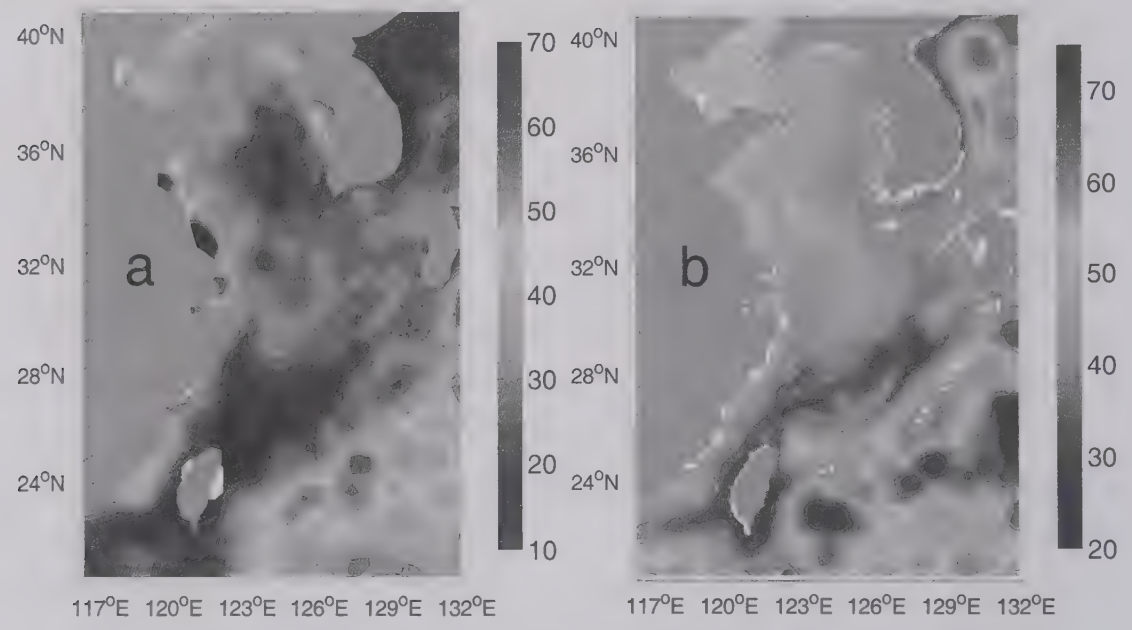

Fig. 3 Annual ranges from the simulation in the east of China seas (unit: cm)

(a) annual range from T/P data; (b) annual range from basic experiment results.

2.4 Sea wind influence on the SSHA annual range in the east of China Seas

Analyzing the SSHA annual range distribution and its proportion in the basic experiment (Fig. 5a), the annual range is smaller comparing with the basic experiment. The SSHA annual range differences from China coasts to the Ryukyu Islands almost disappear. In BYS, the annual ranges are close, all the same (Fig. 5a). From the proportion of comparative results to the basic results (Fig. 5b), the percentage becomes larger from China coasts to the Ryukyu Islands. The proportion in BYS is among 0.4 - 0.6 and beyond 0.6 in ECS. All of these demonstrate that the wind stress plays a more important role in the coastal sea level variability.

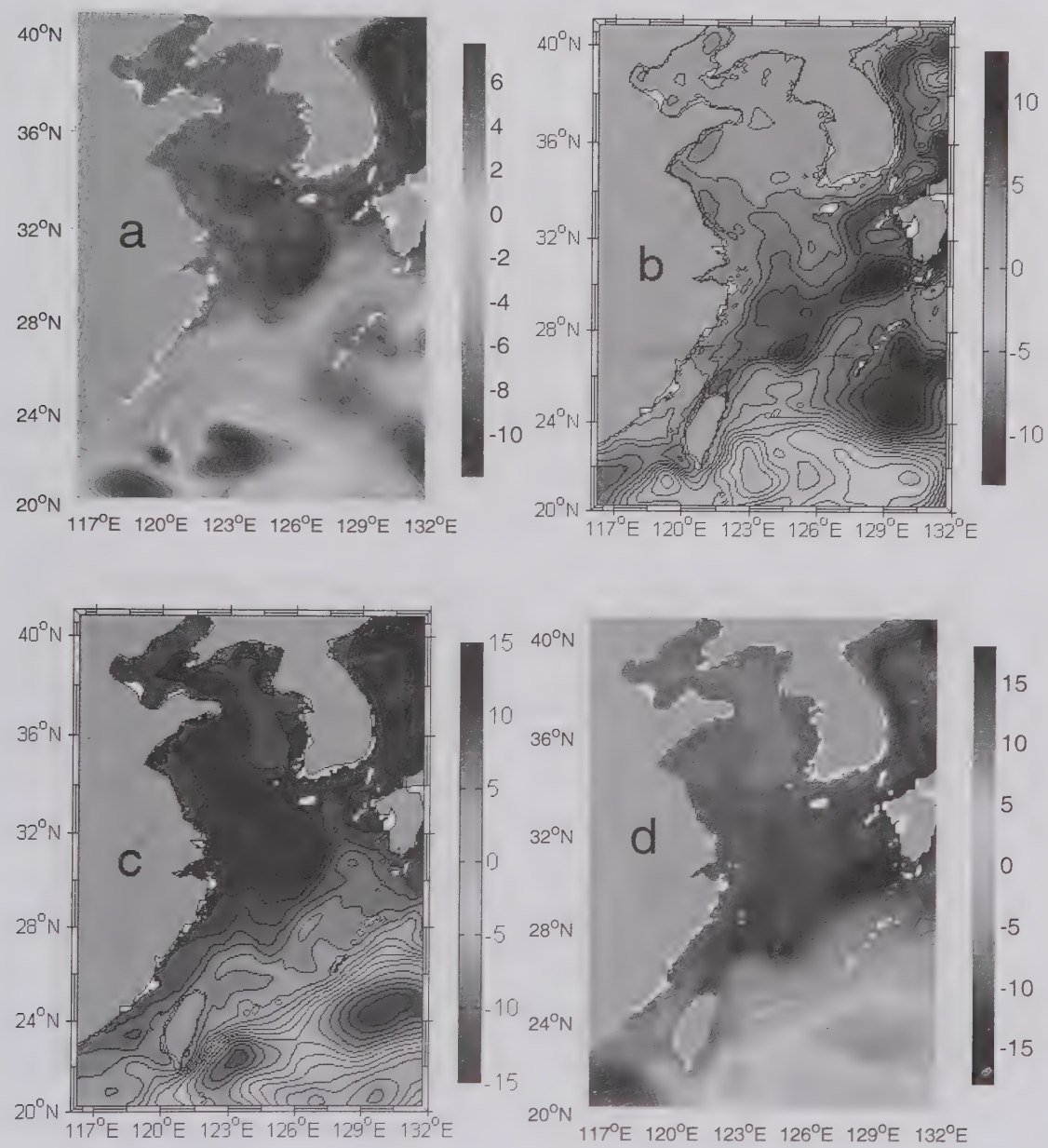

Fig. 4 Sea level seasonal variability in the east of China seas using the comparative experiment (unit: cm)

(a) the SSHA in spring; (b)the SSHA in the summer; (c)the SSHA in the autumn; (d) the SSHA in the winter

3 Conclusions

The sea level seasonal variability from 2004 to 2006 in the east of China Seas is

studied by ROMS simulation and T/P data. The SSHA simulations are mostly similar with T/P data. The annual range in the mainland coast is smaller than that in Taiwan and the Ryukyu Islands nearby. To remove the wind stress influence, it also shows obvious seasonal variations. But the phenomenon of negative SSHA in spring, summer and positive SSHA in autumn and winter almost disappears. Compared with the results with wind force, the SSHA difference between the coast and the deep ocean becomes smaller. In spring and autumn, the difference of SSHA between ECS and BYS, Ryukyu Islands nearby is smaller than that in the basic experiment. Also, in the southeast of Ryukyu Islands, phenomenon of alternating positive and negative eddies weakens. The annual range without wind stress becomes smaller obviously. The SSHA annual range differences from China coast to the Ryukyu Islands almost disappear. In BYS, the annual range is close, all the same (Fig. 5a). From the ratio of comparative results to the basic results (Fig. 5b), the percentage becomes larger from China coasts to the Ryukyu Islands. They are caused by the effect of sea water accumulation driver by the wind force. The accumulation effort is larger in the offshore region and leads to smaller annual range.

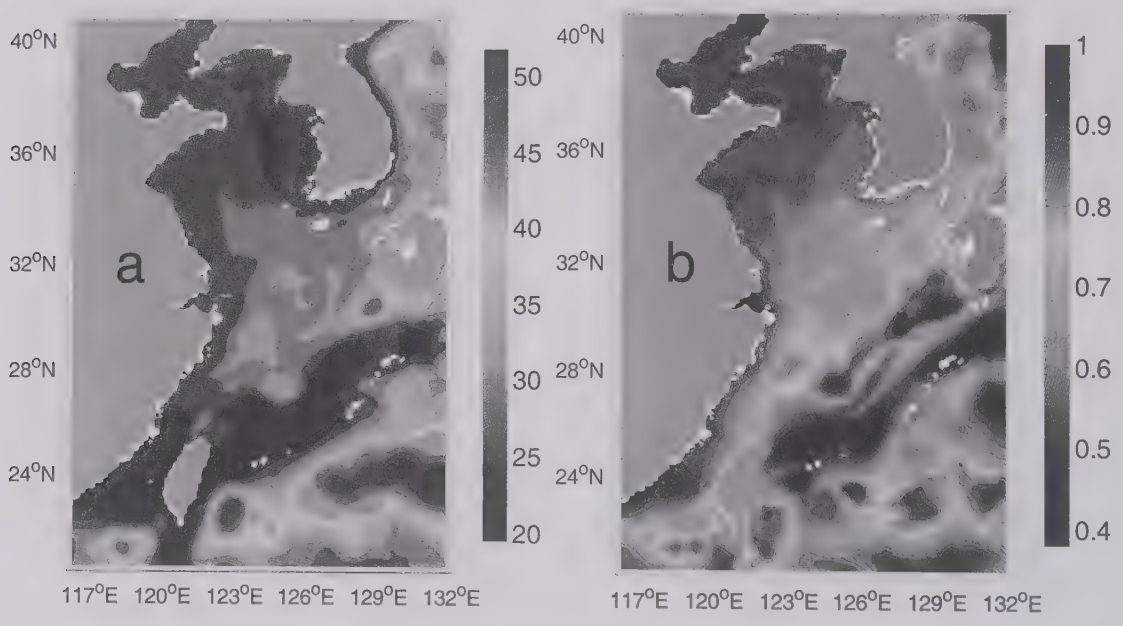

Fig. 5 SSHA annual range distribution of comparative experiment and ratio of comparative experiment to the basic experiment in the east of China Seas

(a) annual range of comparative experiment; (b) the annual range ratio of comparative experiment to basic experiment results

Acknowledgements

This study is supported by the National Natural Science Foundation of China (contract No. 41006002, No.41206013 and No. 41106004); Open Fund of State Key Laboratory of Satellite Ocean Environment Dynamics, Second Institute of Oceanography of SOA (contract No. SOED1305); Open Fund of the Key Laboratory of Ocean Circulation and Waves, Chinese Academy of Sciences (contract No. KLOCAW1302); the Public Science and Technology Research Funds Projects of Ocean (contract No. 200905001, No. 201005019, and No. 201205018; the Natural Science Foundation of State Ocean Administration (contract No. 2012202, No. 2012223, and No. 2012224); Open Fund of Key Laboratory of Physical Oceanography, MOE (contract of Song jun).

References

[1] Cao Y N. The mechanism and the features of seasonal sea surface height in the South China Sea [D]. Ocean University of China, 2007

[2] Li K P, Zhou T H, Chen Z Y. The analysis of monthly average sea level variability and its formation in coastal China [J]. Acta Oceanologica Sinca, 1982(5):529 - 536.

[3] Song J. The study on the theories and methods of water exchange model and its applications [D]. Ocean University of China, 2010.

[4] Song J, Xue H J, Bao X W, et al. A spectral mixture model analysis of the Kuroshio variability and the water exchange between the Kuroshio and the East China Sea [J]. Chinese Journal of Oceanology and Limnology, 2011, 29(2): 446 - 459.

[5] State Ocean Administration. 2008 China sea level bulletin, 2008.

[6] Yan M. The steric effect of global sea level variability [D]. Ocean University of China, 2008.

[7] Zhang J L. The global sea level variability characteristics and the steric effect [D]. Ocean University of China, 2006.

风对中国东部海域海平面季节变化的影响

牟 林[1]，迟永祥[2,3]，刘首华[1,4,6]，宋 军[1,5]，林霄沛[5]，
李 琰[1]，张建立[1]

(1. 国家海洋信息中心，天津 300171；2. 中国海洋大学 海洋环境学院，山东 青岛 266100；
3. 国家海洋局烟台海洋环境监测中心站，山东 烟台 264006；4. 国家海洋局第二海洋研究所 卫星海洋环境动力学国家重点实验室，浙江 杭州 310012；5. 中国海洋大学 教育部物理海洋重点实验室，山东 青岛 266100；
6. 中国科学院海洋研究所 海洋环流与波动重点实验室，山东 青岛 266071）

摘 要：应用ROMS数值模式配置基本实验模拟了2004年到2006年中国东部海域海平面的季节变化。模拟结果与TOPEX/Poseidon(T/P)卫星高度计观测结果基本一致，海平面年较差从中国沿岸到黑潮路径逐渐变小。将数值模式的风应力项去掉，配置对比实验。与基本实验结果对比发现，对比实验海平面仍然具有季节变化，但是闽浙沿岸和苏北沿岸海平面春夏季异常偏低、秋冬季异常偏高现象消失，中国沿岸向太平洋的海平面变化减弱。春季和秋季，渤、黄海和黑潮附近海平面异于东海的现象减弱。对比实验海平面的年较差的数值明显减小，从近岸向黑潮海平面年较差渐变的过程消失。整个渤黄海的海平面年较差近似。对比实验海平面年较差占基本实验海平面年较差比率从近岸向黑潮路径逐渐增大。

关键词：海平面；季节变化；数值模拟；海上风

Study on calculation for the position and scope of tropical cyclone

LIU Yong-lu, SHAO Li-min, LANG Feng-wang

Ocean Meteorology Teaching and Research Section, Dalian Naval Academy, Dalian 116018, *Liaoning province, China*

Abstract: The scale, shape and position are three main factors to forecast tropical cyclone. The aim of the paper is to recognize tropical cyclone (TC) in the satellite cloud pictures according to the scale, shape and position of clouds. The study includes Canny edge detection, contour extraction and other techniques. The solutions are also established. The experiments show that the method can recognize the TC in the satellite pictures. The study is beneficial for TC track.

Keywords: tropical cyclone (TC); Canny edge detection; contour extraction; automation recognition

Introduction

The purpose of this study is to give an easy method to make computer to track the TC from the satellite pictures. The ability to monitor and forecast TC is improved in recent years, but it is not enough to decrease the TC disaster. There are many difficulties not to be overcome. The recognition of TC from satellite cloud pictures is still one of the disturbed topics.

Methods of recognition clouds from satellite pictures mainly include threshold method, multi spectral threshold method, mathematical morphological method, cluster analysis, artificial neural network and wavelet analysis method [3, 4]. TC clouds are different, but TC clouds can be divided into two types, that is one has the eye, and the other has no eye. Above methods can only deal with the TC clouds where there are an obvious eye in the center of clouds [5, 6]. The paper presents an easy method to recognize the TC clouds through the image shape feature and range size. It is suitable for professional persons and also suitable for non-professional persons [7].

As everyone knows, TC structures have nice organization. The TC clouds shape feature is obvious. The scale of TC clouds is also different from other weather system

Received on Oct. 9, 2012

Corresponding author: lyonglu@126.com

clouds. So the scale, the shape and the position can prove that clouds represent TC or not.

The method proposed in this paper is based on the comprehensive analysis from the tropical cyclone cloud shape feature, position and range in size simultaneously. The clouds are determined TC clouds when three requirements are satisfied. This method doesn't consider whether there is the eye in the tropical cyclone and suitable for a variety of different shapes of tropical cyclones. That means that the method is in common use to recognize TC clouds.

1 Methodology

TC clouds have special characteristics, because of its regular spiral appearance. In this paper, we tried to find a method to recognize the TC spiral clouds according to the cloud shape in the satellite pictures.

The cloud shape can be obtained by cloud edge detection. The following step is to determine that the shape, the scale and the center position are conformed to the features of TC clouds in the satellite pictures. If the result satisfies the requirement, then the clouds can be confirmed the TC clouds.

There are many edge detection algorithms. Canny algorithm is the best one to be applied in the TC clouds recognition. Canny algorithm has advantage in dealing with step edge and noise. The basic idea of Canny algorithm is to find the maximum value of image gradient. The gradient is calculated with the derivative of Gauss filter.

$G(x,y)=\frac{1}{2\pi\sigma^2}\exp(-\frac{x^2+y^2}{2\sigma^2})$, that is the Gauss smoothing function

G_x and G_y are respectively, $G(x,y)$ derivatives for x and y

$A=\sqrt{G_x{}^2+G_y{}^2}$, that is the edge strength

$\alpha=arctg\frac{G_y}{G_x}$, that is the angle of G derivative

The edge points will be found through inhibition of edge strength A.

Canny algorithm detects strong edge and weak edge with two threshold values. The weak edge will be obtained only when strong edge and weak edge connect together. Therefore, the method is not prone to be disturbed by noise and can detect the real weak edge.

Edge detection steps are as follows [8].

In the first step, the suitable satellite pictures are selected according to the time. Before the next step, the pictures will be simplified under the map background.

The second step is edge detection.

In the third step, the centroid is calculated on the basis of the TC clouds edge. The distances between centroid and points in the edge can be obtained after centroid calculation.

In the fourth step, the distances can help to determine the scale and shape of clouds. The centroid position is also considered. In the end, three elements confirm whether the focused clouds are TC clouds or not, such as Fig. 1.

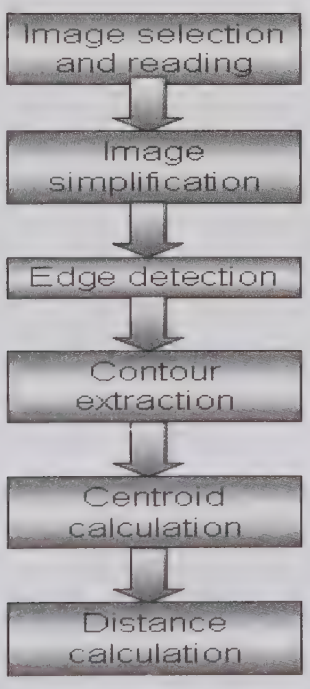

Fig. 1 Flow chart of automatic detection

2 Preprocessing of satellite cloud pictures

In order to decrease the complex degree, the map background of pictures should be eliminated. Because the TC often appears between 30°N and equation, the pictures will be cut to preserve the useful area, such as Fig. 2 and Fig. 3, which are processed with Matlab.

3 Edge detection

Edge extraction is the followed step after the preprocessing of pictures. Before edge detection, the format of pictures should be converted. Because Canny algorithm demands the gray format image, the images should be converted from colorful format to gray format. When Canny algorithm is used [9], the threshold values should be adjusted to the best values, such as Fig. 4. Fig. 4 shows the result after Canny edge detection. In order to simplify the images [10, 11], the useless part will be eliminated. Canny algorithm is used again after the simplification, such as Fig. 5. A clear contour is obtained at last.

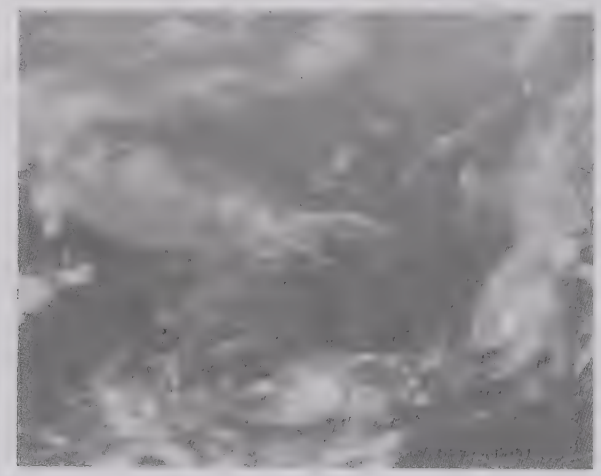

Fig. 2 A raw cloud picture

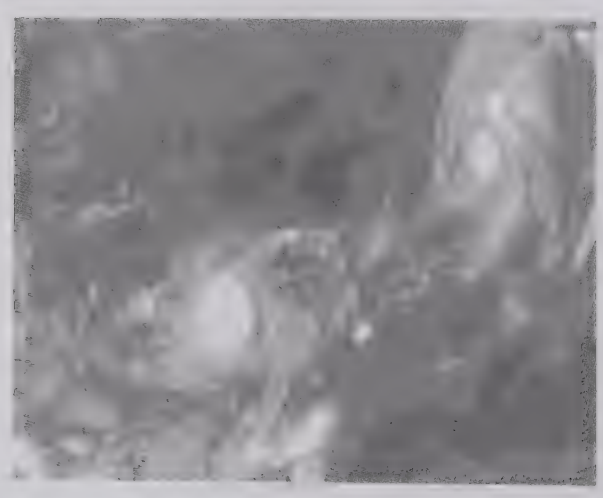

Fig. 3 Image after the process

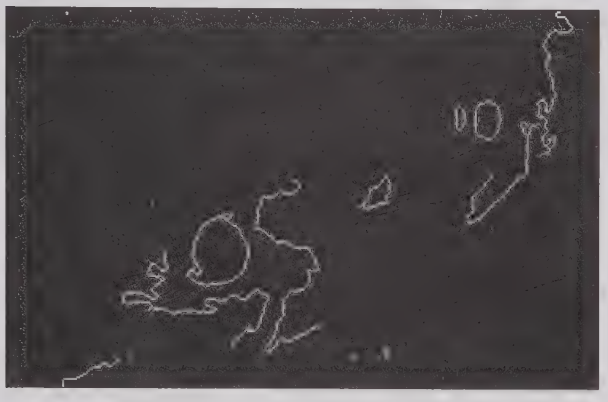

Fig. 4 Image after being processed with canny algorithm

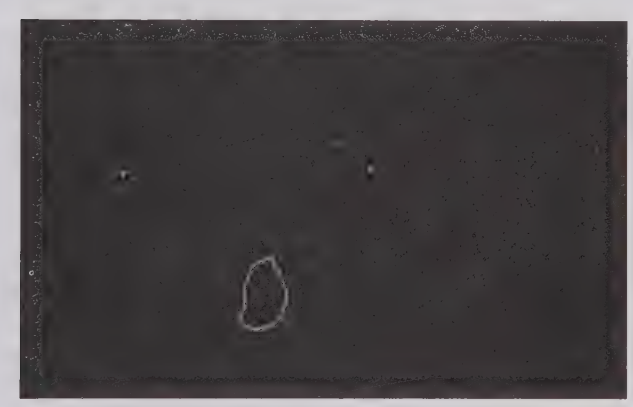

Fig. 5 Image after the simplification

4 Edge extraction with contour method

The edge detection result can not provide the position of edge points. Edge extraction gets the contour of edge [12], that is, edge point coordination is calculated. Matlab provides some functions to solve the edge extraction [13]. The contour method is one of them. Fig.6 shows the edge extraction result.

5 Centroid calculation

Centroid position is the key to determine the scale and shape of clouds. Centroid is not just in the center of contour. In order to make centroid near the center, we only retained the edge and erased other points from the image.

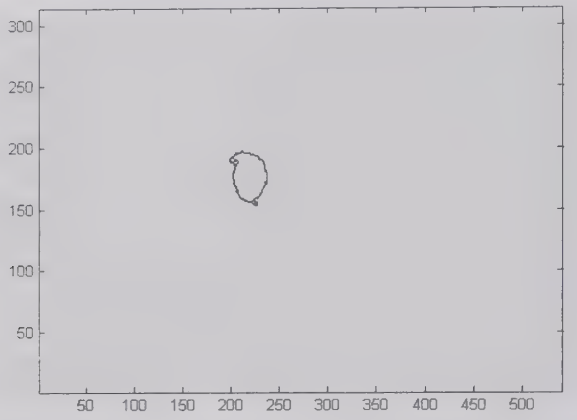

Fig. 6 Contour after being processed with contour algorithm

6 Determination of image characteristics and calculation of the area enclosed by the outline through the distance between centroid and outline point

A reasonable and appropriate handling of images that can be approximated to strike the center of mass as the center of the image is taken before the previous step of finding the centroid, and then the basic characteristics of the image is determined by the distance between centroid and outline point[14].

It is easily to calculate the distance between two points in the MATLAB software environment using the special function distance.

The outline is extracted by the function contour, and the coordinates of the point on it are calculated. Each of the distance between the centroid and outline point is computed by the function, and the minimum distance is known by comparing the distances.

The area enclosed by the outline of the image can be calculated in order to further verify the experiment concluded, and it is verified by the magnitude from the side.

7 Data analysis

7.1 Experiment results

A group of data is obtained through the above experiment:

Centroid coordinates are as [x,y]=[217.7778,177.5231];

Outline matrix C are as follows:

Columns 1 through 4

000.1000 193.0000 193.1000 194.0000

183.0000 190.9000 191.0000 191.9000

.....

Columns 4149 through 4152

235.0000 235.0000 235.0000 235.0000

177.0000 178.0000 179.0000 179.0000

By comparing, the minimum distance is 15.2662, and the magnitude of area enclosed by the outline of image is 8016.

7.2 Analyses of results

According to the design, the magnitude 15.2662 is the minimum distance between centroid and outline points.

By comparing the latitude, longitude values and pixel coordinate values on the original image, we can get the relationship between the image pixel distance and actual distance in nautical mile. Similarly, two points of ten latitudes apart are taken on and the distance is calculated: the pixel distance is 68.6867; actual distance is 600 nautical miles. If there is a straight line through the centroid point and it intersects with contour lines at two points, so that the distance between those two points is greater than two times of the minimum distance between centroid and outline points. Furthermore, we can conclude that the minimum distance between two points intersected with the outline by a straight line through the image center point is 266.7 nautical miles, and it already reach to the standard of tropical cyclone vortex area. So we can confirm that the satellite cloud image contains tropical cyclone cloud system.

In addition, the area enclosed by the image outline is 8 016. By comparing the pixel area and the actual area, it is obviously that the area of image outline already reaches the standard of tropical cyclone vortex area. This also verifies the conclusion of the experiment.

8 Conclusions

(1) There is no standard for processing the image edge, and it needs series

experiment of threshold adjustments.

(2) Striking image centroid is not the process of striking a center point of the image, but makes the centroid point close to the image center after external image processing. Therefore, the center of the image is an approximation, and cannot completely be the accurate reflection of the image feature.

(3) It is a cumbersome and complex work to determine shape features of cloud image through the distances between centroid and outline points, and it needs a large number of repeated experiments to make corrections and adjustments in order to achieve the best results.

Acknowledgements

This paper is supported by the Liaoning Natural Science Foundation (No. L2010055).

References

[1] Wang Guihua, Su Jilan, Ding Yihui, et al. Tropical cyclone genesis over the South China Sea [J]. Journal of Marine Systems, 2007, 68(3): 318 - 323.

[2] Ka Yan Wong, Chi Lap Yip, Ping Wah Li. Automatic tropical cyclone eye fix using genetic algorithm [J]. Expert Systems with Applications, 2008, 34(1): 643 - 648.

[3] He Li, Qin Danyu, Huang Xiaoyan, et al. The Application of FY2 Satellite Cloud Image Analysis System to the Process of Tropical Cyclone Kammuri [J]. Meteorological Monthly, 2010, 10(3): 35 - 50.

[4] Pan Jieli, Zhu Ming, Zhu Jinghai, et al. An algorithm using satellite image data for the forecasting of tropical cyclone path [J]. Journal of Oceanography in Taiwan Strait, 2009, 22(3): 425 - 432.

[5] Tsonis A A. Single Threshold and Rain Area Delineation from Satellite Imagery [J]. APP. Meteor., 1998, 31(2): 1 302 - 1 306.

[6] Chen Hongyi, Zhang Mei. Practical Skills of Using Satellite Cloud Pictures in Tropical Cyclone Forecasting [J]. Meteorological Science and Technology, 2008, 11(4): 574 - 581.

[7] Yu Jianbo. The Research on the Recognition of the Classification of Cloud, Typhoon Segmentation and Locating of the Typhoon's Centre Based on the Meteorological Satellite Cloud Image [D]. Wuhan University of Technology, 2008, 110 - 115.

[8] Zeng Mingjian, Yu Bo, Zhou Cengkui, et al. Researches and applications of locating technology for typhoon center on satellite infrared cloud picture [J]. Journal of Tropical Meteorology, 2006, 11(3): 340 - 344.

[9] Gonzalez R C, Woods R E, Eddins S L. Digital Image Processing Using Matlab [M]. Beijing:

Publishing house of electronics industry. 2005: 251 - 270.

[10] Xie Zhendong. Measure on the colored picture edge based on Canny theory [J]. Computing Techniques for Geophysical and Geochemical Exploration, 2007, 22(4): 370 - 378.

[11] Jing Aibin, Liu Qing, Meng xiangzeng. Extraction and Filling of the Outline of Black-and-White Binary Graphics Based on Matlab [J]. Computer Knowledge and Technology, 2008, 8(1): 27 - 32.

[12] Xu Ping, Shao Dinghong, Wei Ying. Optical threshold segmentation and contour extraction technology and its application [J]. Computer Engineering and Design, 2009, 16(2): 35 - 38.

[13] Chen Yang. Research of Digital Image Detection Algorithms by Using MATLAB [J]. Science & Technology Information, 2008, 25(8): 63 - 68.

[14] Zou Boxian, Lin Jingrang. Contour extraction research of image [J]. Computer Engineering and Applications, 2008, 21(4): 32 - 35.

自动计算热带气旋位置和范围的方法研究

刘永禄，邵利民，郎丰旺

（海军大连舰艇学院军事海洋系海洋气象教研室，大连 116018）

摘 要：本文以卫星云图的热带气旋云系为研究对象，基于 Canny 边缘检测、contour 轮廓提取等方法，研究了通过图像的形状特征和范围大小对热带气旋云系进行自动识别，得到了较好的效果。这种方法有助于提高热带气旋云系识别的自动化程度，实现热带气旋的自动跟踪，从而为热带气旋的预报提供了便利。

关键词：热带气旋；Canny 边缘检测；轮廓提取；自动识别

Ocean surface currents retrieval based on the satellite remote sensing data

AN Yu-zhu[1, 2], CHEN Yi-de[1], ZHANG Ren[1], WANG Hui-zan[1], CHEN Jian[1]

1. *PLA Key Laboratory of Military Marine Environment, Institute of Meteorology and Oceanography, PLA University of Science and Technology, Nanjing* 211101, *Jiangsu province, China*

2. 61741 *Troops of PLA, Beijing* 100081, *China*

Abstract: The ocean surface currents are reconstructed from the satellite remote sensing data containing altimeter-derived sea surface height and QuikSCAT satellite-derived wind data. Based on the method proposed by Lagerloef, a global weekly 0.5°×0.5° ocean surface current product was obtained over the period 2000 - 2008 by combining the geostrophic currents estimated from sea surface height with Ekman current estimated from the wind stress. Particularly, weight functions were introduced when calculating the Ekman currents to eliminate the discontinuity near 25°S and 25°N. These satellite-derived currents have been compared with TAO current meter and the SCUD product, respectively. The comparison showed that satellite-derived currents not only could capture the characteristics of ocean surface currents but also had high accuracy and reliability. The result showed that this innovatory method was effective.

Keywords: satellite altimeter data; QuikSCAT wind field; surface geostrophic current; Ekman current

1 Introduction

Ocean surface currents are important for studying air-sea interaction, heat transport and other oceanographic applications. High-resolution and accurate currents can improve our interpretations of the substance transportation, the pollutant diffusion and the rules of animal migration [1, 2]. So far, there have been many studies on calculating the surface currents in different ways. For example, Nililer et al. used 47 surface drifters in the Northeast Pacific during the fall of 1987 and 16 drifters in the fall and winter of 1989 and 1990 to investigate the correlation between current velocities at 15 m depth and the local wind speeds. He found out that the currents were highly coherent with the local wind with an average phase of 70° to the right of the rotating wind vector for the periods between 5

Received on Jul. 26, 2012

*Corresponding author: ayz_276521@sina.com

and 20 days [3]. Meurs et al. used the STORMS 87 and HEAVY 89 experimental data to investigate the differences in the large scale surface velocity and eddy activity in the northeast Pacific. The variability of mesoscale eddies can result in large interannual differences in estimating the mean velocity [4]. Ralph et al. analyzed the mean ageostrophic near-surface circulation measured by 1503 Lagrangian drifters at 15 m depth in the tropical Pacific between 1987 and 1994. It found the physical model of the wind-driven currents in a weakly stratified upper layer [5]. Based on the Kalman Filter trajectory prediction model, Guo et al. estimated the surface currents from November 2001 to October 2004 with error estimations. Moreover, this method was applied to obtain mid-depth currents at 1 000 db and 2000 db [6]. Hu et al. studied the multi-year averaged surface current field and seasonal variability in the Kuroshio and adjacent regions from 323 Argos drifters deployed by Chinese institutions and World Ocean Circulation Experiment [7]. Along with the rapid development of satellite remote-sensing observations, the currents derived from remote-sensing data are attracting more attentions. Lagerloef et al. assumed that geostrophic and Ekman components accounting for the lower-order dynamics of surface velocity could be obtained independently from surface height and wind stress data. He proposed a statistical model where geostrophy varied smoothly from a β plane formulation at the equator to an f plane formulation in the midlatitude and the two-parameter Ekman model [8]. Sudre et al. compared a global 1/4° resolution product of surface currents developed by the CTOH (Centre de Topographie des Océans et del' Hydrosphère) with other current products. Then a global validation was performed using Lagrangian surface drifting buoys and acoustic Doppler current profiler current observations. The results showed a very good agreement in the subtropical and mid-latitude bands. But a direct comparison with the TOGA/TAO moored current meter showed that only the low frequency currents were captured by the satellite current product due to the tropical instability waves [9]. Qiu et al. used TOPEX/POSEIDON altimeter data from April 1993 to March 2001 to study the seasonal variation of SLA and surface currents in the tropical Atlantic, and the results from TOPEX/POSEIDON were verified by those from the Argo drifting buoy trajectories [10]. Lin et al. investigated the seasonal and interannual variations of surface geostrophic currents in the Southeast Pacific using TOPEX/POSEIDON data [11]. Up to now, there is still no effective means to directly observe the currents in the global ocean. Retrieving the ocean surface currents based on satellite remote sensing data is a feasible approach.

Based on the altimeter and QuikSCAT data and the method developed by Lagerloef et al., the present work calculates the global ocean surface currents and improves the discontinuity when calculating the Ekman current in the latitudes of 25°S and 25°N. At last, this satellite-derived product is validated through comparing with other direct observations.

2 Data

2.1 Sea level height

Maps Sea Level Anomaly Merged (MSLA) data are provided by the AVISO (Archiving, Validation and Interpretation of Satellite Oceanographic data) web site (http://las.aviso.oceanobs.com/las/servlets/dataset). This product merges altimetric measurements from Topex/Poseidon, Jason-1, ERS1&2 and Envisat. The weekly data have a spatial resolution of 0.25° all around the globe. Comparing with the individual data source, the multi-resource altimetic data will possess much higher resolution. Note that the MSLA data range from 75°S to75°N over the period from 2000 to 2008. Then we convert this spatial resolution onto a 0.5° grid using linear interpolation algorithm. To eliminate the effects induced by tide, we only analyze the data deeper than 200 m. Additionally, the Mean Dynamic Topography (MDT) data which range from 82°S to 82°N provided by the Hawaii University are used to get the Absolute Dynamic Topography (ADT).

2.2 Wind stress

The wind stress is calculated by the QuikSCAT scatterometer with 0.5° resolution product from Jet Propulsion Laboratory (http://airsea-www.jpl.nasa.gov/data/QuikSCAT/wind/). This product ranges from 75°S to 75°N over the period from 2000 to 2008. In order to keep consistent temporal resolution with MSLA data, we convert the 12-hour resolution to the weekly one. Each Wednesday is assigned by the weekly mean value to cover this week.

2.3 TAO

Tropical Atmosphere Ocean (TAO, renamed the TAO/TRITON array on 1 January 2000) consists of about 70 moorings in the Tropical Pacific Ocean, telemetering oceanographic and meteorological data to shore in real-time via the Argos satellite system. They can measure the temperature, salinity and current in the upper ocean. The data are available from the TAO website (http://www.pmel.noaa.gov/tao/).

2.4 SCUD

SCUD (Surface currents from Diagnostic) model can be downloaded from APDRC/IPRC (Asia Pacific Data Research Center/International Pacific Research Center, http://www.apdrc.soest.hawaii.edu/). SCUD velocities are assumed to be related to the local instantaneous pressure gradient and wind by building a ten-coefficient model. Then the ten coefficients are calculated by minimizing the cost function for obtaining the current

fields [12]. The SCUD provides global daily current data with 0.25° resolution.

3 Methods

According to the viewpoint of Lagerloef et al., the surface currents are the sum of the geostrophic velocities and the Ekman currents at 15 m depth, i.e. $U=U_g+U_e=(u_g+u_e,v_g+v_e)$, where U are the surface currents, $U_g(u_g,v_g)$ is the geostrophic component, and $U_e(u_e,v_e)$ is the Ekman component.

3.1 Surface geostrophic currents

The geostrophic currents are calculated from the Aboslute Dynamic Topography (ADT) which is the sum of Maps Sea Level Anomaly (MSLA) and Mean Dynamic Topography (MDT), i.e. ADT=MSLA+MDT, where the ADT is the absolute dynamic topography relative to the geoid. Outside the equatorial band (5°S - 5°N), the geostrophic velocities are calculated based on the geostrophic balance equations. But inside the equatorial band, the geostrophic balance will not be suitable. So we adopt dual methods as follows:

Inside the equatorial band, the geostrophic velocities can be calculated by a β-plane approximation.

$$\begin{cases} u_\beta = -\dfrac{g}{\beta}\dfrac{\partial^2 h}{\partial y^2} \\ v_\beta = \dfrac{g}{\beta}\dfrac{\partial^2 h}{\partial x \partial y} \end{cases} \tag{1}$$

where $\beta \approx 2\Omega / r = 2.3\times10^{-11}$ / m · s (as a parameter in the equatorial band); g is the gravity acceleration; $f = 2\Omega\sin\varphi$; Ω denotes the earth rotational angular speed; φ is the latitude.

Outside the equatorial band, the geostrophic velocities can be calculated by a f-plane approximation.

$$\begin{cases} u_f = -\dfrac{g}{f}\dfrac{\partial h}{\partial y} \\ v_f = \dfrac{g}{f}\dfrac{\partial h}{\partial x} \end{cases} \tag{2}$$

The two equations estimate geostrophic velocities well in the corresponding region.

However, there are discontinuities in the transition belts. To ensure a smooth transition from the β-plane calculation in the equatorial band to the normal f-plane calculation elsewhere, weight functions are introduced within the equatorial band as follows to improve this limitation.

$$\mathbf{U}_g = W_f \mathbf{U}_f + W_\beta \mathbf{U}_\beta \tag{3}$$

$$\begin{cases} W_f = 1 - \exp\left[-\left(\dfrac{\phi}{\phi_s}\right)^2\right] \\ W_\beta = C \cdot \exp\left[-\left(\dfrac{\phi}{\phi_s}\right)^2\right] \end{cases} \tag{4}$$

where W_f and W_β are the weight funcions; W_f=0 and W_β =1 at the equator; $W_f \rightarrow 1$ and $W_\beta \rightarrow 0$ at 5°S and 5°N. φ_s is the latitudinal scale equal to 2.2°; C is the amplitude scaling equal to 0.7 which is tuned to provide a better fit to the equatorial current meter data.

3.2 Ekman current at the 15 m depth

Ekman currents are evoked by the wind stress which is calculated from the QuikSCAT data.

$$\boldsymbol{\tau} = [\tau_x, \tau_y] = \rho_a C_D V_{10} [u_{10}, v_{10}] \tag{5}$$

where ρ_a is the air density given by ρ_a=1.2 kg/m^3; V_{10} is the wind speed on the 10 m; u_{10} is the zonal wind speed; V_{10} is the meridional wind speed; and C_D is the drag coefficient [13, 14].

$$10^3 C_D = \begin{cases} 0.49 + 0.065 V_{10} & V_{10} > 10 \text{ m/s} \\ 1.14 & 3 \le V_{10} \le 10 \text{ m/s} \\ 0.62 + 1.56 V_{10}^{-1} & V_{10} < 3 \text{ m/s} \end{cases} \tag{6}$$

Lagerloef et al. proposed a two-parameter regression model between the Ekman currents at 15 m depth and the surface wind stress:

$$(u_e + i v_e) = B e^{i\theta} (\tau_x + i \tau_y)$$

$$\begin{cases} B = \dfrac{1}{\rho \sqrt{r^2 + f^2 h_{md}^2}} \\ \theta = \arctan\left(\dfrac{f h_{md}}{r}\right) \end{cases} \tag{7}$$

where ρ is the seawater density given by $\rho=1.02\times10^3$ kg/m^3; r is the frictional parameter equal to 2.15×10^{-4} m/s; h_{md} is the mixed layer depth (h_{md}=32.5 m).

Within the band between 25°S and 25°N, B and θ are constants. The amplitude B is ~0.3 / (ms · Pa). θ is the turning angle relative to the wind direction: 55° to the right (left) of the wind in the northern (southern) hemisphere at 15 m depth.

3.3 Improvement of the algorithm

In the two-parameter regression model, B and θ are important. Fig. 1 shows B and θ vary with the latitudes. B decreases gradually from the equator toward the mid-latitude and its value reaches 0.49 / (ms · Pa) at the 25°S and 25°N. The turning angle is 0° at the equator and increases with latitudes. At 25°S and 25°N, the angle can reach 83.87°. It is obviously that B and θ are not always constants for 0.3 / (ms · Pa) and 55°, respectively. As Fig. 1c and 1d show, these leaps will result in the singularities for u_e and v_e near the 25°S and 25°N.

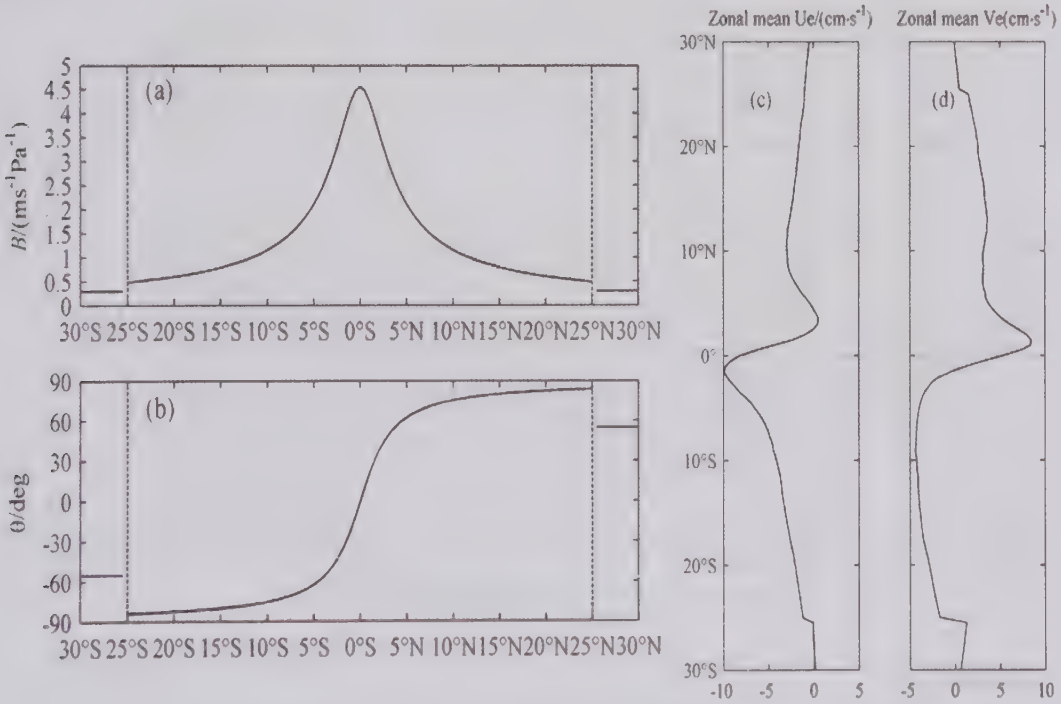

Fig. 1 Amplitude function B(a), velocity vector angle θ(b) to the wind stress vector, zonal averages of u_e (c) and v_e (d) between 30°S and 30°N

In order to resolve these discontinuities, we introduce weight functions (8) just like equation (4). B and θ are defined as equation (7) inside the band between 10°S and 10°N. In the bands 10°→25°S and 10°→25°N, the weight functions are calculated as follows.

$$\begin{cases} \mathbf{U}_{e10} = Be^{i\theta}(\tau_x + i\tau_y) & \begin{cases} B = \dfrac{1}{\rho\sqrt{r^2 + f^2 h_{md}^2}} \\ \theta = \arctan(\dfrac{fh_{md}}{r}) \end{cases} & |\phi| < 10° \\ \mathbf{U}_{e25} = Be^{i\theta}(\tau_x + i\tau_y) & \begin{cases} B = 0.3\ \mathrm{ms^{-1}Pa^{-1}} \\ \theta = 55 \times \pi / 180 \end{cases} & 25° \le |\phi| < 75° \\ \mathbf{U}_e = F_{10}\mathbf{U}_{e10} + F_{25}\mathbf{U}_{e25} & \begin{cases} F_{10} = \exp\left[-\left(\dfrac{|\phi| - 10}{6.6}\right)^2\right] \\ F_{25} = 1 - \exp\left[-\left(\dfrac{|\phi| - 10}{6.6}\right)^2\right] \end{cases} & 10° < |\phi| < 25° \end{cases} \tag{8}$$

where φ is the latitude (positive northward); U_{e10} and U_{e25} are the Ekman velocities at 10°S and 10°N and at 25°S and 25°N, respectively; $F_{10} \to 1$, $F_{25} \to 0$ at 10°S or 10°N; $F_{10} \to 0$, $F_{25} \to 1$ at 25°S or 25°N (Fig. 2).

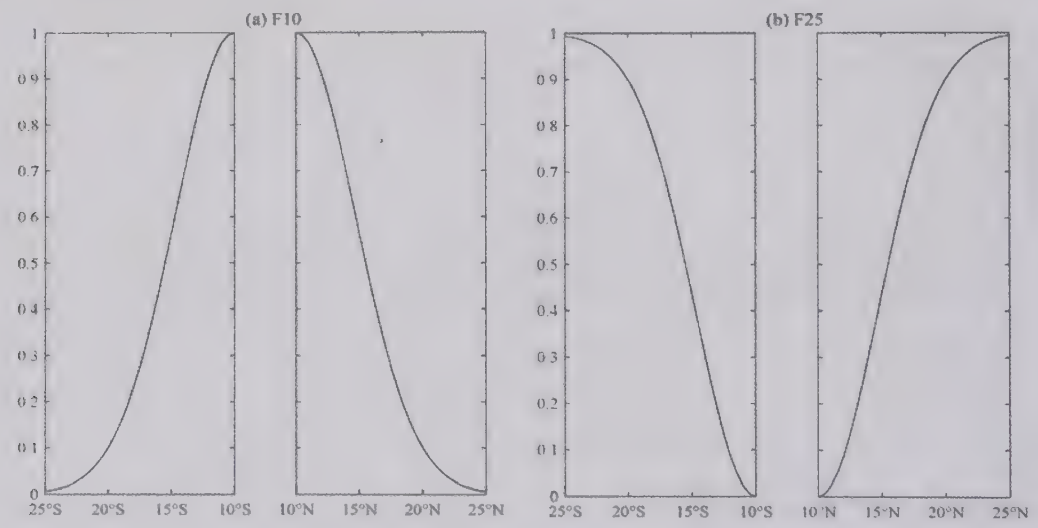

Fig. 2 Weight functions F_{10} (a) and F_{25} (b)

4 Validation

In this section, the global surface currents are calculated and validated for the years from 2000 to 2008. Fig. 3 shows the 9-year mean currents of Pacific and Atlantic. North Equatorial Current (EC) is near 10~20°N and bifurcates into two branches when reaching the western boundary. The northern branch is Kuroshio and the southern one is Mindanao Current. South Equatorial Current (SEC) strides the equator to 4°N and North Equatorial Countercurrent is near 6°N. In the Atlantic, the Gulf Stream and Equatorial Currents are also

significant. The Antarctic Circumpolar Current (ACC) spans 50°S from west to east. The retrieval currents can catch the large scale signals very well.

Fig. 4 shows the global standard deviation of the surface currents. The weak variations mostly locate in the open ocean. The standard deviations in the Southern Pacific Ocean and southern Atlantic Ocean are less than 10 cm/s but become sharp near the western boundary reaching 40 - 50 cm/s. At the equator, the standard deviations are more than 40 cm/s, which indicates that the equatorial currents are active. For example, the ITCZ (Intertropical Convergence Zone) shifts northward or southward with seasons. The vigorous region in the India Ocean is Somali where the standard deviation can exceed 70 - 80 cm/s because the Somali current shifts with monsoons [15]. ACC is the significant region in the southern oceans. In general, the variations are intenser in the northern oceans than that in southern hemisphere, and intenser in strong current regions than that in weak currents regions.

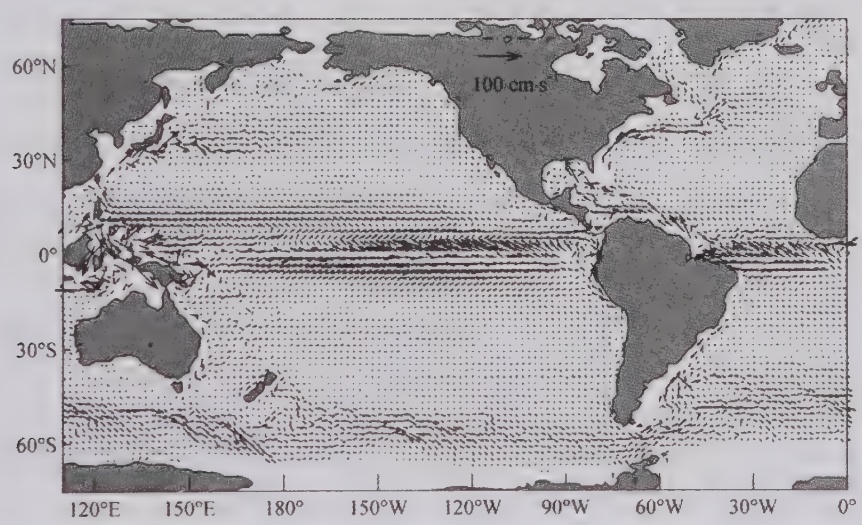

Fig. 3 Mean surface currents retrieved by satellite remote sensing data of Pacific and Atlantic over the period 2000 – 2008

4.1 Comparison with TAO

In this section, the moored current meter records from the TOGA/TAO array in the equatorial Pacific Ocean are compared with the retrieval current. TAO observations are necessarily interpolated to the time and location of satellite product.

We select three positions (0°N, 140°W), (2°N, 156°E) and (2°S, 156°E) to verify U and V. Note that the U and V have been scaled by the amplitude factor C in the aforementioned paragraphs. Tab.1 lists the correlation coefficients and the critical values

above the significance level of zonal and meridional velocities. The zonal correlation coefficients vary from 0.314 to 0.592, whereas the meridional correlation coefficients are lower (between 0.106 - 0.337). But the one in position 0n140w is under the significance level.

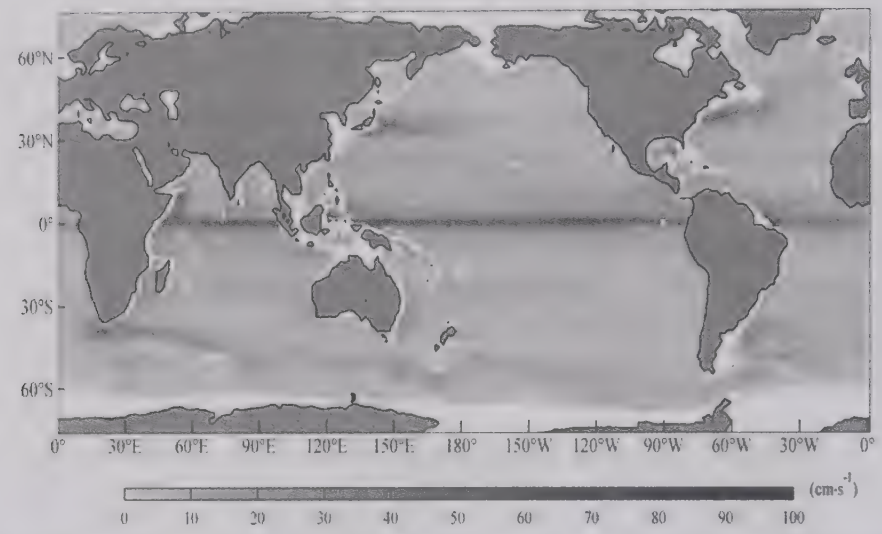

Fig. 4 Standard deviation of the global surface currents over the period 2000 – 2008

The satellite-derived currents are close to the TAO observations especially in the positions (2°N, 156°E) and (2°S, 156°E) where the correlation coefficients can reach 0.592 and 0.505, respectively. In the position (0°N, 140°W), the correlation coefficient reaches 0.32. They all pass the significance test. However, the meridional velocities (Fig. 5b, d and f) are dominated by high frequency signals. The correlation is stronger in the position (2°N, 156°E and 2°S, 156°E) than that in the position (0°N, 140°W). In this region, with the faster oceanic adjustment and rapid equatorial waves, the in situ currents change rapidly [9]. The statistics present that the satellite-derived product can reflect and catch the features factually.

Tab.1 Correlation coefficients and the critical values above the significance level of zonal and meridional velocities

position	zonal correlation coefficient	meridional correlation coefficient	critical value above the significance level
0n140w(0°N, 140°W)	0.314	0.106	0.117
2n156e(2°N, 156°E)	0.592	0.337	0.100
2s156e(2°S, 156°E)	0.505	0.213	0.105

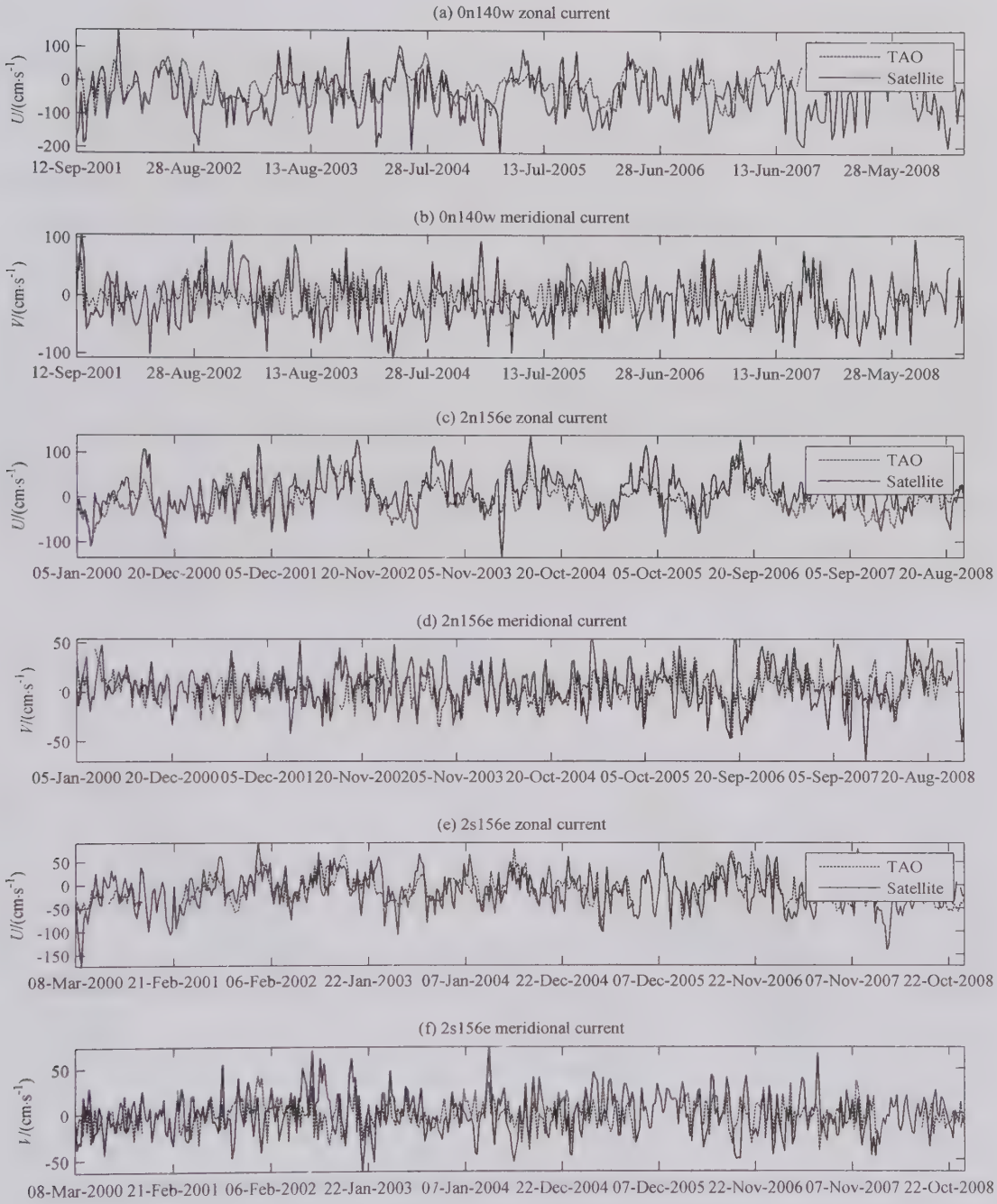

Fig. 5 Comparison between satellite retrieved currents (black solid line) and TAO observations(black dashed line).

(a) U and (b) V at 0°N, 140°W; (c) U and (d) V at 2°N, 156°E; (e) U and (f) V at 2°S,156°E; y-axis indicates speed and x-axis indicates time.

4.2 Comparison with SCUD

SCUD product is reproduced from trajectories of standard drifters and remote observations. In this section, we will compare the two current products in the tropical Pacific (30°S - 30°N, 122°E - 71°W). Firstly, the SCUD products are interpolated into 0.5°×0.5° grid. To quantify the differences between the two data sets, we have calculated the scatter plots of satellite retrieved currents versus SCUD currents in their zonal and meridional component, respectively (Fig. 6).

The analysis shows a higher zonal correlation (r=0.84) compared with the meridional correlation (r=0.62), which indicates that the satellite-derived currents consistent with the SCUD product very well in both components. However, the zonal mean differences (md=4.86) and the meridional one (md=1.02) are positive. That suggests our results are slightly larger than that of SCUD. The RMS difference of -0.88 for zonal component and 0.99 for meridional component denote that the zonal velocities are steadier, which have been illuminated in the TAO in-situ observations. The results show that the two datasets are highly consistent but the satellite-derived currents are little larger generally.

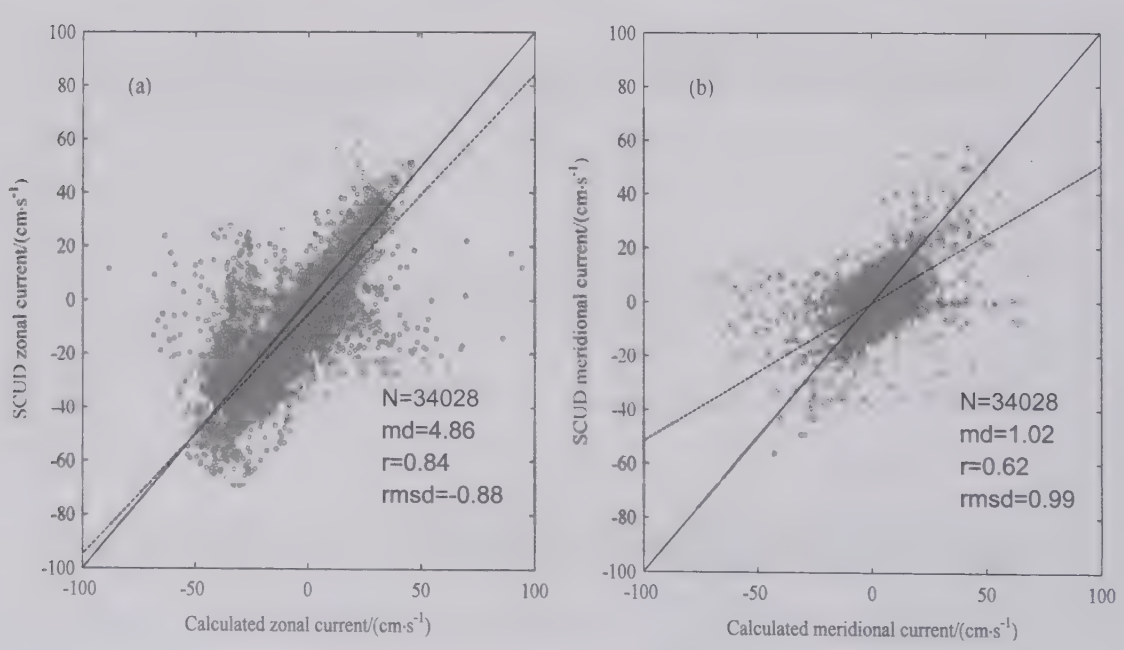

Fig. 6 Scatterplots of satellite retrieved currents versus SCUD currents

(a) zonal components; (b) meridional components

(black solid line denotes both are euqal; black dashed line denotes the linear regression;

N is the number of statistic points; md is the mean difference; r is the regression coefficient; rmsd is the RMS difference)

5 Conclusion

In this study, we discuss the discontinuity when calculating the Ekman flow near 25°S and 25°N, and apply weight functions to resolve the limitation. The satellite remote sensing data containing altimeter-derived sea surface height and QuikSCAT satellite-derived wind data from the years 2000 to 2008 are used to calculate the global ocean surface currents, then a global weekly 0.5°×0.5° ocean surface current product is reconstructed. Compared to the TAO current meter and the SCUD product, we find that this product can preferably reflect the characteristics of the sea surface currents in the large scale. The standard deviation indicates that the equatorial currents and the western boundary current system varies intensively, on the whole, the northern oceans vary more sharply than the southern oceans, and the strong flow areas vary more sharply than the weak areas. Satellite-derived currents not only can capture the characteristics of ocean surface currents but also have high accuracy and reliability. Thus, this innovatory method is effective.

Acknowledgements

This work was supported by the National Natural Science Foundation of China (No. 41306010, 41276088 and 41206002).

References

[1] Wahl T, Skøelv A, Pedersen J P, et al. Radar satellites: a new tool for pollution monitoring in coastal waters [J]. Coast Manag., 1996, 24: 61 - 71.

[2] Girard C, Sudre J, Benhamou S, et al. Homing in green turtles Chelonia mydas: oceanic currents act as a constraint rather than as an information source [J]. Mar. Ecol. Prog. Ser., 2006, 322: 281 - 289.

[3] Niiler P P, Paduan J D. Wind-Driven Motions in the Northeast Pacific as Measured by Lagrangian Drifters [J]. J. Phys. Oceanogr., 1995, 25: 2 819 - 2 830.

[4] Meurs P, Niiler P P. Temporal Variability of the Large-Scale Geostrophic Surface Velocity in the Northeast Pacific [J]. J. Phys. Oceanogr., 1997, 27: 2 288 - 2 297.

[5] Ralph E A, Niiler P P. Wind-Driven Currents in the Tropical Pacific [J]. J. Phys. Oceanogr., 1999, 29: 2 121 - 2 129.

[6] Guo Jige, Xie Jiping, Zhu Jiang. Estimation of the surface and mid-depth currents form Argo floats [G]. A collection of Argo research papers. Beijing: Ocean Press, 2006, 111 - 127.

[7] Hu Xiaomin, Xiong Xuejun, Qiao Fangli, et al. Surface current field and seasonal variability in the

Kuroshio andadjacent regions derived from satellite-tracked drifter data [J]. Acta Oceanologica Sinica, 2008, 30(6): 1 - 16.

[8] Lagerloef G S E, Mitchum G T, Lukas R B, et al. Tropical Pacific near-surface currents estimated from altimeter, wind and drifter data [J]. J. Geophys. Res., 1999, 104(C10): 22 313 - 23 326.

[9] Sudre J, Morrow R A. Global surface currents: a high-resolution product for investigating ocean dynamics [J]. Ocean Dynam., 2008, 58:101 - 118. DOI: 10.1007/s10236-008-0314-9.

[10] Qiu Yun, Hu Jianyu. Seasonal Variation of Surface Currents in the Tropical Atlantic Derived from Altimeter Data [J]. Marine Science Bulletin, 2005, 24(4): 8 - 16.

[11] Lin Liru, Hu Jianyu. Seasonal and interannual variations of sea surface geostrophic current in the Southeast Pacific [J]. Marine Sciences, 2006, 30(6): 51 - 58.

[12] Maximenko N, Hafner J. SCUD: Surface Currents from Diagnostic model [R]. IPRC Technical Note No. 5, 2010, February 16, 17p.

[13] Large W, Pond S. Sensible and Latent Heat Flux Measurements over the Ocean [J]. J. Phys. Oceanogr., 1982, 12(5): 464 - 482.

[14] Trenberth K, Large W, Olson J. The Effective Drag Coefficient for Evaluating Wind Stress over the Oceans [J]. J. Clim., 1989, 2(12): 1 507 - 1 516.

[15] Shi Maochong. Physical Oceanography [M]. Jinan: Shandong Education Press, 2004:137 - 139.

基于卫星遥感数据的全球表层流场反演重构

安玉柱[1,2]，陈奕德[1]，张 韧[1]，王辉赞[1]，陈 建[1]

（1 解放军理工大学气象海洋学院，军事海洋环境军队重点实验室，南京 211101；

2 解放军 61741 部队，北京 100081）

摘 要：利用 2000～2008 年的卫星高度计资料和 QuikSCAT 风场资料，反演了全球的海表的地转流和 Ekman 流，将两者合成后生成了 0.5°×0.5°的逐周全球表层流产品。在计算 Ekman 流的时候，引入了权重函数，改进了 Lagerloef 方法中 Ekman 流在 25°S 和 25°N 上的不连续问题。分析表明：卫星资料反演的流产品能够反映出海表流场的特征，将其分别于 TAO 观测和 SGUD 流产品进行定量化的比较显示，所得流产品具有较高的反演精度和可信度，说明改进的方法是有效的。

关键词：卫星高度计资料；QuikSCAT 风场；表层地转流；Ekman 流

Research of the wave measurement using GPS absolute velocity estimation technology

SHAN Rui[1, 2, 3], LIU Yan-xiong[4], ZHAO Tie-hu[1, 3], ZHANG Xiao-bo[1, 3], QIN Ke[1, 3]

1. Key Laboratory of Marine Hydrocarbon Resources and Environmental Geology, Ministry of Land and Resources, Qingdao 266071, Shandong province, China;

2. Key Laboratory of Surveying and Mapping Technology on Island and Reef, State Bureau of Surveying and Mapping, Qingdao 266590, Shandong province, China;

3. Qingdao Institute of Marine Geology, Qingdao 266071, Shandong province, China;

4. The First Institute of Oceanography, SOA, Qingdao 266061, Shandong province, China

Abstract: This paper analyzed the existing methods of wave measurement, and described the advantages of GPS applied in measuring the wave. The equations of absolute velocity estimation were discussed, focusing on two methods with Doppler shift. The error sources and their effect on velocity estimation were analyzed. Then, some tests were carried on to simulate dynamic velocity determination using static data. Based on the high-frequency carrier-phase derived Doppler observations, the velocity has been estimated to the precision of 1 cm/s or so, even to the mm/s level. And with the receiver generated Doppler measurements, the precision can reach 3 - 15 cm/s.

Keywords: GPS; absolute velocity estimation; Doppler observation; wave measurement; error analysis

1 Introduction

As an important movement phenomenon in the ocean, wave has a huge impact on human marine activities and coastal activities, thus, real-time monitoring of wave and studying its movement law became necessary. Therefore, the wave monitoring has been included in the marine operational observing. In recent decades, the increasing human activities on marine development greatly promote the ocean observing methods and equipment development [1]. GPS has the ability of precise positioning and velocity measurement. Because of its signal's large coverage and all weather working, GPS can be used in monitoring real-time ocean waves. Real-time three-dimensional instantaneous velocity of the carrier can be obtained by shipboard or buoy GPS Doppler measurements, which can inverse the real-time wave height, period, wave direction, and other physical

Received on Jan. 31, 2013

*Corresponding author: shanrui416@163.com

oceanographic parameters.

This paper first introduced the existing wave measurement methods, and then gave a systemic analysis on the existing methods of GPS velocity measurement [2-7]. On this basis, the models and methods of velocity measurement by Doppler original observations and export values had been discussed in detail, then error sources had been analyzed, and the achieved accuracy of different methods can be estimated by the solved results of sets of experimental data.

2 Current state of wave measurement technology

Visual method, optical wave meter, acceleration wave meter, hydraulic wave meter, acoustic wave meter and so on are the existing primary wave measurement techniques [1]. Visual method requires that the observers should have a wealth of background knowledge of waves and high visual ability, so the measured results are highly subjective, and this method is not applicable in an environment such as greater storms and other bad weather conditions. Strictly speaking, optical wave meter belongs to the visual method, so its result is still influenced greatly by the subjective role of the observer.

Acceleration wave meter measures waves by using the principle of acceleration. The major domestic instrument is SZF1-II digital temperature wave meter produced by Institute of Oceanography, Chinese Academy of Sciences. Its sampling interval is 0.25s or 0.5s, and wave height measurement accuracy can be up to 4 cm [1].

Acoustic wave meter measures the distance continuously between transmitter and sea by the propagation characteristics of ultrasound in the medium and the reflective properties of different media interfaces. Wave height, period and other wave elements can be calculated based on the real-time changes of the sea. According to different means of transmission, the instrument can be divided into the underwater type and above-water type. The measurement accuracy of above water-type is low because its transducer's position is not fixed. Underwater type is set in the seabed and fixed location because its transducer's position is fixed. But its measurement accuracy on small cycle waveform is not high, and the error is also big when the depth exceeds a certain range. Storm easily leads to a lot of foam, and bubble reflection of sound waves will cause the wrong instructions on the acoustic signal reception. At present, such kind of instrument includes ultrasonic wave height meter from Japan and American acoustic wave meter. Qingdao Institute of Iinstrumentation also has the same products [1].

Methods above can do the effective wave measurement, and its advantages and

disadvantages are also obvious. Visual and optical methods can not meet the requirements of the inclement weather and night observation, however the prices of gravity, acoustic, and hydraulic wave meter are generally more expensive, and can not get the position, wave height, period, wave direction and other physical oceanographic parameters. GPS has many advantages, such as all-weather, high precision, simple, cheap and so on. Through using GPS to measure the velocity precisely to inverse the basic information of waves, those shortcomings can be overcome.

3 GPS single point wave measurement

3.1 Principle of GPS single point velocity measurement

In the conventional terrestrial coordinate system, code pseudorange observation equation between station *i* and satellite j at a particular epoch *t* is as follow:

$$\tilde{\rho}_{\mathrm{i}}^{j}(t)=\rho_{\mathrm{i}}^{j}(t)+\mathrm{c}\delta t_{i}(t)-\mathrm{c}\delta t^{j}(t)+\Delta_{i,I_g}^{j}(t)+\Delta_{i,T}^{j}(t)+\varepsilon_{\rho} \tag{1}$$

Where $\tilde{\rho}_{\mathrm{i}}^{j}(t)$ and $\rho_{\mathrm{i}}^{j}(t)$ denote the code pseudorange and geometric distance between satellite *j* and receiver *i* at epoch *t*, respectively; $\delta t_{i}(t)$ and $\delta t^{j}(t)$ denote the receiver and satellite clock errors at epoch *t*, respectively; $\Delta_{i,I_g}^{j}(t)$ and $\Delta_{i,T}^{j}(t)$ denote ionosphere and troposphere delays, respectively; ε_{ρ} is the observation noise; the differential equation in (1) is as follow:

$$\dot{\tilde{\rho}}_{\mathrm{i}}^{j}(t)=\dot{\rho}_{\mathrm{i}}^{j}(t)+\mathrm{c}\dot{\delta t}_{i}(t)-\mathrm{c}\dot{\delta t}^{j}(t)+\dot{\Delta}_{i,I_g}^{j}(t)+\dot{\Delta}_{i,T}^{j}(t) \tag{2}$$

As a result, Doppler velocity measurement observation equation can be drawn as follows:

$$\lambda D_{\mathrm{i}}^{j}=\dot{\rho}_{\mathrm{i}}^{j}(t)+\mathrm{c}\dot{\delta t}_{i}(t)-\mathrm{c}\dot{\delta t}^{j}(t)+\dot{\Delta}_{i,I_g}^{j}(t)+\dot{\Delta}_{i,T}^{j}(t)+\varepsilon_{D} \tag{3}$$

$$\dot{\rho}_{\mathrm{i}}^{j}(t)=\begin{pmatrix} l_i^j(t) & m_i^j(t) & n_i^j(t) \end{pmatrix}\left[\begin{bmatrix} \dot{X}^j(t) \\ \dot{X}^j(t) \\ \dot{X}^j(t) \end{bmatrix}-\begin{bmatrix} \dot{X}_i(t) \\ \dot{X}_i(t) \\ \dot{X}_i(t) \end{bmatrix}\right] \tag{4}$$

where each parameter in equations (3) and (4) with "." denotes the temporal variability of corresponding variables; $\begin{pmatrix} l_i^j(t) & m_i^j(t) & n_i^j(t) \end{pmatrix}$ is the direction cosine between satellite j and

receiver *i* at epoch *t* in the conventional terrestrial coordinate system; ε_D is the observation noise.

The change rates of ionosphere and troposphere delays in equations (3) and (4) are too small to be neglected. The velocity and clock error variability of the satellite can be obtained by the navigation data. The receiver clock error variability can be solved in the equation solution as an unknown parameter. Before determining the direction cosine, three-dimensional position of the carrier and the satellite location should be pre-calculated. So before the determination of velocity, receiver position should be calculated by the pseudorange point positioning. As long as the number of observation satellites is four or more than four, the unknown above can be solved by the least squares principle.

Doppler value can be solved by the pseudorange or phase epoch difference. GPS receiver can record the original Doppler observed values and carrier phase observations. The accuracy of the carrier phase observations is much better than code phase observations [8], so the calculation of the export Doppler value in this paper used the phase observations corresponding to L1 carrier.

3.2 Waves information extraction

Evaluating the integrals of the calculated velocity component on the vertical direction will be able to get the wave surface displacement values at buoy, and a time series of wave fluctuating data could be obtained when trend and other low-frequency information were filtered through the sliding average method, wave height, period and other parameters would be obtained after the spectrum analysis on that time series. In order to get better information of the wave's changes under the severe sea state, the sampling rate of GPS receiver should be improved to get the high-frequency velocity information. In addition, the observed wave surface velocity data of the vertical, east-west and north-south direction by the GPS buoy can be used in the cross-correlation function of the Fourier transform to calculate the cross spectrum, coupled with the directional spectrum analysis, and wave directional spectrum could be obtained[9].

4 GPS single point wave measurement error analysis

4.1 GPS measurement-related error

The error source of GPS measurement is broadly divided into: the satellite-related errors, and receiver-related errors and other errors.

On the one hand, satellite orbit errors affect the positioning accuracy and thus indirectly affect the velocity measurement accuracy, and they have a direct impact on the solution accuracy of the station-satellite direction cosine. Assuming that distance between station and satellite was 20 000 km, the speed of the satellite was 3.2 km/s. If the satellite orbit error was 10 m, whose impact on the change rate of station-satellite distance would be 1.6 mm/s [10]. Currently the information released by IGS showed that the accuracy of GPS broadcast ephemeris was 1.6 m, the error which caused had very small impact on the velocity measurement. From the form of equation (4), it is clear that satellite velocity errors directly affect the change rate of station-satellite distance. When the satellite velocity error is less than 10 m/s, the velocity measurement error would be on the order of sub-millimeter per second. After SA policy was canceled, the accuracy of the satellite speed calculated by broadcast ephemeris was better than 1 mm/s [11].

The receiver position error and satellite orbit errors would all lead to the calculation error of the station-satellite direction cosine, and thus have an impact on the velocity measurement. The accuracy of the original Doppler observations is quite different due to different receiver types, and has varying degrees of delay [5]. Different documents had different views on its accuracy [4, 11]. In using export Doppler values to calculate the velocity, the precision of the phase observations would affect the final accuracy of velocity solution, meanwhile this method is susceptible to the influence of cycle slip.

In addition to the above error effects related to the satellite and receiver, the GPS measurement is also affected by the following errors, such as time change rate of the ionosphere and troposphere delay, relativistic effects, the multipath effects and observation noise, et al.

4.2 The impact on the GPS wave measurement in the marine environment

During the measurement at sea, except the above errors caused by GPS measurement, GPS wave measurement will also be subject to the impact of trends and the past boat, and these errors could be separated by selecting the appropriate high-pass and low-pass filter, because they had different frequencies.

Severe sea state usually leads large wind wave, and the buoy will also appear more substantial swing. If GPS was equipped on the measured wave buoy, the GPS receiver would loose sampling points occasionally when it was under water because GPS signals could not pass through the water, which resulted in data gaps and would affect the data quality of the GPS buoy wave measurement. In order to effectively control the quality of the data, the interpolation can be used in data repairing directly when the gaps appear less; follow-up normal sample values could be moved forward to ensure the data continuity

when data collection was interrupted for a longer period of time.

The receiver would not be under water in large waves when GPS receiver was equipped on small survey launches, but the hull itself would play a filtering role on the small trivial waves, and the collected data could not reflect the real waves, and motor equipment on board would bring the hull high-frequency jitter, which all would increase the noise of the data collection. So it is recommended to use the measured wave buoys as an equipped device platform.

5 Data testing and analysis

A number of tests were conducted to justify the achievable accuracies of GPS single point velocity measurement. If static observations were taken to calculate, the true value of the carrier speed should be zero, and the solution of the calculated speed value could be considered the true error of speed solver.

5.1 Static test

Trial data were collected by station MATE and the self-designed station SELF1 over the same period, May 20, 2003, and both sampling intervals were 30 s. Receiver used in station MATE was TRIMBLE 4000SSI, and station SELF1 was LEICA GX1230. Fig. 1 and Tab. 1 show the statistical results of 1000 epochs solver based on the original Doppler observations from two stations.

Tab. 1 Statistical results of errors with the method of single Doppler velocity estimation

	Station MATE				Station SELF1			
	Velocity component			Velocity	Velocity component			Velocity
	X	Y	Z	V	X	Y	Z	V
Mean error	-3.65	-0.85	-4.14	10.17	-0.10	4.92	-0.61	40.02
SD	7.00	4.00	6.82	5.79	18.89	33.62	27.70	26.01
RMS	7.89	4.08	7.97	11.71	18.89	33.96	27.70	47.72

SD:Standard Deviation; RMS: Root Mean Square

In Fig. 1, velocity measurement error of receiver LEICA GX1230 achieved the order of decimeter per second in some epochs, and error in most epochs was about 5 cm/s, while velocity measurement receiver precision of TRIMBLE 4000SSI, which was all controlled under 3 cm/s and more than half of epochs achieved the accuracy of sub-centimeter per second, was significantly better than the former. Tab. 1 shows the velocity error statistics in each direction component and the total value compared with the

true value, based on two stations' data solver. Accuracy differences between the two stations were obvious. As a result, the accuracy of the original Doppler measurement and receiver type with a greater impact on velocity measurement can be verified.

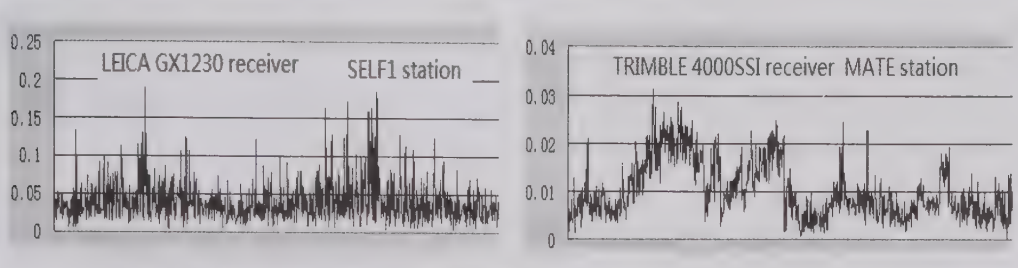

Fig. 1 Difference of velocities calculated with two types of receivers

In order to fully verify the accuracy of velocity measurement by the export Doppler value, two groups of high-frequency observational data were collected in May 30, 2008. Sampling intervals were 0.5 s and 0.1 s, and at the same time, recording the original Doppler observations. Observation length was 1 000 s and receiver model was Z-MAX. Two groups of observational data were solved by the means of export Doppler value solver and original Doppler observations solver respectively.

Data of 0.5 s intervals were tested firstly; Fig. 2 shows the true error of the velocity solved by two kinds of different ways in the X, Y and Z directions. It is clear that the results solved by export Doppler observations are better than those solved by the original Doppler observations in the three directions. Tab. 2 shows the statistical analysis on the velocity measurement results , although the mean error of the original Doppler value solver results was slightly better in the three directions, and the standard deviation and RMS of the export Doppler value solver internal accuracy was much better than the original Doppler value solver results. Mean error of Total velocity error showed that solver accuracy of data of 0.5 s intervals collected by the Z-MAX receiver using the export Doppler value measurement was up to 3 cm/s - 4 cm/s, and the solver accuracy of the original Doppler value was 13 cm/s - 14 cm / s.

Tab. 2 Statistical results of errors

0.5 s Interval	Using export Doppler values				Using original Doppler values			
	Velocity component			Velocity	Velocity component			Velocity
	X	Y	Z	V	X	Y	Z	V
Mean Error	1.33	-2.78	-1.65	3.53	-0.62	0.19	-0.29	13.97
SD	0.34	0.39	0.34	0.40	8.95	10.03	8.14	7.22
RMS	1.37	2.81	1.69	3.55	8.97	10.03	8.14	15.72

The same calculation was used to test the observational data of 0.1 s. Statistical results are seen in Fig. 3 and Tab. 3. The results solved by the export Doppler observations were still better than the original Doppler observation computed results in the three directions. The accuracy of velocity measurement computed by export Doppler values increased with the sample rate becoming larger. Velocity measurement accuracy of 0.1 s interval data collected by Z-MAX receiver , computed by export Doppler values, was 1~2 cm/s and doubled than 0.5s interval data solver results' accuracy.

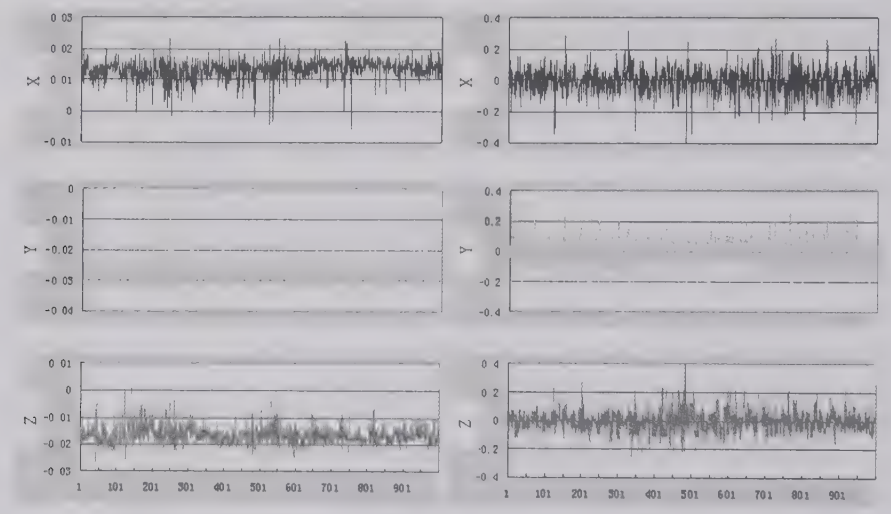

Fig. 2 Calculation results using observational data of 0.5 s

(a) Computed results using export Doppler value m/s; (b) Computed results using original Doppler value m/s

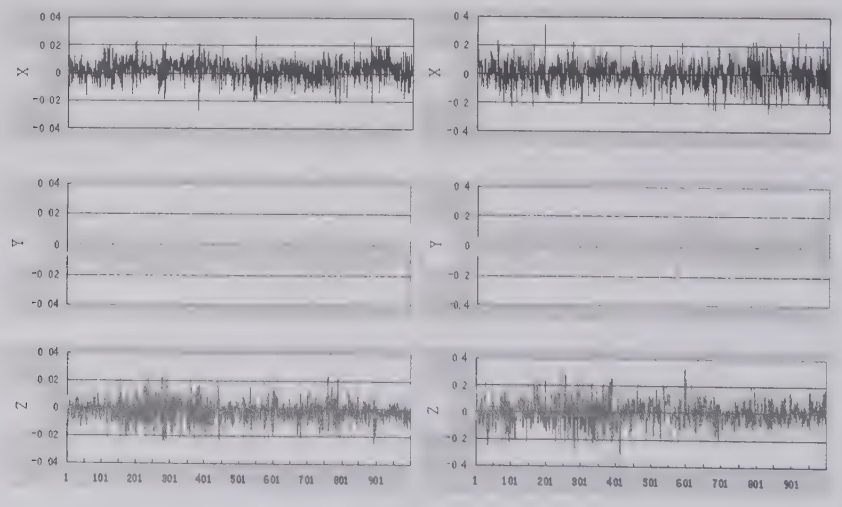

Fig. 3 Calculation results using observational data of 0.1s

(a) Computed results using export Doppler value m/s; (b) Computed results using original Doppler value m/s

Tab. 3 Statistical results of errors

0.1 s Interval	Using export Doppler values				Using original Doppler values			
	Velocity component			Velocity	Velocity component			Velocity
	X	Y	Z	V	X	Y	Z	V
Mean Error	0.24	-0.50	-0.24	1.47	0.18	0.58	0.48	16.52
SD	0.77	0.96	0.90	0.72	9.18	11.55	10.62	7.61
RMS	0.80	1.08	0.93	1.64	9.18	11.56	10.62	18.19

5.2 Kinematic Test

The Kinematic test area was in the Qingdao coastal waters, using two Leica SR530 dual-frequency GPS receivers and RTK measurement mode to record 23353 epochs' data (about 6.5 h) by 1s sampling rate. Rover station was set close to the tracking ship's center of gravity. The export Doppler velocity measurement and position differential RTK were taken to compute the speed. The changes of measured three-dimensional velocity component are shown in Fig. 4.

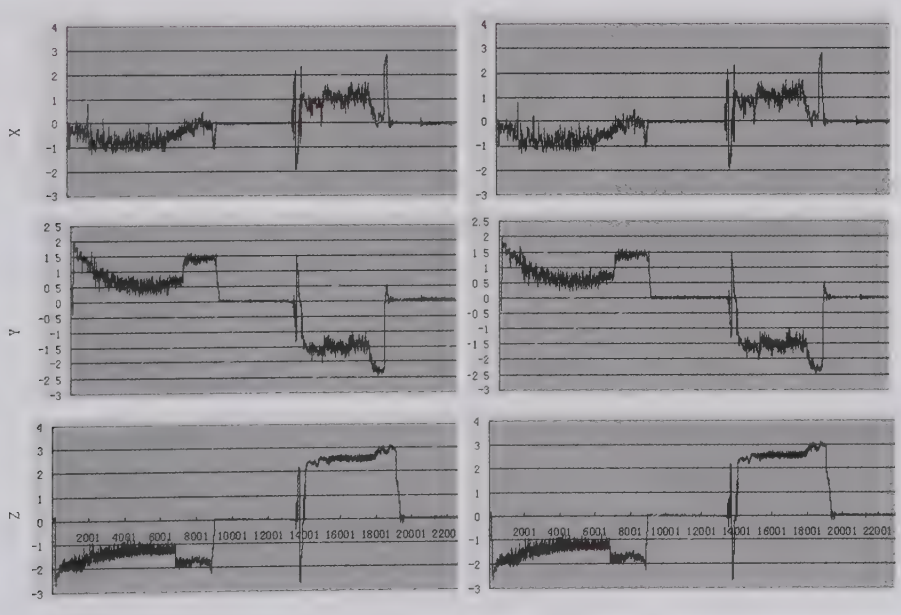

Fig. 4 Test results of calculating kinematic velocities

In Fig. 4, the real-time changes of the two ways to measure velocity showed a high degree of consistency. RTK had a real-time centimeter-level positioning accuracy, so velocity with high precision could be computed by its differential location information.

Calculating the difference of each epoch's computed speed in these two methods and making statistical analysis to verify the accord accuracy of the two methods, and the accuracy of two methods achieved the centimeters per second. All results are listed in Tab. 4.

Tab. 4 Statistics of Kinematic Test

Statistics	Speed difference of two methods' computed values in all directions		
	X	Y	Z
Mean Difference Value	-0.51	0.39	0.00
Standard Deviation	1.71	3.01	2.52
RMS	1.78	3.03	2.52

6 Conclusion

The computed results of static data in this article showed that the accuracy of single point velocity measurement using the original Doppler observations was 3 cm/s - 15 cm/s and obviously constrained by the receiver type. It's hard to get the high accuracy velocity measurement results when the low-performance receiver was used, because the collected Doppler observations had low precision and some of receivers couldn't record with Doppler data. When the export Doppler value was used, users can measure velocity only using single point observations of single-frequency receivers. As long as the data sampling rate is high enough, the velocity measurement precision could reach a higher level of about 1 cm/s - 2 cm/s. The kinematic test results showed that the export Doppler value and position differential RTK velocity measurement both achieved a good consistency and higher accord accuracy. The GPS technology obtain a carrier of high-precision velocity information, combined with GPS single-point velocity measurement techniques, and the GPS receiver is equipped on small tracking ship or buoy, extracting the sea surface displacement data through continuous observation and collection of speed data calculated by the integral filter, and further relevant wave information can be obtained through the direction of wave spectrum calculation. This method does not need other sensors, and there are some advantages such as simple system integration, low cost, small size, free from restrictions of the base station, so it has broad application prospects in the marine engineering, marine scientific research, disaster prevention and mitigation, marine navigation safety, marine surveying, airborne remote sensing, kinematic climate and meteorology research and application, and environmental protection.

In addition, pseudo-range point positioning was used in computing the carrier position, and the broadcast ephemeris was used in solving the satellite position. In order to achieve hopeful higher measurement precision, the precise ephemeris and locating the

precise point position based on the phase observations should be taken into account in the follow-up. Early exploratory studies in regard to the GPS single-point velocity measurement applied to the wave measurement had been done in this paper, and more comprehensive study of how to specifically measure in the marine environment should be finished in the latter part, and a complete operational observing system would be formed eventually.

Acknowledgements

This work was supported by the Key Laboratory of Marine Hydrocarbon Resources and Environmental Geology (MRE201233); Key Laboratory of Surveying and Mapping Technology on Island and Reef; State Bureau of Surveying and Mapping (2012B04).

References

[1] SHI Maochong, GAO Guoping, BAO Xianwen. Marine survey methodology [M]. Qingdao: Ocean University of China Press, 2000.

[2] HE Haibo, YANG Yuanxi, SUN Zhongmiao, et al. Mathematic Model and Error Analyses for Velocity Determination Using GPS Doppler Measurements [J]. Journal of the Plainstitute of Surveying and Mapping, 2003, 20(2):79 - 82.

[3] XIAO Yun, XIA Zheren. Comparison between Phase-Rate and Doppler to Determine Velocity [J]. Geomatics and Information Science of Wuhan University, 2003, 28 (5): 581 - 584.

[4] XIAO Yun, SUN Zhongmiao, CHENG Guangyi. Precise Determination of Velocity for Airborne Gravimetry Using the GPS Doppler Observations [J] .Journal of Wuhan Technical University of Surveying and Mapping, 2000, 25(2): 113 - 117.

[5] Hebert C J, Keith J. DGPS Kinematic CarrierPhase Signal Simulation Analysis for Precise Aircraft Velocity Determination [C]. ION Annual Meeting, Albuquerque, NM, 1997.

[6] Ryan S, Lachapelle G, Cannon M E. DGPS Kinematic Carrier Phase Signal Simulation Analysis in the Velocity Domain [C]. ION, Kansas, 1997.

[7] HE Haibo, YANG Yuanxi, SUN Zhongmiao. A Comparison of Several Approaches for Velocity Determination with GPS [J]. Acta Geodaetica et Cartographic Sinica, 2002, 31(3): 217 - 221.

[8] ZHOU Zhongmo, YI Jiejun. GPS satellite measurement Principles and Applications [M]. Beijing: Surveying and Mapping Press, 1997.

[9] WEN Shengchang, YU Zhouwen. Waves Theory and Calculation Principles [M]. Beijing: Science Press, 1984.

[10] IGS Central Bureau. IGS Products [OL]. http ://igscb.jpl.nasa.gov/ components/prods.Html, 2005.

[11] Serrano L, Kim D, Langley R B, et al. A GPS Velocity Sensor: How Accurate Can It Be? A First

Look [C]. ION NTM 2004, San Diego, 2004.

GPS 单点测速技术在海浪测量中的应用研究

单 瑞[1,2,3]，刘焱雄[4]，赵铁虎[1,3]，张晓波[1,3]，秦 轲[1,3]

（1. 国土资源部 海洋油气资源与环境地质重点实验室，山东 青岛 266071；
2. 海岛（礁）测绘技术国家测绘局重点实验室，山东 青岛 266590；3. 青岛海洋地质研究所，山东 青岛 266071；
4. 国家海洋局第一海洋研究所，山东 青岛 266061）

摘 要：分析比对了 GPS 单点测速技术与其他已有测波手段的不同，讨论了基于多普勒频移的 GPS 测速方法，并分析了各类误差对测速精度的影响。分别利用原始多普勒值和导出多普勒值进行了静态测速试验和动态测速试验，将导出多普勒测速结果与 RTK（Real Time Kinematic，实时动态测量系统）位置差分测速进行了比测。结果表明，使用静态数据采用高频导出多普勒值测速的精度可以达到亚厘米级每秒，而采用原始多普勒观测值进行测速因接收机型号的不同，结果差异较大；动态测速试验中，采用导出多普勒测速的方法与 RTK 位置差分测速的符合精度可达 cm/s。

关键词：GPS；单点测速；多普勒观测值；海浪测量；误差分析

A review of numerical modeling research on the marine oil spill

CAI Yang[1], MU Lin[2*], LI Huan[2], SONG Jun[2], CHI Yong-xiang[3], GUAN Cheng-yang[3], LI Cheng[3]

1. *Forecast center of South China Sea, Guangzhou* 510300, *Guangdong province, China;*
2. *National Marine Data and Information Service, Tianjin* 300171, *China*
3. *Ocean University of China, Qingdao* 266100, *Shandong province, China*

Abstract: Recently, as the oceanic activities are more and more frequently carried out, marine oil spill accidents bring to enormous harm to the economy and society in China, especially in the Offshore China. Marine oil spill is one kind of serious disasters which severely damages the marine environment. Aiming at the improvement of the emergency response system and response ability for the oil spill, the relative technologies on oil spill response are developed. This paper briefly introduces the developments and achievements of the oil spill numerical models, including the oil spill spreading model, the oil spill transport model, the oil particle model as well as the oil spill weathering model, which provide the theoretic criterions for the future work on the oil spill predicting and response.

Keywords: oil spill; spreading model; transport model; weathering model; oil particle model

1 Introduction

With the development of economy in China, the requirement of energy resources becomes more and more, which accelerates the development of marine transportation and petroleum exploration. However, the more human activities probably enlarge the risks of marine oil spill accidents, especially serious marine oil spill accidents. As a result, these marine oil spill accidents will damage the offshore marine environment, and affect people's life and hinder the economic development of China. Therefore, it is urgent to carry out the research on oil spill emergency response technologies, and improve the emergency response system as a technology platform which provides not only technical support for protecting the offshore marine environment safety but also provides necessary protection for the development of marine transportation and exploration industry of China.

Received on May 6, 2013

*Corresponding author: moulin1977@hotmail.com

In this paper, the fate and behavior prediction of marine oil spill and emergency response technology will be analyzed and discussed. Moreover, the development of oil spill numerical model will be described.

2 Oil spill numerical model

In a marine environment, the oil pollution will eventually disappear after a series of complicated physical, chemical and biological changes. The fate and behavior of oil can be divided into the processes as follows: (a) Spreading process: the enlargement of the oil slick on sea surface due to the intrinsic character of oil. (b) Transport process: the movement of the spilled oil, including horizontal transport as well as vertical mixing and suspension. (c) Weathering process: all of the processes that can lead to the composition property changes, including evaporation, dissolution, emulsification, dispersion, sedimentation, oxidation, biodegradation and so on [1]. Normally, evaporation and emulsification are closely related to the oil spill emergency response and economic damage assessment in a short term, but oxidation and biodegradation, which the final destination of the spilled oil depends on, are directly related to the marine environment impact assessment [2].

2.1 Oil spill spreading model

There have been many researches on the spreading process and the spreading range and rate of an oil slick have been paid more attentions. In the early stage, Blockker equation was ever proposed [3], which was based on the mass conservation of an oil slick with neglecting surface tension and viscosity, only considering specific gravity and volume of spilled oil. The equation is as follow:

$$D = [D_0^3 + \frac{24K_r}{\pi}(d_W - d_O)V_t]^{1/3} \quad (1)$$

where D_0 is the initial oil film diameter (m); d_0 is the oil specific gravity; d_W is the water specific gravity; K_r is the Blokker constant; V is the total oil volume. In addition, Okubo [4] developed his model, based on the analysis of great amount of observations and suggested that the approximate normal distribution of the oil slick mass was caused by spreading, and in the isotropic condition, the spreading range could be measured by the slick diameter on the premise when the oil slick periphery remained circle. But there exists a significant deficiency that in the slick spreading process, the diameter is only related to the spreading time.

It is well known that when oil is spilled, it starts to spread out over the sea surface, initially as a single slick. The speed at which this takes place depends upon the viscosity of

the oil to the great extent. Fluid, and low viscosity oils spread more quickly than those with high viscosity. Nevertheless, slicks quickly spread to cover extensive areas of the sea surface. Fay [5] developed the three-stage oil slick spreading model considering gravity, inertia, viscous and surface tension forces. The model could be divided into three equations according to the different roles of those forces at different stages: gravity-inertia spreading equation, gravity-viscous spreading equation and surface tension-viscous spreading equation. Based on an experienced research, simplified estimates of the spread of oil on water can be made by using as the follow equations:

$$\text{Gravity-inertial spreading equation: } D = 2k_1(g\beta V_t^2)^{1/4} \tag{2}$$

$$\text{Gravity-viscous spreading equation: } D = 2k_2(g\beta V^2/\sqrt{v_w})^{1/6}t^{1/4} \tag{3}$$

$$\text{Surface tension-viscous spreading equation: } D = 2k_3(\sigma/\rho_w\sqrt{v_w})^{1/2}t^{1/4} \tag{4}$$

$$\text{After the spreading, the diameter stays the same: } D = 356.8V^{3/8} \tag{5}$$

From equation (2) to equation (5), D is the diameter of an oil slick (m); g is the gravity acceleration (m/s^2); V is the volume of oil (m^3); t is the time (s); ρ_w is the density of sea water (Kg/m^3); $\beta = 1 - \rho_0/\rho_w$, where ρ_0 is the density of oil (kg/m^3); v_w is the viscous coefficient of water (m^2/s); σ is the surface tension coefficient difference among air-water interface, oil-air interface as well as oil-water interface (N/m); k_1, k_2 and k_3 are the experiential coefficients of the gravity-inertia spreading stage, gravity-viscous spreading stage and surface tension-viscous spreading stage, respectively.

After the proposition of Fay spreading model, several improvements on the model were made. Wang et al.[6] amended the second stage equation of the model, i.e. gravity-viscous spreading equation; Mackay [7, 8] considered the impact of the wind forces in the second stage and developed a new spreading model for both of thick and thin oil slick, combining with a large amount of observations; Lehr [9] suggested that oil slick should spread in the shape of oval. Therefore, he amended Fay spreading model by considering the effects of wind forces and currents on the asymmetric spreading of an oil slick.

It should be mentioned that a new Monte Carlo model had been developed for the study on the oil slick spreading process, which was based on the theory that under the effect of turbulence the diffusion of oil particles is random as a series of disordered movements. In Fig. 1, the directions of those particle movements at any time are random, and the randomness is controlled by the turbulence. Therefore, to any target particle, if the random number, the intensity of turbulence, the time range and the number of particles can be identified, the moving distance of the target particle can be calculated [10].

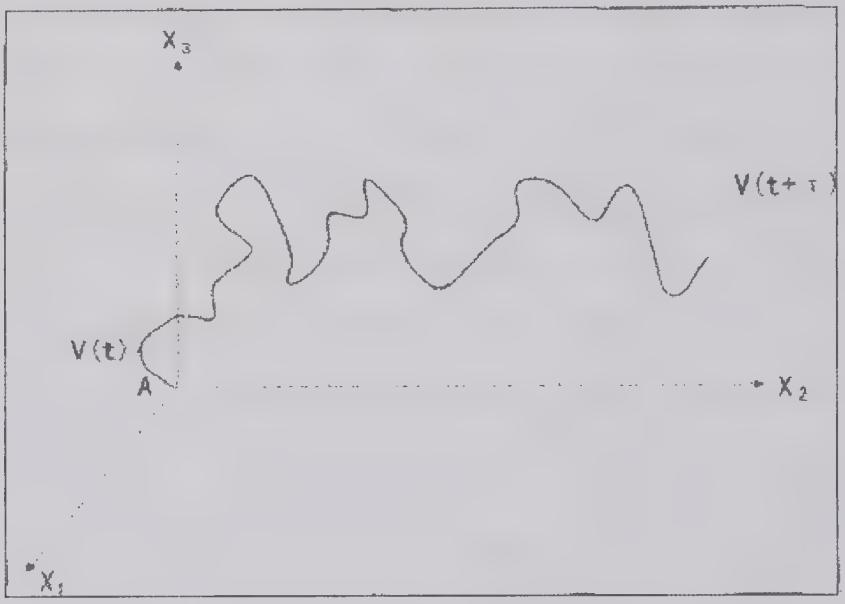

Fig. 1 Turbulent motion of solid fluid micro group

Actually, there are two ways to yield random numbers in Monte Carlo, namely, uniform random number and formal random number.

If a, b and c are random numbers between -0.5 and 0.5, then:

$$A=\frac{a}{\sqrt{a^2+b^2+c^2}},\ B=\frac{b}{\sqrt{a^2+b^2+c^2}},\ C=\frac{c}{\sqrt{a^2+b^2+c^2}} \tag{6}$$

The relation between discrete variance and diffusion coefficient is $k=\sigma^2/2\Delta t$. So the moving distances in three directions are:

$$l_x=A\bullet\sqrt{6\Delta t\bullet k_x},\quad l_y=B\bullet\sqrt{6\Delta t\bullet k_y},\ l_z=C\bullet\sqrt{6\Delta t\bullet k_z} \tag{7}$$

If a,b and c are normal random numbers between 0 and 1, the average of a,b and c is 0, and the normal distribution is (0,1), then the moving distances in three directions are as follows:

$$l_x=a\bullet\sqrt{6\Delta t\bullet k_x},\quad l_y=b\bullet\sqrt{6\Delta t\bullet k_y},\ l_z=c\bullet\sqrt{6\Delta t\bullet k_z} \tag{8}$$

What can be inferred from the equation (6) to (8) is that in Monte Carlo model, the diffusion of oil particles is random as a series of disordered movements under the effect of turbulence, and the transportation of particles is the simulation of Wiener process in mathematics.

Assuming sampling time interval $\Delta t > 0$, letting $X_n = X(n\Delta t)$ (9)

$$X_n = X_{n-1} + \sigma\sqrt{\Delta t}W_n \quad (\sigma > 0) \tag{10}$$

where $\{W_n\}$ is the independent random number of N (0,1)

Increasing $X_n - X_{n-1}$ only depends on k variables $(W_{n-k+1}.....W_n)$ responding to (n-k, n), so $X_n - X_{n-1}$ is distributed in N (0, 1).

As a result, transportation distance of the marked particle is expressed as the following:

$$X_i = X_{i-1} + U \bullet \Delta t + L \tag{11}$$

where $X = (x, y, z), U = (u, v, w), L = (l_x, l_y, l_z)$

Both of the horizontal velocity u and v contain the components driven by currents and wind; the vertical velocity w contains upward floating speed, sediment speed and marine dynamic vertical speed. The vertical diffusion items l_x, l_y and l_z are obtained from equations (7) or (8). The turbulent diffusion coefficient accords with three dimension current field. Thus the moving distance of any particle can be calculated from equation (11) and the behavior of spilled oil can be expressed by the locations of a large amount of oil particles.

In conclusion, the influences of marine environmental dynamic elements should be considered in the study of the oil slick spreading process. The spilled oil goes through gravitational spreading stage, in the early period after being spilled into the water when currents and wind forces have little effect on the slick spreading. With the weakening of gravitational spreading and the decrease of slick thickness, the oil slick steps into shear spreading stage, when the influence of currents and wind forces is dominant and the slick spreading is primarily driven by the viscous force between oil and air interface as well as oil and water interface, so the changes of currents and wind are important. Finally, with the weakening of shear spreading and the decrease of slick thickness, the oil slick steps into the transportation stage.

2.2 Oil spill transport model

The transport of the oil in a marine environment depends on a number of factors. After spreading to the maximum diameter, the oil slick translation in most near-shore waters will be dominated by wind and currents. The direction of the oil slick movement, which is influenced by wind, should be taken as that of the wind. Oil slick translation is

thus calculated as the vector sum of the currents and the wind stress on the slick. In addition to the translation of the surface slick, the possibility of the oil aging and mixing vertically with the water column should be considered. Normally, in the numerical model, the speed of the wind-driven component of the slick movement is considered to be about 3%~4% of the wind speed, and the speed of the current-driven component is the current speed. If the impact of coastal currents in the area where the oil spill happens is weak, the above calculation method will be suitable. In brief, it is necessary to access the current and wind data before calculating the transport track of oil slick.

The study on oil spill transportation numerical prediction started from 1960's. A wide variety of transportation models have been developed. Most of them combine the spreading and diffusion of the spilled oil. Some the representative models are shown as follows:

2.2.1 Coast Guard (II) model

Developed by Miller et al. [11], this model couples a wind-force model and a fluid dynamic model to predict the oil spill transportation. The wind-force model is built in the condition of the balance of wind stress, pressure gradient force and Coriolis force, where the wind stress friction near sea surface is also considered. The fluid dynamic model contains a two-dimensional discrete vertical average model of the pollutants. As the output from the wind-force model, the wind speed data is used by the fluid dynamic model to predict the transport tracks of oil slick [12]. This model mainly focuses on the dynamical effects of wind.

2.2.2 SEADOCK model

Developed by Williams et al. [13], this model calculates the displacement of the center of mass of the oil slick after the prediction of the transport of spilled oil under the control of wind and currents through the coordination of the weight coefficients of wind velocity vectors in the offshore sea, open sea, and then the superposition of the current velocity vector in sea surface. In the calculation of oil slick transport, considering that the entire slick is uniformly circularly distributed around the centroid, the spreading diameter calculated with Fay equations is adopted in the model at each step. In addition, a first-order decay caused by the evaporation and dissolution is also considered in the model, without the the influence of Coriolis force on wind and currents.

2.2.3 Navy model

Developed by Webb et al. [14], this model is mainly used to predict the transport of tanker and oil spill. In this model, the function of tidal flow, river, geostrophic flow and

wind-driven current role are considered and then the formulae of the displacement of the oil film centroid are established without the spreading of oil slick.

2.2.4 Other models

Huang L X [15] developed a diffusion model through the experiments by the synthesis of the vector of the current velocity, wind velocity and the slick spreading rate to obtain the drift velocity in different directions and the displacement at any point of the slick edge at any moment, which is the object of forecasting the trajectory of the slick. Wu Z. H. and Zhao W Q [16] developed an instantaneous oil spill model which considers the distribution around the centroid of slick similar to ellipse as well as long axis and the instantaneous drift in the same direction, and it obtains the slick centroid trajectory with the Euler-Lagrange method. In addition, it is possible to portray the irregular shape of the slick and the development process by calculating the trajectory of the edge of a particle in the transport.

2.3 Oil spill particle model

2.3.1 Definition of Lagrangian oil particle

As the pioneer, Johansen proposed a Lagrangian particle model, in which the oil slick was described as a combination of a number of discrete oil particles dispersed in water. And the concentration field is represented by a large number of "clouds" composed by many oil particles. Each particle is characterized by a certain amount of mass. These oil particels will drift and diffuse under the effect of currents. The translational motion of oil particles is simulated by Lagrangian approach. The simulation of shear flow and turbulence transport is achieved by random walking method, that is, the turbulence field is regarded as a random field and each particle acts like the Brownian motion of fluid molecules. So it is the random movement of each particle that results in the dispersion of oil "clouds" in the water [17, 18]. The particles accumulate as the oil slick on sea surface, where the oil particle is dispersed as oil droplets in water. The transport and weathering process of spilled oil is simulated by the interaction of superficial diffusion, advection, translation, emulsification and evaporation algorithm. The movement of the oil slick depends on the advection and turbulent diffusion around water bodies.

2.3.2 Lagrangian tracking of oil parcel

The Lagrangian tracking model can be used to describe the migration path of the oil slick. As the oil particles are elements of certain size certainmass, the trajectory and fate of spilled oil is simulated by combining the spreading, transport, turbulent diffusion, evaporation and dissolution processes at sea. In order to simulate the trajectory, each oil

particle which represents the portion of the oil slick is drifted and diffuse, which is driven by currents and wind [18].

Oil particle movements which could be divided into spreading, advection and diffusion process are simulated by means of Fay three-stage spreading equations, deterministic methods, and random walking method.

The Lagrangian tracking model is expressed as follows:

$$\frac{d\vec{r}}{dt} = \vec{V}(\vec{r},t) + \vec{V}'(\vec{r},t) \tag{12}$$

where $\vec{r} = x\vec{i} + y\vec{j}$ (m); $V(\vec{r},t)$ is the velocity (m/s); $V'(\vec{r},t)$ is the horizontal turbulent diffusion velocity of the oil slick (m/s); it is calculated with the following equation:

$$\vec{V}(\vec{r},t) = \alpha D\vec{W} + \beta\vec{U}w \tag{13}$$

where $\vec{W}$ is the wind speed at 10 m above sea surface; $\vec{U}_W$ is the sea surface flow velocity (m/s) calculated from two of three dimensional hydrodynamic equations; α is the wind factor, which is usually 3% - 4%; β is the effect factor accounting for drift of oil film on the surface, which is usually 1.1; D is the transition matrix of considering the wind deflection angle:

$$D = \begin{pmatrix} \cos\theta & \sin\theta \\ -\sin\theta & \cos\theta \end{pmatrix} \tag{14}$$

$\theta = 40° - 8\sqrt{\vec{W}}$ when $0 \le \vec{W} \le 25$ m/s; $\theta = 0$ when $\vec{W} \ge 25$ m/s.

The horizontal turbulent diffusion velocity is calculated with different formulae as follows:

$$\vec{V}'(\vec{r},t) = V' R_n e^{i\theta'} \tag{15}$$

where $V' = (4E_r/\delta t)^{1/2}$ (m/s), $E_r = 0.4 n_b V_R^{1/2} h^{5/6}$ is the rate of turbulent diffusion; h is the depth(m); δt is the time step(s); R_n is random number between 0 - 1; direction angle θ' is the random number uniformly distributed between 0 and π; there are different forms of the random walking method.

The position of the oil parcel is obtained from equation (12):

$$\begin{aligned} X &= X_0 + (V_x + V_x')\Delta t \\ Y &= Y_0 + (V_y + V_y')\Delta t \end{aligned} \tag{16}$$

where X_0, Y_0 are the initial coordinates of the particle.

The spreading stage adopts Fay three-stage spreading equations to calculate the spreading rate of the oil slick. According to substantive in-situ observations, Fay created the formula about oil area and volume when the spreading stage finishes, which is as follows:

$$A = 10^5 V^{3/4} \tag{17}$$

where V is the volume of spilled oil (m^3).

According to equation (17), when the spreading finishes, the oil slick thickness is $10^{-5}V^{1/4}$ m. Spreading, migration trajectory and an impact region of oil spill can be simulated with the tracking of the oil particle positions. The oil spill impact area generally refers to the sea area where the oil slick sweeps.

2.4 Oil spill weathering processes and models

2.4.1 Oil spill weathering processes

Oil spill weathering processes consist of the evaporation, dissolution, emulsification, dispersion, sedimentation, oxidation and biodegradation and so on.

Evaporation occurs when the lighter or more volatile substances within the oil mixture become vapors and leave the surface of the water. This process leaves behind the heavier components of the oil, which may undergo further weathering or may sink to the bottom of the ocean floor. Spills of lighter refined products, such as kerosene and gasoline, contain a high proportion of flammable components known as light ends. These may evaporate within a few hours, causing minimal harm to the marine environment. Heavier oils, vegetable oils, and animal fats leave the thicker, more viscous residue. These types of oils are less likely to evaporate.

Dissolution is the chemical stabilization of oil components in water. Water soluble compounds in the oil may dissolve into the surrounding water. This depends on the composition and state of the oil, and occurs most quickly when the oil is finely dispersed in the water column. Components that are most soluble in sea water are the light aromatic hydrocarbons compounds such as benzene and toluene. However, these compounds are also those first to be lost through evaporation. Oil contains only small amounts of these compounds making the dissolution one of the less important processes [19].

Emulsification is the term used for the formation of water in oil emulsions, which frequently results in the formation of mouse [20]. Emulsification is a physical process and is

formed when two liquids combine, with one ending up with being suspended in the other; this physical mixture is caused mainly by the turbulence at the sea surface. These emulsions significantly change the properties and characteristics of spilled oil [21]. There are two types of emulsions: water-in-oil or as otherwise called 'chocolate mousse'; and oil-in-water which is a lighter mixture [22]. The formation of the emulsions may occur during the first 8 hours after the spillage, but normally, the rate and extend of these processes depend upon the type of the oil involved and the sea state prevailing [23].

Dispersion is also a significant physical process associated with the destruction of an oil spill and begins almost as soon as the spill occurs [20]. Waves and turbulence at the sea surface can cause all or part of a slick to break up into the droplet the varying size, which becomes mixed into the upper layers of the water column [21]. The primary dispersions are unstable and separate easily by gravity alone, and in this case, the average droplet size is normally taken as being larger than about 50 μm. On the other hand, the secondary dispersions pose a severe separation problem since they are not separated by gravity, and the rates at which these very small droplets float to the surface are extremely low [24]. The increased surface area presented by dispersed oil can promote processes such as biodegradation, dissolution and sedimentation [22].

Sedimentation occurs as e result of a number of processes which increase the specific gravity of the oil above that of the supportive water [20]. The adhesion of small amounts of dense particles to the large surface area can cause sedimentation. Evaporation and dissolution of low molecular weight hydrocarbons bring about an increase in the oil specific gravity and enhance the sinking to the sediments where it will undergo a predominantly biodegradative process, provided that suitable dissolved oxygen and nutrient levels exist [20]. Most of the oil spilled will eventually enter the sediments and will degrade within them.

Oils react chemically with oxygen either breaking down into soluble products or forming persistent compounds called tars. This process is promoted by sunlight and the extent to which it occurs depends on the type of oil and the form in which it is exposed to sunlight. However, this process is very slow, even in strong sunlight, and thin films of oil break down at no more than 0.1% per day. The formation of tars is caused by the oxidation of thick layers of high viscosity oils or emulsions. This process forms an outer protective coating of heavy compounds that results in the increased persistence of the oil as a whole. Tarballs, which are often found on shorelines and have a solid outer crust surrounding a softer, less weathered interior, are the typical example of this process [19].

Sea water contains a range of micro-organisms or microbes that can partially or

completely degrade oil to water soluble compounds and eventually to carbon dioxide and water. Many types of microbe exist and each tends to degrade a particular group of compounds in crude oil. However, some compounds in oil are very resistant to attack and may not degrade. The main factors affecting the efficiency of biodegradation, are the levels of nutrients (nitrogen and phosphorus) in the water, the temperature and the level of oxygen. As biodegradation requires oxygen, this process can only take place at the oil-water interface since no oxygen is available within the oil itself. The creation of oil droplets, either by natural or chemical dispersion, increases the surface area of the oil and increases the area available for biodegradation to take place [19].

The processes of spreading, evaporation, dispersion, emulsification and dissolution are most important during the early stages of a spill whilst oxidation, sedimentation and biodegradation are more important later on and determine the ultimate fate of the oil.

2.4.2 Oil spill weathering models

At present, most of weathering models are developed to investigate the internal mechanism of weathering processes. Representative weathering models are IKU model, ADIOS model and Sebastiao&Guedes-Soares model.

(1) IKU model: IKU is developed by SINTEF (The Foundation for Scientific and Industrial Research at the Norwegian Institute of Technology). The inputs of model contain a number of experimental data and the environmental conditions, the former of which consist of the data about oil distillation curve, the maximum capacity of water absorption, the viscosity limits of the dispersant and so on. In addition, the outputs of the model contain the information of evaporation losses, the total oil mass balance, water content, the amount of dispersion, the time prediction of dispersant using and on-site incineration and so on.

The information of oil components comes from the distillation curve, where the evaporation process is analyzed with the quasi-component method as follows:

$$DQ_i(t)/dt = -\alpha(t)Q_i(t)M(t)P_i(t)/\rho(t)h(t)RT \tag{18}$$

where $Q_i(t)$ is the weight of component denoted i in the unit residual area (kg/m^2); $\alpha(t)$ is the mass transfer coefficient related to the wind speed (m/s); $M(t)$ is the molar mass of the liquid mixture (kg/kmol); $P_i(t)$ is the vapor pressure of component denoted i (N/m^2); $\rho(t)$ is the density of the liquid mixture (kg/m^3); $h(t)$ is the oil film thickness (m); R is the gas parameter (J/mol·K); T is the absolute temperature (K).

The dispersion process is calculated with the empirical equation proposed by Delvigne and Sweency [25]:

$$Q_r(d_0) = C(o)D_{ba}^{0.57} SFd_0^{0.7} \Delta d \tag{19}$$

where Q_r is the rate of oil droplets with the interval of Δd into water per the unit surface area (kg/m^2·s); $C(o)$ is the empirical entrance parameter relying on the oil category and the weathering state; D_{ba} is the energy of dispersive broken waves per the unit surface area (J/m^2); S is the rate of area covered by oil ($0 \le S \le 1$); F is the number of broken waves encountered on the sea surface in the unit time; d_0 is the diameter of the oil particle (m); Δd is the interval of the diameters of oil particles (m). Among them, the energy of dispersive broken waves is given by the semi-empirical equation:

$$D_{ba} = 0.0034\rho_w g H_{rms}^{\ 2} \tag{20}$$

where H_{rms} is the root of mean square of wave heights in the wave field; ρ_w is the density of sea water (kg/m^3); g is the gravitational acceleration (m/s^2).

In this model, the emulsion viscosity is calculated with the equation proposed by Mackay.

$$\mu = \mu_0 \exp[2.5w/(l - 0.654w)] \tag{21}$$

where μ, μ_0 are the viscosity of the weathered oil and initial oil, respectively (centipoise).

(2) ADIOS model: ADIOS developed by U.S. NOAA / HMRAD is a new weathering model, related to three oil properties (density, viscosity and water content) and four physical processes (spreading, evaporation, dispersion, emulsion).

In this model, the oil slick spreading process is simulated by the modified Fay spreading equations, and the evaporation process is described by Stiver and Mackay equation:

$$\frac{dF}{dt} = (K_E / h)\exp[6.3 - 10.2(C_1 - C_2 F)/T] \tag{22}$$

The dispersion process is described by the modified equation from Delvigne and Sweeney [25]. The water-in-oil rate of emulsion is calculated with the atomization equation proposed by Mackay:

$$dY/dt = kU^2(1 - Y/Y_f) \tag{23}$$

where Y is the volume ratio of water and emulsion; Y_f is the volume ratio of water and emulsion after emulsification finishes completely; the constant k is 0 for no emulsion, in

general, $k = 1.6 \times 10^{-6} s/m^2$.

The density is calculated from the assumption that the density and evaporation fraction as well as the change of temperature are linearly related, which is applied in the model by Mackay et al.:

$$\rho_m = Y\rho_w + (1-Y)\rho_0[1 - c_1(T - T_1)](1 + c_2 f) \tag{24}$$

Where ρ_m is the mixture density (kg/m^3); ρ_0 is the reference density (kg/m^3); T_0 is the reference temperature (K); f is the evaporation rate; c_1 and c_2 are experimental parameter based on the characteristic of spilled oil.

The viscosity is calculated with Mooney equation:

$$V_m = V_0 \exp(\frac{c_3 Y}{1 - c_4 Y}) \exp[c_5(\frac{1}{T} - \frac{1}{T_0})] \exp(c_6 f) \tag{25}$$

where $c_3 = 2.5$, $c_4 = 0.65$, $c_5 = 5.0$, c_6 is expressed by a curve.

(3) Sebastiao & Guedes-Soares model: in this model, the same equations as those in ADIOS are used to simulate oil spill evaporation, emulsification, viscosity changes and so on. In addition, the dispersion process is calculated with the equation proposed by Reed [26]:

$$D = 0.11(U + 1)^2 (1 + 50\mu^{1/2} \delta St)^{-1} \tag{26}$$

Where D is the hourly factor loss on the sea surface due to the dispersion; δ is the slick thickness (cm); St is the oil-water interfacial tension (dyne/cm); U is the wind speed (m/s); μ is the viscosity (centipoise).

The most successful improvement of the model is to simulate different weathering processes at the same time.

2.4.3 Summary

The defectsof the oil spill weathering model are as follows: a) Due to the lack of experimental data, most of the oil spill weathering models are based on the empirical equations. But actually, few empirical equations that affect the accuracy of the forecasts is on the basis of extensive research. Although, in some models, a few parameters are corrected by experimental data in order to enhance the simulation accuracy, most of parameters are not necessarily suitable to each type of oil due to the complexity in the weathering process of different oil. b) Weathering processes are so complicated that different processes have mutual influence and constraints, but it is difficult to integrate all of those processes since they are separated from each other in current models. c) There are both internal (eg. the composition change caused by the weathering of oil itself) and

external (eg. the geographical environment change, human intervention, et al.) factors which will influence the balance of the quality of spilled oil. However, independent calculations of the weathering processes in those traditional models seldom reflect the difference of the vertical distribution of oil due to internal reasons. Besides, it is a failure to find the actors of the geographical changes in the environment (such as near-shore stranding) and human interventions (such as various cleanup operations) which should be reflected in the mass balance prediction in most of the models to make them more practical.

To sum up, in order to make the weathering models more practical, it is suggested that the future development of the weathering models should depend on some substantive basic researches such as finding out the essential features and the microscopic mechanism of the oil weathering processes, and revealing the mechanism of the mutual influences of those processes.

3 Conclusions

This paper reviews the development of oil spill numerical model by introducing and analyzing oil spill spreading model, transport model, oil particle model and weathering model. Firstly, for the oil spill spreading model, the basis of calculating the spreading diameter is determined by analyzing and reckoning the changes of the spreading range and thickness under the influence of ocean dynamic factors. Secondly, for the oil spill transport model, the calculation method of the oil spill transport track is determined by analyzing the influence of currents and wind. Thirdly, for the oil spill particle model, the style of motion of the oil is analyzed on the ground of the concept of oil particle. Finally, for the oil spill weathering model, the internal mechanism of the weathering processes has been further analyzed. The paper provides the foundation and reference for developing the oil spill forecasting and operational warning system.

References

[1] Xu Yandong. A study on the weathering and predicting model of spilled oils at sea [M]. Qingdao: Ocean University of China, 2006.

[2] Yan Zhiyu. Study and Modeling of the Weathering of Spilled Oils at Sea [M]. Dalian: Dalian Maritime University. 2001.

[3] Blokker P C. Spreading and evaporation of petroleum products on water. Proc, 4th International Harbour Congress, Antwerp, the Netherlands, 1964, 911 - 919.

[4] Okubo A. Some Speculation on Oceanic Kiffusion Diagrams. In KuUenberg, G And Talbot, J.

Physical Processes Responsible for Dispersal of Pollutant in the Sea, Rapp. Proc. Verb Penn. Cons. Exp1. Mer, 1974(167): 77 - 85.

[5] Fay J A. Oil on the Sea [M]. New York: Plenum Press, 1969: 53 - 63.

[6] Wang H, Campbell J R, Ditmars J D. Computer Modeling of Oil Drift and Spreading in Delaware Bay [J]. Ocean Engineering, University of Delaware, 1975: 11 - 30.

[7] Mackay D, Paterson S, Trudel K. A mathematical model of oil spill behavior [R]. Canada: Environment Canada Report, 1980.

[8] Mackay D, Buist I, Mascarenhas R, et al. Oil spill processes and Models [R]. Canada: Environment Canada Report, 1980.

[9] Lehr W J, Cekirge H M, Fraga R J, et al. Empirical studies of the spreading of oil spills [J]. Oil and Petrochemical Pollution, 1984, 2(1): 7 - 11.

[10] Lou Angang, Wang Xuechang, Yu Yifa. Studies on Monte-Carlo Method Application for Predicting Marine Oil Spill Diffusion [J]. Marine Sciences, 2000, 24(5): 7 - 10.

[11] Miller and Stolzenback K D. A review and evaluation of basic techniques predicting the behavior of surface oil slicks [R]. MIT Report, 1977, 22: 20 - 30.

[12] Yang Hong, Hong Bo, Chen Sha. Research and Application Progress of Marine Oil-Spill Models [J]. Transactions of Oceanology and Limnology, 2007, 2: 157 - 163.

[13] Williams G N, Hann R W. Simulation Models for Oil Spill Transport and diffusion [C]. Summer Computer Simulation Conference, 1975: 748 - 752.

[14] Webb L, Taranto R, Hashimoto E. Operational Oil Spill Drift Forecasting [J]. In: proceedings of 7th Nary Symposium of Military Oceanography, Annapolis Maryland, 1970: 114 - 119.

[15] Huang Lixian, Zhang Guanxi, Wan Zhaozhong. Diffusion of Oil at Sea [J]. Chinese Journal of Environmental Engineering, 1982, 3(1): 7 - 12

[16] Wu Zhouhu, Zhao Wenqian. The Combined Oil Spill Model of Expansion, Dispersion and Migration [J]. Marine Environmental Science, 1992, 11(3): 35 - 42.

[17] Liu Weifeng, Sun Yinglan. Study and improvement of oil spill simulation methods. Journal of East China Normal University(Natural Science), 2009(3): 91-97.

[18] Wu Zhaochun. Numerical Simulation of Oil Spill Spread and Transport in the Tidal Waterways [M]. Shanghai: Shanghai University, 2009.

[19] International Tanker Owners of Pollution Federation Limited (ITOPF). Fate of marine oil spill. Technical information paper, 2002, 1 - 8.

[20] Robotham P W J, Gill R A. Input, behavior, and fates of petroleum Hydrocarbons. The Fate and Effects of Oil in Fresh Water [J]. London, Elsevier Science Publishers Ltd, 1989, 41 - 79.

[21] Oil in the sea III: Inputs, Fates, and Effects [M]. Washington, D.C: The National Academies Press, 2003.

[22] Global Marine Oil Pollution Information Gateway (GMOPIG). What happens to oil in the water? Technical Information Paper, 2007.

[23] Butt J A, Duckworth D E, Perry S G. Characterization of spilled oil sample: purpose, sampling, analysis and interpretation [J]. Journal of Chromatography A, 1986, (367): 1 - 453.

[24] Parker H D, Pitt G D. Pollution control instrumentation for oil and effluents [M]. London: Kluwer Academic Publishers Group, 1987.

[25] Delvigne G A L, Sweeney C E. Natural dispersion of oil [J]. Oil and Chemical Pollution, 1988, (4): 281 - 310.

[26] Reed M, Gundlach E A. Coastal zone oil spill model: development and sensitivity studies [J]. Oil and Chemical Pollution, 1989, (5): 411 - 449.

海上溢油数值模型研究进展

蔡 扬[1], 牟 林[2], 李 欢[2], 宋 军[2], 迟永祥[3], 管承扬[3], 李 程[3]

（1. 国家海洋局南海预报中心，广东 广州 510300；2. 国家海洋信息中心，天津 300171；
3. 中国海洋大学，山东 青岛 266100）

摘 要：我国是海洋大国，近年来，海上活动持续增多，发生海上溢油事故的风险随之加大，海上溢油污染事故一旦发生，如不得到及时控制，必将严重损害我国近海海洋环境。为了完善我国海上溢油应急反应体系，提高我国处理重大海上溢油事故的应急反应能力，海上溢油污染应急技术研究已经得到开展。本文综述了溢油预测模型的发展过程以及相关的研究成果，包括：溢油扩展模型、溢油漂移模型、油粒子模型和溢油风化模型等。这为进一步开展溢油预测和溢油污染应急工作提供了理论依据和参考。

关键字：海上溢油；扩展模型；输运模型；油粒子模型；风化模型

Distribution and ecological evaluation of heavy metals in multi-medium of the Dongzhai Harbor

TIAN Hai-tao[1], CAO Ling-long[1, 2*], WANG Ping[1], XIE Jian[1], HE Yuan-sheng[3]

1. *South China Sea Marine Engineering and Environment Institute, SOA, Guangzhou* 510300, *Guangdong province, China;*

2. *Department of Earth Sciences, Sun Yat-sen University, Guangzhou* 510275, *Guangdong province, China;*

3. *Haikou marine Environment Monitoring Center, SOA, Haikou* 570310, *Hainan province, China*

Abstract: The distribution characteristics of heavy metals such as Cu, Zn, Pb, Cd, Hg. As in seawater, superficail sediments and several marine organisms of Dongzhai Harbor in Hainan were analyzed. Index methods of the single factor and geo–accumulation were used to assess the pollution degree of heavy metals. The results showed that the heavy metal levels in the seawater of Dongzhai Harbor accorded with the first category of the seawater except Pb, and were much lower than the fishery water quality standard; the concentration of the heavy metal in surface sediments did not exceed the national benchmark of the first-class of marine sediment quality basically, and the superficial sediments were essentially uncontaminated; the heavy metal content in wetland sediments was slightly higher than those in other typical mangrove wetland island of Hainan and marine sediments in Dongzhai Haibor, which indicated this area might has been affected by land-based pollution influence, and this should cause the attention of related departments; the heavy metal concentrations in marine organisms were up to the first category. All were not beyond the standard of non-environmental pollution aquatic products.

Keywords: seawater; sediment; marine organisms; heavy metals; Dongzhai Harbor

Introduction

Most of heavy metals, after the adsorption, sedimentation and other physical-chemical processes, will transform into particulate, and finally precipitate in the inshore water [1]. In this water-sediment transformation system in which lots of physical, chemical and biochemical process are proceeding, specific chemical composition and variation in the sediments are important factors for evaluating environmental change [2]. In these

Received on Mar. 25, 2013

*Corresponding author: 444810453@qq.com

processes, heavy metals are biodegradated by benthic organism, then transferring, enriching in the organisms by food chain. Consequently it will result in the adverse reaction in the organisms, even harm demic health [3].

The mangrove ecosystem is one of the highest-productivity marine natural ecosystems, and meanwhile, it is the most endangered one [4]. In a broad sense, mangrove ecosystem doesn't only include mangrove, mud flat and gei wai fishponds, but also includes coastal waters, sediments and organisms. Mangrove becomes the source and collection area of heavy metals usually, as lying between outfall and coastal zone, belonging to the connection of ocean and land [5]. In the heavy metal study, there are lots of work about heavy metal distribution and evaluation in the mangrove ecosystem [6-9]. Most of them analyze the single factor, for example, soil, sediments, while few records the comprehensive survey of heavy metal factors, including water, sediments, organisms and so on.

So mangrove ecosystem attracts more and more environmental scientists' attention, meanwhile mangrove of Dongzhai Harbor in Hainan is an important mangrove ecosystem protection areas in our country. Just because of these, this study analyses typical heavy metal(Cu, Zn, Pb, Cd, Hg, As), in order to evaluate heavy metal pollution features and degree comprehensively, and further offer some theoretical significance and practical value for marine ecosystem protection and sustainable utilization of mangrove in Dongzhai Harbor.

1 Regional overview and research methods

1.1 Research area

Dongzhai Harbor in Haikou, with a tropical maritime climate, is a national mangrove wetland nature reserve, and has been included in the international directory of important wetlands. The average tidal range of irregular diurnal tidal in Dongzhai Harbor is approximately 1 meter. Annual average temperatures of Dongzhai Harbor and sea surface are about 23.8 °C and 24.5 °C respectively, while mean annual precipitation is 1 676 mm. The major species of mangrove are *Bruguiera gymnorrhiza, Avicennia marina, Kandelia candel, Aegiceras corniculatum* and so on, with an area of 1 700 hm^2 approximately. There are several natural villages around Dongzhai Harbor and a large area of mariculture zone outside the reserve.

1.2 Sampling and research methods

1.2.1 Monitoring stations and time

We set up 5 stations to investigate environmental quality of heavy metals in the seawater, superficial sediments and marine organisms of Dongzhai Harbor (neap season) in July, 2010, combining with previous survey data of wetland sediments in Dongzhai Harbor (2008). The distribution of these stations is shown in Fig. 1.

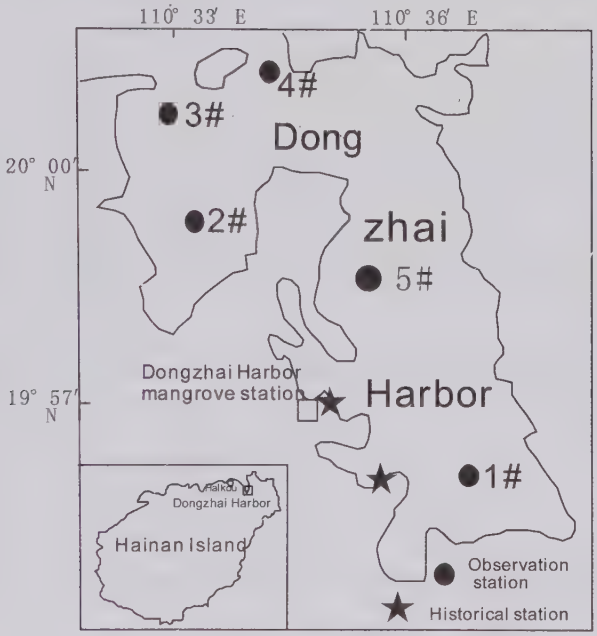

Fig. 1 Monitoring stations in the Dongzhai Harbor

1.2.2 Sample collection and analytical techniques

Surface seawater is collected in clean polyethylene bottles and 0.45 um Nuclepore membrane is used to filter on site. Bottom sampler is used to collect sediment samples into sample sacks, and then they are air-dried, uniformed and grinded in the lab for the following analysis. Collected marine organisms are washed by seawater, and then cryopreserved in polyethylene bottles. Zn, Cd, Cu, Pb in seawater are determined using graphite furnace atomic absorption spectrometry, while these elements in sediments and marine organisms are analyzed using flame atomic absorption spectrometry. As in seawater, sediments and marine organisms are determined using arsine spectrophometry and Hg by cold atomic absorption spectrometry respectively. Collection, analysis and measurement methods of all samples strictly referred to "The Marine Monitoring" [10].

2 Results and analyses

2.1 Concentration distribution of heavy metals and environmental quality assessment in the seawater

Results of heavy metal monitoring in the seawater are shown in Tab. 1 and Tab. 2. Concentration of some heavy metals in the seawater presents certain regular distribution, such as the concentrations of Hg, Zn, Pb, which gradually reduce from southern gulf to bay mouth. Combining with the trend of survey data, distribution of heavy metals may be related to hydrodynamic conditions and the impact of land-based pollution emissions, which is consistent with distribution of heavy metals in other harbors [11, 12]. By using single factor method to evaluate seawater quality standards [13], we reached the results that the heavy metals pollution levels in seawater in Dongzhai Harbor accord with the first category of the seawater except Pb, and much lower than the fishery water quality standard, which indicated that the seawater was suitable for the cultivation and production of fishing and marine function zoning.

Tab. 1 Results of heavy metal content in the seawater of the Dongzhai Bay

Porjects	c / μg / L					
	Cu	Zn	Pb	Cd	Hg	As
Average value (concentration range)	3.01 (2.64 - 3.40)	8.6 (8.0 - 9.0)	1.55 (1.32 - 1.74)	0.24 (0.22 - 0.27)	0.03 (0.01 - 0.05)	1.9 (1.6 - 2)
First category of the seawater	5	20	1	1	0.05	20
Second category of the seawater	10	50	5	5	0.2	30
Fishery water quality standard	10	100	50	5	0.5	50

Tab. 2 Evaluation results of heavy metals in the seawater of the Dongzhai Bay

Evaluation elements	Cu	Zn	Pb	Cd	Hg	As
Single pollution index (first category standard)	0.61	0.43	1.50	0.24	0.53	0.09
Evaluation results range (first category standard)	0.53 - 0.68	0.40 - 0.45	1.32 - 1.74	0.22 - 0.27	0.18 - 0.98	0.08 - 0.1

2.2 Content of the heavy metal in the superficial sediment and environmental quality evaluation

2.2.1 Content of heavy metal

Tab. 3 shows the content of heavy metal in the superficial sediment samples from Dongzhai Harbor, indicating that the content of heavy metal in sediments from mangrove and hidden shoal is higher than that in bottom sediments of Dongzhai Harbor (such as Cd, Cu, et al.). Comparing with the content of heavy metal in sediments from typical mangrove wetland in Hainan Island and surrounding area, we discovered that Dongzhai Harbor samples were at a bit higher level than medium. According to the first class sediment quality from marine sediment quality, evaluating by the single factor evaluation method, we could deduce the pollution level of heavy metal in superficial sediments of Dongzhai Harbor from high to low are, Zn, Pb, As, Cu, Cd, Hg in order. However, the pollution index of each heavy metal are all less than 1.0, meaning that they accord with the first class sediment quality and unqualified rates are 0%. These attribute to the lower development and less effect of human activity.

Tab. 3 Contents of heavy metals in the surface sediments

Project	w/×10^{-6}					
	Cu	Zn	Pb	Cd	Hg	As
This study	3.9	36.33	11.68	0.012	0.012	17.40
	2.2 - 6.1	22.6 - 50.6	8.1 - 15.4	0.001- 0.04	0.003 - 0.015	16.49 - 18.39
Mangrove and tidal flat [9]	17.9	57.3	19.1	0.11	0.08	12.9
Wenchang [13]	27	89	30	ND	0.06	15
Sanya Bay [9]	9.5	53.1	17.5	0.13	0.06	7.1
Yalong Bay [9]	4.7	25.7	14.7	0.12	0.03	5.2
Zhanjiang [13]	19	69	36	ND	0.04	16

Notes: Lithology of samples mainly are sludge and conglomerate-bearing sandy; ND indicates no results.

Tab. 4 Evaluation results of heavy metals in the surface sediments

Elements	Cu	Zn	Pb	Cd	Hg	As
The first class /×10^{-6} [12]	35	150	60	0.5	0.2	20
Factor of pollution index	0.11	0.24	0.19	0.024	0.06	0.87
Extent of evaluation results	0.06 - 0.17	0.15 - 0.34	0.14 - 0.26	0.01 - 0.08	0.02 - 0.08	0.82 - 0.92

2.2.2 Evaluation of heavy metal pollution

(a) Evaluation methods

We used index of geo-accumulation (I_{geo}) to evaluate heavy metal pollution, which was created by the German scientist Muller [14] as a quantitative index to research heavy metal pollution of sediments in the water environment. This method doesn't only consider geochemical background values and human element, but also, especially, pays attention to the change of background values, resulted by natural lithogenesis. Computational formula is as follows:

$$I_{geo}=\log_2^{[Cn/(1.5BEn)]}$$

In this formula, BEn is geochemical background values of heavy metals, mg/kg. Cn is the content of the element in sediments (a measured value, meaning mass ratio), mg/kg. Because of the change of background values by diagenesis, so we must have a constant (1.5). Index of geo-accumulation is divided to 7 grades, from 0 to 6 grade, indicating pollution from none to the extreme. Tab. 4 shows ecological-geochemistry survey of Hainan in the national second general survey of soil, which we used as background values [15]. We listed the relation between index of geo-accumulation (I_{geo}) and the pollution grades in Tab. 5 [16].

Tab. 4 Geo-chemical background values of heavy metals

Elements	Cu	Zn	Pb	Cd	Hg	As
BEn($\times10^{-6}$)	4.95	35.11	22.34	0.05	0.03	1.14

Tab. 5 Index of geo-accumulation(I_{geo})and the pollution grades

	pollution level						
Category	None	None - Medium	Medium	Medium - High	High	High - Extremely high	Extremely high
I_{geo}	<0	0 - 1	1 - 2	2 - 3	3 - 4	4 - 5	>5
I_{geo} level	0	1	2	3	4	5	6

(b) Results of evaluation

We selected 6 heavy metal elements (Cu, Zn, Pb, Cd, Hg, As,) to evaluate the pollution degrees in superficial sediments of Dongzhai Harbor. The results are showed in Tab. 6, indicating that, in general, index of geo-accumulation(I_{geo}) of Cu, Zn, Pb, Cd, Hg in 5 samples are low, however, that of As lies between 3 and 4, meaning a serious pollution.

Overall, index of geo-accumulation of heavy metal in mangrove wetland is a bit higher than that in bottom sediments of Dongzhai Harbor, consistent with the results of the single factor evaluation. Due to many villages lying around Dongzhai Harbor, agriculture is developed. So pollution source of heavy metal may derive from land, including sanitary wastewater and farmland drainage. Meanwhile, mangrove ecosystems, lying in intertidal zone, have features that they can absorb, deposit and settle down heavy metals. Consequencely, heavy metal content in hidden shoal is higher than that in water. High index of geo-accumulation (I_{geo}) of As possibly relates to releasing heavy metal from protective paint of shipping. By comparative study and combing with past studies, we suggested that mangrove region in tidal flat might become a heavy metal enrichment region [9, 11].

Tab. 6 Index of geo-accumulation (I_{geo}) and the pollution grades of sedimentary heavy metals in Dongzai Bay

Element	1#		2#		3#		4#		5#		wetland#	
	I_{geo}	I_{geo} class	I_{geo}	I_{geo} class	I_{geo}	I_{geo} class	I_{geo}	I_{geo} class	I_{geo}	I_{geo} class	I_{geo}	I_{geo} class
Cu	-0.63	0	-1.57	0	-1.75	0	-0.28	0	-1.64	0	1.27	1
Zn	-0.06	0	-1.22	0	-1.08	0	-0.16	0	-1.32	0	0.12	1
Pb	-1.27	0	-2.05	0	-1.12	0	-1.83	0	-2.45	0	-0.81	0
Cd	-5.2	0	-5.1	0	-5.2	0	-1.0	0	-5.8	0	0.43	1
Hg	-1.58	0	-1.68	0	-0.39	0	-0.58	0	-1.87	0	1.76	2
As	3.43	4	3.38	4	3.30	4	3.27	4	3.08	4	2.92	3

2.3 Survey results and evaluations of heavy metals in the organisms

Heavy metals of fish, crustaceans and shellfish biological samples in the study area have been detected. By single factor method, the first-class standard stipulated in Marine Life Quality GB18421-2001 is used to evaluate pollutant contents in shellfish (bivalves). Meanwhile, this paper used limit standard in the safety qualification for agricultural product-safety requirements for non-environmental pollution aquatic products (GB18406.4 -2001) to evaluate pollutant contents (Hg, As, Pb and Cd) in other mollusks, crustaceans and fish organism, which is lack of national standards. The results are showed in table 7 and 8. Heavy metals contamination of shellfish is the highest relatively, because bivalves can produce metallothionein firmly combined with a large number of heavy metals [12]. Contents of Cu, Zn are higher than contents of Hg, Pb, As and Cd in organism, which may due to background contents of essential elements Cu, Zn higher than non-essential elements Hg, Pb, As and Cd [18]. Another reason may be that shellfish often can selectively absorb essential elements strongly, but not obviously be non-essential elements [19], which is attribute to unconspicuous heavy metals pollution in Dongzhai Harbor. Organisms are all

accord with the requirement in safety qualification for agricultural product-safety requirements for non-environmental pollution aquatic products [20].

Tab. 7 Evaluation standard of heavy metals in marine organisms

Fresh samples of marine organisms	w/*10^{-6}					
	Cu	Pb	Zn	Hg	Cd	As
First-class standard stipulated of shellfish [21]	10	0.120	1.0	0.2	0.2	0.05
Limit standard in aquatic safety requirements for the safety and quality of agricultural products [20]	≤50	≤0.5	≤20	≤0.3	≤0.1	≤1.0

Tab. 8 Evaluation results of heavy metals in marine organisms

Heavy metals	evaluation results in marine organisms					
	Cu	Zn	Pb	Cd	Hg	As
fish	0.04 (0.01 - 0.08)	0.16 (0.13 - 0.19)	0.02 (0.01 - 0.04)	0.03 (0.01 - 0.06)	0.02 (0.01 - 0.03)	0.02 (0.01 - 0.04)
Crustaceans	0.04 (0.01 - 0.10)	0.07 (0.03 - 0.15)	0.05 (0.02 - 0.09)	0.05 (0.02 - 0.10)	0.02 (0.01 - 0.04)	0.03 (0.01 - 0.06)
Shellfish	0.25 (0.16 - 0.39)	0.33 (0.25 - 0.44)	0.41 (0.23 - 0.54)	0.22 (0.13 - 0.35)	0.03 (0.02 - 0.05)	0.23 (0.15 - 0.37)

3 Conclusions

(1) The heavy metal pollution levels in the seawater of the Dongzhai Harbor accord with the first category of the seawater except Pb, which reach the second category of the seawater, and are much lower than the fishery water quality standard, which indicates it is suitable for fishing.

(2) Contents of heavy metals (Cu, Zn, Pb, Cd, Hg, As) in superficial sediments of Dongzhai Harbor accord with the first class sediment quality, indicating sediments in Dongzhai Harbor have not been polluted by heavy metal obviously; but sediments in hidden shoal of Dongzhai Harbor have a bit higher heavy metal contents than typical mangrove wetland in Hainan Island and the surrounding area.

(3) On the basis of evaluation results by index of geo-accumulation(I_{geo}), we suggest that, except as pollution level of heavy metals in superficial sediments of Dongzhai Harbor belongs to non-pollution. However, index of geo-accumulation of heavy metal in mangrove

wetland and hidden shoal is higher than that in bottom sediments of Dongzhai Harbor, indicating mangrove region on tidal flat in the estuary may become a heavy metal enrichment region and have been affected by land-based pollution influence.

(4) According to the quality standards of marine organisms, biological samples of fish, crustaceans and shellfish all meet the first-class standards and requirements of aquatic products.

References

[1] Dai Ji-cui, Ni Jin-ren. Advances of studies on biogeochemistry of environmental pollution in mangrove wetlands [J]. Marine Environmental Science, 2009, 28(6): 779 - 784.

[2] Wu Xiang-qing, Li Xiao-zheng, Lan Liu-cun. Assessment on the heavy metals pollution in surface sediments of pearl culturezone of Pearl Bay in Fangcheng City [J]. Marine Science Bulletin, 2010, 29(5): 584 - 587.

[3] Ma Li, Cai Li-zhe, Yuan Dong-xing. Advances of studies on mangrove benthic fauna pollution ecology [J]. Journal of Oceanography in Taiwan Strait, 2003, 22(1): 113 - 119.

[4] Terchunian A, Klemas V, Alvarez A, et al. Mangrove mapping in Ecuador: The impact of shrimp pond construction [J]. Environmental Management,1986,10: 345 - 350.

[5] Yao Pan-zhao, Zhang Yu-feng, Hu Xin, et al. Occurrence states and potential mobility of heavy metals in sediments of Western Xiamen Bay [J]. Journal of Oceanography In Taiwan Strait, 2010, 29(4): 532 - 538.

[6] Tang Yi-jie, Fang Zhan-qiang, Yu Shi-xiao. Heavy metals, polycyclic aromatic hydrocarbons and 0rganchlorine pesticides in the surface sediments of mangrove swamps from coastal sites along the Leizhou Peninsula,South China [J]. Acta.Oceanologica Sinica, 2008, 27(1): 42 - 53.

[7] Luoping Zhang, Xin Ye, Huan Feng, et al. Heavy metal contamination in western Xiamen Bay sediments and its vicinity ,China [J]. Marine Pollution Bulletin, 54(2007): 974 - 982.

[8] Tan Lin-zhi, Qi Shi-hua, Fu Yang-rong, et al. Heavy metal pollution survey and evaluation of surface soil in higher-place ponds culture zone in Bamen Bay of Hainan [J]. Environmental Chemistry, 2010, 29(2): 335 - 336.

[9] Qiu Yao-wen, Yu Ke-fu. Accumulation of heavy metals in sediment of mangrove wetland from Hainan Island [J]. Journal of Tropical Oceanography, 2011, 30(2): 102 - 108.

[10] GB 17378-1998, The specification for marine monitoring [S].

[11] Patharbison. Mangrove mud-a sink and a source for trace metal. Marine Pollution Bulletin, 1986, 17(6): 246 - 350.

[12] Qu Hong-xia, Dong Shu-gang, Tang Zhi-hong, et al. Distribution and ecological evaluation of heavy metals in multi-medium of Luoyuan Bay [J]. Marine Environmental Science, 2009, 28(3): 293 - 308.

[13] GB 3097-1997, Sea water quality standard [S].

[14] GB 18668-2002, Marine sediment quality [S].

[15] Vane C H, Harrison I, Kim A W, et al. Organic and metal contamination in surface mangrove sediments of South China [J]. Marine Pollution Bulletin, 2009, 58: 134 - 144.

[16] Muller G. Index of geoaccumulation in sediments of the Rhine River [J]. Geojoumal, 1969, 2: 108 - 118.

[17] Ecological-geochemistry survey of Hainan in the national second general survey of soil- 1:250000 multi-objective regional geochemical survey report in Hainan island

[18] Jia Zhen-bang, Zhou Hua, Zhao Zhi-jie, et al. The Application of the Index of Geoaccumulation to Evaluate Heavy Metal Pollution in Sediments in the Benxi Section of the Taizi River [J]. Acta Scicentiarum Naturalum Universitis Pekinesis, 2000, 36(4): 525 - 530.

[19] Xue Ke, Han Jia-bo, Zhuang Ren-qin. Analysis of heavy metal content in shelfish along the Liaoning coast [J]. Fisheries Science, 1994, 13(2): 16 - 19.

[20] Usero J, Gonzalez-Regalado E, Gracia I. Trace metal in the bivalve molluscs Ruditapes decussatus and Ruditapes philinarum from the Atlantic coast of southern spain [J]. Environ. Intern., 1997, 23(3): 291 - 298.

[21] GB 18406.4-2001. Safety qualification for agricultural product-Safety requirements for non-environmental pollution aquatic products [S].

[22] GB 18421-2001. Marine biological quality [S].

海南东寨港重金属在多种环境介质中污染状况及评价

田海涛[1]，曹玲珑[1,2*]，王 平[1]，谢 健[1]，何远胜[3]

（1. 国家海洋局南海海洋工程勘察与环境研究院 广东 广州 510300；2. 中山大学地球科学系，广东 广州 510275；3. 国家海洋局海口海洋环境监测中心站，海南 海口 570311）

摘 要：分析了东寨港海水、表层沉积物和生物体中重金属 Cu、Zn、Pb、Cd、Hg、类金属 As 的含量及分布特征，并运用单因子指数法、地积累指数法评价了该调查区重金属污染程度。结果表明：东寨港海水中除 Pb 的含量符合二类海水标准外，其余含量均符合一类海水标准，且远低于渔业水质标准限值；表层沉积物中典型重金属元素含量都符合海洋沉积物质量一类标准，基本属于无污染区；本区湿地沉积物中的重金属含量比岛内及周边区典型红树林湿地略偏高；红树林及暗滩沉积物中重金属比东寨港水底沉积物重金属含量高，表明河口湾潮滩上的红树林区可能是重金属元素的富集区，东寨港目前可能受到了陆源污染的影响；生物体中重金属含量均符合一类标准，符合无公害水产品的要求。

关键词：海水；沉积物；海洋生物；重金属；东寨港

RECEIVED
8/1/17

Marine Science Bulletin

Marine Science Bulletin publishes papers on marine science and technology including physical oceanography, chemical oceanography, marine biology, marine geology, environmental oceanography, estuarine & coastal sciences, marine technology, digital ocean, coastal zone management, ocean engineering, marine economics, etc., and aims to promote international academic exchange.

Editor-in-Chief: XU Sheng (徐　胜)
Associate Editor-in-Chief: LI Dong-xu (李东旭)　XUE Hui-feng (薛惠芬)
Executive Editor: QIU Wen-jing (邱文静)　LI Xue (李　雪)　YANG Rui (杨　瑞)
LI Xiao-guang (李晓光)　DONG Yi (董　艺)　YUAN Ze-yi (袁泽轶)
English proofed by: WANG Qi (王　琦)

Semi-annually (started in 1999, sum 30)
Publication date: May 15th and Oct. 15th

Marine Science Bulletin **(Vol. 15, No. 2, Oct. 2013)**

Responsible Institution:
State Oceanic Administration of China
Sponsored by:
National Marine Data and Information Service
Edited by:
Office of Marine Science Bulletin (English edition)
Printed by:
Printery of National Marine Date and Information Service

Published by:
Office of Marine Science Bulletin (English edition)
E-mail: msb@mail.nmdis.gov.cn
Tel: (022) 24011287
Address: 93 Liuwei Rd., Hedong District, Tianjin 300171, China

---

ISSN1000-9620
CN12-1271/N

Price: $ 30.00 / ￥40.00 Per year

ISSN 1000-9620

02>